Author:
Stefan, Lucio

Title:
Scanning magnetometry with single-spin sensors

Scanning magnetometry with single-spin sensors

Lucio Stefan

Department of Physics
University of Bristol

A dissertation submitted to the University of Bristol in accordance with the requirements of the degree of Doctor of Philosophy in the Faculty of Physics.

January 2020

Word count: Thirty-thousand four-hundred forty-two

Summary

Magnetic imaging is an increasingly important tool for fundamental research and technology. The nitrogen-vacancy centre (NV) defect in diamond has emerged as a promising single-spin sensor which can detect not only magnetic fields but also electric fields and temperature. 2D mapping of magnetic fields can be achieved by grafting a diamond containing NVs to the tip of a scanning probe. Its single spin nature can be used to image large spin textures without perturbing them, as well as enabling the sensing of the stray fields produced by single electron spins and nuclear species.

Despite the realisation of NV magnetic sensing in the last few years, the technique has been developed only by few research groups. The technical challenges increase when the system is operated at cryogenic temperatures, which are needed when magnetic samples with low Curie temperature or superconductors are to be imaged. This thesis describes the work done towards the implementation of two scanning NV magnetometry experiments, the first of their kind at the University of Cambridge.

The first type of NV sensing we explore is based on NVs in nanodiamonds, deposited on the surface of a material which is ferromagnetic below 130 K. The NVs act as point-probes of the stray field, providing information on the spatial variation of the material. However, NV centres operated as point probes of stray fields are not suitable to image spin textures in magnetic materials. Starting from two types of scanning probe microscopes, one operating at room temperature and one operating from room temperature to 3 K, two scanning NV magnetometers are developed.

The imaging of the stray fields arising from magnetic field sources at the nanoscale with these two systems successfully establishes the technique in the Cavendish laboratory, offering a promising platform for the study of spin textures.

Acknowledgements

These last four years have been a deeply transformative experience, both personally and scientifically. Here I wish to thank the people who have been part of this adventure and who stayed next to me through the ups and downs of the PhD. The intention was to keep the "Acknowledgements" section down to one page but well, sometimes things do not always go as planned.

First of all, thanks to Prof. John Rarity. Without him, I would be somewhere else in the world. His suggestion to apply to the Quantum Engineering CDT program in Bristol has allowed me to learn much more than I could expect. I wish to thank him for having supported me in times of need, squeezing some time for me in his busy schedule. His proofreading considerably improved the quality of this document.

Another thank you goes to Prof. Mete Atatüre, for letting me join his group and supervising me throughout my work. Without him, the two scanning setups would not exist. He has created a research group where brilliant people with whom having stimulating discussions do not lack.

My first year of CDT back in Bristol has been special. Peter Turner and Chris Erven have done an amazing job at coordinating and teaching us. Thank you to Alex Moylett, Geraint Gough, Martin Nicolle, Henry Semenenko, Lawrence Rosenfeld, Jason Mueller, Joe Smith and Sam Holder for the year spent together in the CDT office. I still miss the discussions we had, ranging from quantum theory to philosophy of science, NV centres, atomic clocks and python coding. Lin, Andrea, Becky and Sorrel have been extremely efficient with administering the CDT and have always been happy to help with any issue I had. Finally, special thanks go to Pete for the chats we had.

The group in Cambridge has been an equal source of interesting people. Dhiren Kara welcomed me in the group and was the one who helped me out during my summer project at the Cavendish lab before the start of my PhD. Although he has been busy with entirely different experiments since then, he has always been there for a chat. I have learnt a great deal from him, from the most technical aspects of research to the theory of spin control. He has the rare skill to deconstruct difficult

problems into intuitive solutions. My biggest regret is that I did not have the chance to work with him a bit more, so that I could snatch more secrets from him!

Helena Knowles was here at the beginning of my PhD. She has always been available for interesting chats about spins, either single or many; her insights after talks and seminars added extra depth and implications I could not see. Without her support, these words would probably have not been written.

Anthony Tan has been both an amazing co-worker and friend. Work has been a much less lonely task since he joined the group in the last half of my PhD. The attocube NV-AFM was set up together with him. His expertise in magnetism, together with his passion for research, have been crucial for the progress of the experiment. Without his programming skills, our code would not run as smoothly as it does (except when you need to generate large matrices!). He managed to quickly learn from scratch how to use mumax^3 to run the micromagnetics simulations used in Chapter 5. I believe it would have taken me much longer to figure out how to do it. I also thank him for proofreading this thesis. He has a peculiar taste for rewriting in MATLAB® already existing Python scripts made in-house, he loves greyscale colormaps and complaining about the cold. Legends say he makes a pretty good pesto.

In these last three months the scanning NV team has doubled its size with Michael Högen and Baptiste Vindolet joining the ranks of the scanning NVs. They have proven to meet the attitudinal standards to be full-fledged scanning NV team members. Their work has considerably increased the rate at which experiments can be done. In particular, Michael modified the room temperature setup with Anthony to acquire images of MFM tips, which are presented at the end of Chapter 4.

David Dominik Jarausch and Lina Klintberg need to be credited for acquiring some of the data presented in Chapter 3. Nicolas Gauriot helped me setting back up the Montana experiment when he joined the group for his masters project. He worked with me on the PCMO experiment in the first few months of PhD, when we were both young and naive.

Alejandro Rodriguez-Pardo Montblanch has shared the lab space with me once I started working on the scanning setups, although he works with "flat" materials. Together, we turned an empty room into a new lab full of fancy equipment. He taught me to ponder my career choices a bit more –probably more than he would expect– and he somehow managed to keep me on track in the most difficult moments of my PhD. His inappropriate jokes entertain the whole group, even though sometimes he pretends to be a serious person.

Noah Shofer, who joined the group to work with NV biosensing for his MPhil, has

been an office mate for a while and is always a source of interesting conversations. One day I will manage to convince him that the Alps are good hiking spot. His love for climbing trees and dangerous cycling is unparalleled. He also found the time to proofread parts of my thesis, for which I am grateful.

Paolo Andrich deserves to be mentioned in this thesis for the numerous chats we had, about science and life. His humbleness and being down to earth conceal a lot of knowledge and interests. I hope we will manage to keep in touch, even when we *an varè per frosole*.

Claire Le Gall and Dorian Gangloff are both impressive scientists. I wish I had more time –and courage!– to ask them questions about the details of their research on quantum dots. Carola Purser, who has recently joined the group to work on 2D materials and SxVs, gave us pretty good suggestions that fixed some of the issues we had. We had interesting scientific discussions with Hannah Stern and I hope we are going to be able to work together in the future. I wish to thank Qiushi Gu, Johnny Bodey, Daniel Jackson and Carmen Palacios-Berraquero for the nice chats we had during these years. I am also looking forward to knowing better the new members of the group, which has recently welcomed many more members than it used to be!

A big shout-out to the group members who were part of the group and left throughout these three years. Matteo Barbone is one of the best researchers I have met. Although he claims to have a limited knowledge of theory, he easily compensates with an almost boundless creativity and ingenuity. The group thoroughly misses a polarising figure like him. I hope he and Maddalena will manage to keep bees some day! Ben Pingault has always been happy to support me and give me suggestions, probably as many as the pictures of the group he took and never showed. Mustafa Gündoğan is a well-rounded person and scientist. I miss the interesting chats about science and philosophy that we had every now and then, and the strolls through Grantchester meadows. I feel grateful to have had the chance to cross paths with Robert Stockhill and Gabriel Éthier-Majcher: they are both kind people and great scientists.

I also thank Jean-François Roch for the interesting scientific discussions we had when he visited the group during his sabbatical, and for being kind enough to host me in his group for a month. In this occasion I was lucky to work with Loïc Rondin and Thimotée De Guillebon, who taught me so much in so little time.

Finally, I wish to thank all the friends scattered around the world, and my family. Without their love and support, I would not be where I am now. Special thanks to Valentina: you have put up with me –and you keep doing it!– throughout these years. Your contribution to this thesis is probably the most important one. Thank

you for being at least as stubborn as I am. I hope we are going to share even more adventures in the times to come.

Author's declaration

I declare that the work in this dissertation was carried out in accordance with the requirements of the University's Regulations and Code of Practice for Research Degree Programmes and that it has not been submitted for any other academic award. Except where indicated by specific reference in the text, the work is the candidate's own work. Work done in collaboration with, or with the assistance of, others, is indicated as such. Any views expressed in the dissertation are those of the author.

SIGNED:..... DATE:.....

Contents

List of Figures

List of Tables

"O frati," dissi, "che per cento milia
perigli siete giunti a l'occidente,
a questa tanto picciola vigilia

d'i nostri sensi ch'è del rimanente
non vogliate negar l'esperïenza,
di retro al sol, del mondo sanza gente.

Considerate la vostra semenza:
fatti non foste a viver come bruti,
ma per seguir virtute e canoscenza."

Dante Alighieri, *Inferno* XXVI, 112–120

Chapter 1

Introduction

Magnetism plays an important role both in current technology, where its most common application is found in memory storage devices, and in fundamental physics research, because of the many-body interactions arising from spin ensembles. Detecting weak magnetic fields at the nanoscale is thus a key challenge in the field.

As an example of the lengthscales involved in magnetism, the increasing demand for memory storage has pushed the hard drive technology to manipulate and read smaller and smaller magnetic bits. The smallest achievable bit size in current state-of-the-art technology is $20\,\mathrm{nm}^2$ [1]. The manipulation of magnetic domain properties lies at the heart of the relatively new field of spintronics. The controlled motion of domain walls by the aid of spin-polarised currents [2, 3] has prompted proposals and experimental studies for the implementation of racetrack memories [4], which have the potential to offer high storage densities and low power consumption. However, the domain wall motion in thin films is highly dependent on the number of defects, which lead to pinning and consequently to a reduced overall domain wall velocity. Over the last ten years, the research in quasi-particles known as skyrmions [5] –topologically-protected winding spin textures– has considerably grown after the first observations in bulk materials and in thin films [6, 7]. The robustness to external perturbations, given by their non-trivial topological charge, makes them a promising candidate for a new generation of spintronic devices which are not strongly affected by the film defects [8, 9]. Beyond memory applications, skyrmions have been proposed for alternative implementations of computers architectures [10], for neuromorphic computing [11] and for the implementation of magnonic crystals [12]. In all these applications, a high-sensitivity, high-resolution and ideally non-perturbative probe of the spin textures is an essential tool for the full understanding of their physics.

Magnetic field sensing can be extended to the detection of time-dependent mag-

netic fields. One of the most important applications in this sense is nuclear magnetic resonance (NMR) spectroscopy: by detecting the Larmor precession of atomic species invaluable information on the structure and local environment of molecules can be discerned. The holy grail for nanoscale NMR spectroscopy is the 3D imaging of molecular structures, which could find important applications in fundamental chemistry and also in medicine, where the determination of the structure of in-vivo proteins remains an outstanding challenge.

The need to probe spins for technological applications in computing and medicine, understanding complex many-body phenomena in novel materials, and probing fundamental aspects of chemistry has led to the development of a number of techniques for nanoscale magnetic imaging. Here we describe scanning probe techniques, since these are the ones most closely related to the subject treated in this thesis.

One of the most widely used scanning magnetometry techniques is magnetic force microscopy (MFM), which is an evolution of atomic force microscopy. A sharp silicon tip (tip radii are typically of the order of few tens of nm), coated with a magnetic material, is brought in close contact with the sample surface. Magnetic imaging is achieved by tracking the deflection induced by the magnetic dipole interaction between sample and the tip, while the latter is scanned over the surface [13]. This technique can achieve high spatial resolution and is generally offered as an option in commercially available atomic force microscopes. The technique is compatible at room to cryogenic temperatures. As a downside, the very same interaction that allows the imaging can also hinder the image quality. The stray fields generated by the tip can perturb the magnetic textures of a magnetically soft sample. MFM also lacks the sensitivity to detect very weak magnetic fields, such as the ones produced by isolated spins.

An alternative route for high-resolution imaging is a scanning superconducting quantum interference device (SQUID), which consists of a superconducting loop containing Josephson junctions. When SQUIDs are operated as a magnetometer the flux quantum Φ_0 ($\Phi_0 = h/(2e)$)through the loop is measured. The technique can offer extremely high sensitivities, of the order of $1\,\mathrm{fT}/\sqrt{\mathrm{Hz}}$ [14]. In recent years, SQUIDs have been fabricated on tips for scanning probe microscopy, enabling scanning magnetic imaging at the micro- and nano-scale [15–18]. Scanning nano-SQUIDs with a diameter as low as 56 nm have been demonstrated, boasting a spatial resolution of 20 nm and a magnetic field sensitivity of $0.6\,\mu_\mathrm{B}/\sqrt{\mathrm{Hz}}$ ($140\,\mathrm{nT}/\sqrt{\mathrm{Hz}}$), sufficient to detect a single electron spin [19]. The fabrication of scanning nano-SQUIDs however is technologically challenging. There is also a trade-off between the minimal loop size, which determines the maximum spatial resolution, and the minimum achievable sen-

sitivity. The technique is currently limited to operation at cryogenic temperatures, required to maintain the superconductivity of the magnetometer.

Combining the features of scanning probe microscopy and magnetic resonance imaging, magnetic resonance force microscopy is another competitive alternative for magnetic imaging. The detection scheme is based on the resonance shift of a magnetised oscillating cantilever induced by the interaction between the cantilever and spins in a sample [20]. In order to increase the signal-to-noise ratio sufficiently, temperatures below 4 K are required. Using the same technique, 3D magnetic resonance imaging of a biological sample, with a spatial resolution < 10 nm has also been achieved [21].

Above I have briefly described three techniques that are either routinely used in magnetic imaging experiments (as MFM) or offer a promising route for high-resolution and high-sensitivity imaging. However, the magnetism community can make use of many more techniques to obtain a complete picture of the sample magnetic properties, such as total magnetic moment, stray fields or magnetisation. Among the tabletop techniques, we mention micro-Hall probes, which can have a sensitivity of $1\,\mathrm{nT}/\sqrt{\mathrm{Hz}}$, although at the cost of a spatial resolution of $\approx 1\,\mu$m [22]. Spin-polarised scanning tunneling microscopy (SP-STM) –a version of scanning tunneling microscopy which measures the tunneling of a spin-polarised current through a film– can image magnetic ordering with atomic resolution [23]. Microscopes based on the magneto-optical Kerr effect (MOKE) provide magnetic imaging and at the same time can probe other properties of a magnetic thin film (such as the $M - H$ hysteresis loop) all-optically, but have limited spatial resolution and sensitivity [24]. Lorentz-force microscopy detects the deflection of a beam of electrons which are transmitted through a magnetic sample, using a transmission electron microscopy setup. It can achieve resolution < 5 nm and it is sensitive to both the stray fields and the magnetisation of the sample itself [25].

Within larger facilities, synchrotron light can be used to image magnetic ordering with X-Ray magnetic circular dichroism (XMCD), which can be combined with the emission of secondary photoemission electrons (XMCD-PEEM) to image the magnetisation of a sample with resolution of few tens of nm [26]. The technique requires free-standing samples which are thinned to transmit enough X-rays to build up a signal.

In the early 2000s, an optically active spin defect occurring in diamond, called nitrogen-vacancy (NV) centre, was proposed for a new type of scanning probe magnetometers. These magnetometers detect the Zeeman shift induced by an external stray field on the spin of the sensor [27, 28]. Initially studied in ensembles, single

defects were successfully isolated by Gruber *et al.* [29]. The spin state of the NV can be detected optically via spin resonance experiments and, in contrast to other quantum platforms, it can be easily polarised into its quantum ground state using optical excitation with high fidelity, even at room temperature. Early experiments proved that the spin of the NV centre can be coherently controlled [30] and it can interact coherently with its surrounding spin environment, such as the neighbouring nitrogen atom making up the defect or ^{13}C and other spins impurities in the vicinity of the NV [31–33].

The progress in the control of the NV properties has prompted new research to investigate its applicability as a quantum sensor. Given its single-spin nature, the weak magnetic fields generated by the NV itself do not perturb the probed sample. The advancements in diamond fabrication now allow for quasi-deterministic creation of NV centres [34–36] enabling NV-to-sample distances which are less than 10 nm [37, 38]. The careful engineering of the local magnetic environment surrounding the defect [39] permits high sensitivities, which can reach $0.9\,\mathrm{pT}/\sqrt{\mathrm{Hz}}$ [40]. These two quantities, combined together, are an important figure of merit for any magnetometer. Since the magnetic field produced by magnetic dipoles scales with $\sim 1/r^3$, high-sensitivity at small sample-to-probe distances allows to detect and image weak magnetic field sources, as shown in Figure 1.1.

NV centres in bulk diamond have been used in a number of studies, for example the imaging of the current flow in graphene [41], to measure the propagation of neuron pulses *in-vivo* [42] and to probe living bacteria containing magnetite particles [43]. Taking advantage of the spectral selectivity of the NV spin using coherent control sequences, nanoscale MRI of molecular electrons [44, 45] and nuclear spins [46, 47] in liquids has also been demonstrated.

In 2008 a paper by Balasubramanian et al. [48] took advantage of the high sensitivity of the NV centre to implement a scanning probe magnetic field sensor. A nanodiamond containing an NV centre was grafted to the tip of an atomic force microscope (AFM) probe. The AFM system maintains a close proximity between sample and probe, and the application of laser and microwave excitation allows the spin resonance –i.e. the Zeeman splitting– of the NV centre to be measured while the tip is scanned across the surface. Following this work, many research groups have pursued scanning NV magnetometry, both using nanodiamonds grafted to an AFM tip [49] and developing a new type of scanning probe: diamond nanopillars containing single shallow-implanted NVs [50].

One of the advantages of scanning NV magnetometry is the flexibility of environmental conditions it can withstand. Scanning NV probes can operate from room

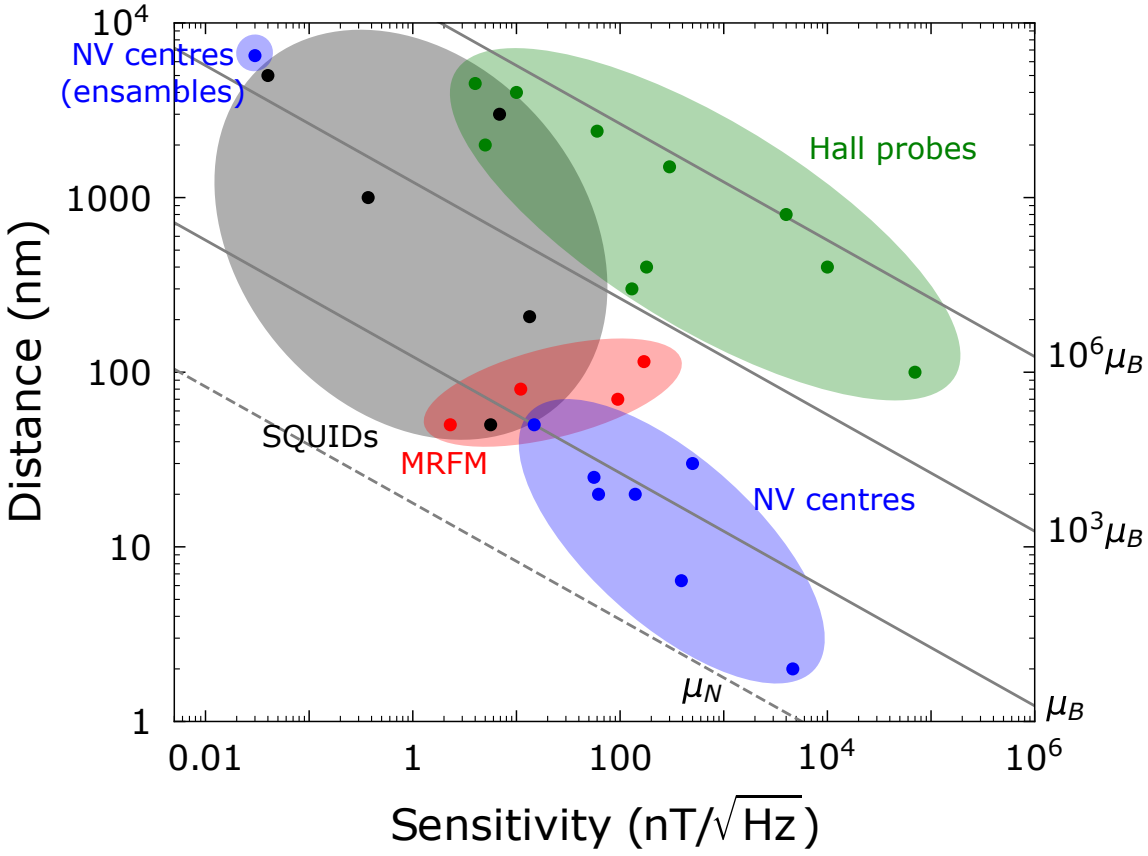

Figure 1.1: Performance of experimentally demonstrated magnetic field sensors, plotted versus sample-to-probe distance and sensitivity. The chart is adapted from Reference [54]. The datapoints represent μ-Hall sensors [22], scanning SQUID sensors [15–19], magnetic resonance force microscopy [20, 55, 56] and NV sensors [47, 50, 53, 57–61]. The dashed line marks the distance-sensitivity threshold to detect one nuclear spin, the solid lines mark the thresholds to detect one electron ($\sim \mu_B$), $10^3\mu_B$ and $10^6\mu_B$. The magnetometers combine high sensitivity a small sample-to-probe distance, which enables high-resolution imaging.

temperature to $< 4\,\mathrm{K}$ [51]. The atmospheric environment does not influence the sensor performance. Since the NV is on the tip of a scanning probe, the NV can achieve close proximity with the sample, with a record minimum of 10 nm demonstrated. Owing to its intrinsic quantisation axis, the Zeeman splitting of the NV centre is determined by the projection of the magnetic field vector along the axis, allowing for vectorial imaging of the stray field [52], which is a unique feature for scanning probe magnetic field sensing. The sensitivity of the NV centre, which is $\approx 1\,\mu\mathrm{T}/\sqrt{\mathrm{Hz}}$ for continuous-wave excitation, can be lowered using coherent spin driving to achieve single-electron spin sensitivity with a scanning system, as demonstrated by Grinolds et al. [53].

Thanks to its unparalleled flexibility, scanning NV magnetometry has been used to study magnetic textures [62, 63], the correlation of dipolar ordering and spin ordering in multiferroics [64], magnetic vortices in superconductors [65], and ferritins

in living cells [66], among other things. Scanning NV magnetometry is not only limited to the sensing of static stray fields. Since the NV resonance is affected by other parameters such as temperature, ensambles of NV centres in nanodiamonds have been used to perform nanoscale thermometry [67]. Taking advantage of the NV centre sensitivity to time-dependent fields, microwave fields generated by a wire [68] or the conductivity of a normal metal [69] can also be imaged.

Despite the progress and the results achieved with this technique, only a few research group have an operational scanning NV setup. The relatively broad expertise require to implement it and operate it limit its attractiveness, when compared to established techniques such as MFM.

Summary

This thesis describes the work and the experimental challenges of NV magnetometry and the development of two scanning NV setups, the first of their kind at the Cavendish laboratory in Cambridge.

In **Chapter 2** I explain the physical properties of the NV centre. Initially, I focus on the ground state Hamiltonian of the NV centre. Understanding the behaviour of the NV centre under magnetic fields with arbitrary intensity and direction is essential to interpret correctly the spin resonance response. After reviewing the standard protocols for magnetic sensing with NV centres, I develop a model of the NV magnetic field-dependent photodynamics, which greatly influence the applicability of scanning NV magnetometry. I also summarise the principles of atomic force microscopy and I describe the different setup geometries used in this work.

Chapter 3 presents the analysis of an inorganic perovskite which exhibits ordering at cryogenic temperatures. I measure the temperature dependent stray fields which are detected by NV centres in nanodiamonds scattered on the surface of the thin film. Using a few NV centres as magnetic point probes I attempt to draw conclusions on the magnetic domain size. Using Rabi nutations as a probe of magnetic field noise, I investigate the spatial variations at which the magnetic ordering arises across the thin film.

In **Chapter 4** I describe the development of the first type of scanning NV magnetometer developed in our laboratories, which operates at room temperature. After having examined the technical details of the setup implementation, I show the proof-of-concept of magnetic imaging with NVs in nanodiamonds grafted on an AFM tip. I also present the preliminary results obtained in the imaging of the stray field of an AFM tip using an "inverted" scanning magnetometer configuration.

I describe the implementation of another scanning NV magnetometer which can operate from room temperature to 3 K in **Chapter 5**. This setup makes use of commercial diamond tips, which have the advantage of removing the time-consuming process of nanodiamond grafting. After having presented some preliminary magnetic imaging on hard disk drives, I present the characterisation of the NV-to-sample distance. In most of the analysed tips, the NV centres are found to have values of NV-to-sample distance too large to image samples which have magnetic domains with a size of few tens of nanometres. Using tips which have adequate NV-to-sample distance I present some all-optical studies of the domain patterns in magnetic thin films.

In **Chapter 6** I outline the progress made towards the implementation of the two scanning NV setups. I highlight the technological hurdles that need to be overcome to increase the setup performance and I consider possible research areas which can be explored with scanning NV magnetometry.

Chapter 2

The nitrogen-vacancy centre

Diamond is one of the allotropes of carbon, consisting of a perfect lattice of carbon atoms arranged in a tetragonal structure. However, defects are often present in real crystals. Their presence modifies the band structure and leads to effects that would be unobservable in a perfect crystal. For example, diamond can become an electric conductor if doped with phosphorus [70], and it becomes a type II superconductor with a 4 K critical temperature if doped with boron [71]. This work discusses point defects in diamond, which are present in the form of vacancies (missing carbons), elemental impurities or combinations of the two. Over 100 of these defects are fluorescent [72] and have been extensively studied over the past 60 years.

The nitrogen-vacancy (NV) centre in diamond is made of a substitutional nitrogen atom and a neighbouring vacancy (Fig. 2.1). The defect can have four possible orientations, corresponding to the four ⟨111⟩ equivalent orientations of diamond.

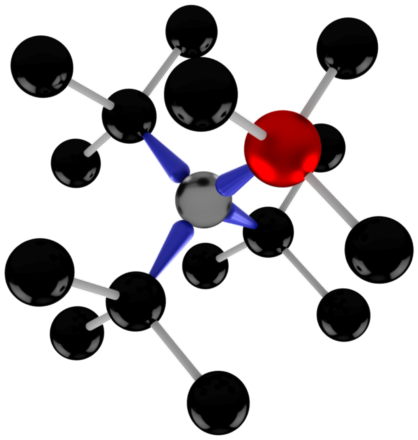

Figure 2.1: Schematic representation of the nitrogen-vacancy (NV) defect. The black spheres represent carbon atoms. A substitutional nitrogen atom (red sphere) and a neighbouring vacancy (grey sphere) form the NV defect. The dangling bonds of three carbon atoms (blue bonds) are caused by the missing carbon atom.

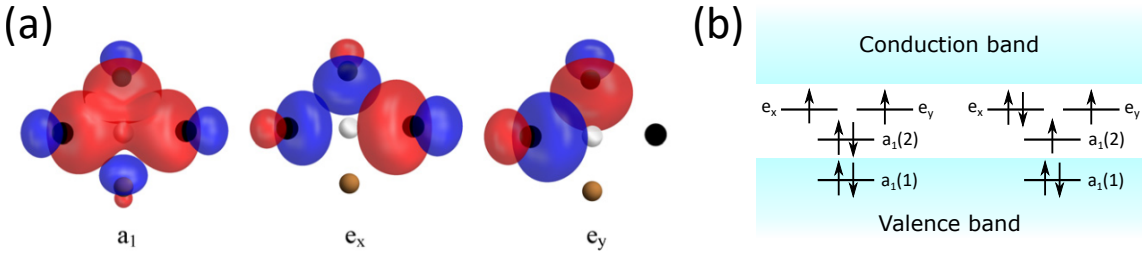

Figure 2.2: Molecular orbitals and band structure. (a) Molecular orbitals used to calculate *ab initio* the symmetry and the energy of the true NV eigenstates. Adapted from [84]. (b) Position of the molecular orbitals within the diamond energy bands. Adapted from [85].

The breaking of the crystal symmetry creates localised electronic states, mostly localised at the vacancy site. *Ab initio* calculations have shown that the wavefunction volume is about 1 nm^3 [73]. The NV centre can be found in a neutral (NV^0) or negatively-charged (NV$^-$) state. When the defect is in NV^0 [74], the four electrons contributed by the carbon dangling bond and the additional electron donated by the nitrogen atom form a spin $S = 1/2$ system. Molecular model studies [75] have determined that the NV$^-$ is explained by a six-electron model with $S = 1$, meaning that an additional charge is trapped at the NV site from a neighbouring charge donor in the crystal, which has been attributed to a nitrogen impurity [76]. The optical spin polarisation and the energy level structure make the NV$^-$ a desirable state for magnetometry, while the NV^0 is primarily used in some schemes to perform single-shot readout of the NV$^-$ spin state [77] or to perform photoelectric readout [78] of NV$^-$.

Control of the charge state can be achieved by modifying fabrication parameters such as surface impurities [79, 80] and position of the Fermi level [81]. Optical excitation can also modify the charge state of NV. It has been verified that even under continuous optical illumination with an excitation wavelength of 532 nm the NV cycles between NV^0 and NV$^-$. The NV$^-$ steady-state population can make up $\geq 75\%$ of the emitted photons. Several studies have verified that the charge conversion from NV$^-$ to NV^0 is a two-photon process which depends on the excitation wavelength and optical power [82, 83]. Even though it is possible to create optical detection schemes to readout and initialise the charge state of the NV, measurements of the emission spectra empirically showed that in our case the prevalent charge state is NV$^-$. When "blinking" of the NV PL occurs another emitter which shows stable emission over time is selected. For this reason, NV will refer to the NV$^-$ charge state for the rest of this thesis.

2.1 Orbital structure and optical properties

The NV defect has a C_{3v} symmetry, with a symmetry axis along the line connecting the vacancy to the nitrogen. *Ab initio* calculations using molecular orbitals (Fig. 2.2(a)) predict that the molecular orbitals corresponding to the three carbon atoms and to the nitrogen atom combine to create a completely filled level in the valence band and three more partially filled levels within the bandgap [85]. By including Coulomb repulsion to the model, the molecular orbitals split to form four states with energy levels lying within the bandgap. Both experiments [86–89] and theory [84] determined that the electronic ground state is a spin triplet $^3A_2$. The optical zero phonon line (ZPL), at a wavelength $\lambda_{ZPL} = 637\,\text{nm}$, is associated to a transition between the ^3E excited state and the $^3A_2$ ground state (Fig. 2.3). Two additional singlet states, $^1A_1$ and ^1E, are coupled by an optical transition with a zero phonon line centred at $\lambda_{ZPL} = 1046\,\text{nm}$. The position of these two levels with respect to the other two states is currently unknown.

The $^3A_2$ and the ^3E are further split by spin-spin interactions which partially lift the spin degeneracy. The $^3A_2$ splits into a $m_s = 0$ ground state which is split by 2.87 GHz from the $m_s = \pm 1$ levels. The presence of strain, electric fields or magnetic fields further split the $m_s = \pm 1$ levels. In the absence of lattice vibrations, i.e. at cryogenic temperatures, two spin triplets are resolvable in ^3E level [90]. At room temperature, however, the levels are averaged out into three, where the lowest-energy state corresponds to $m_s = 0$, whereas the $m_s = \pm 1$ have higher energy and are split from $m_s = 0$ by 1.42 GHz.

The NV centre can be addressed with off-resonant excitation energetically above the ZPL, i.e. with a laser wavelength of $\lambda < 637\,\text{nm}$. As mentioned above, the excitation wavelength influences the ratio between the NV^0 and NV^- population. Experiments [82] have determined that the most efficient wavelength to excite the NV whilst having the largest NV^-/NV^0 ratio lies between 510 nm and 540 nm. We choose then to work with an excitation laser with $\lambda = 532\,\text{nm}$, where high power stable lasers are readily available. When an excitation photon is absorbed, the state is excited above the ^3E level to an upper vibrational state, from which it quickly relaxes back to the one of the ^3E spin states. The state can then follow two decay paths: either a radiative transition to the $^3A_2$ ground state or a non-radiative transition to ^1E followed by a radiative transition to $^1A_1$. The two singlet states are known as shelving states and the spin-dependent transition from excited to ground state through the shelving states is called inter-system crossing (ISC). When the state is in $^1A_1$, it undergoes a dark transition to the ground state. The

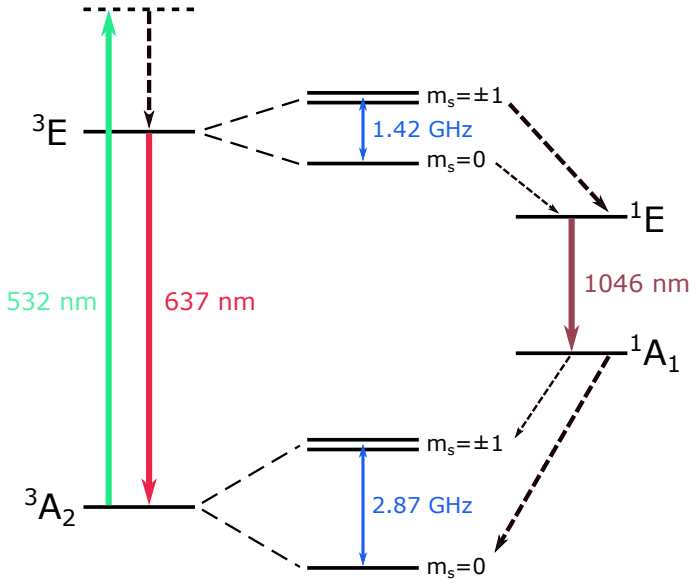

Figure 2.3: Energy level structure of the NV centre at room temperature. An optical ground state (^{3}A$_2$) can be excited to the excited ^{3}E state with off-resonant excitation at 532 nm (green arrow). The two levels are spin $S = 1$ manifolds. The degeneracy is removed by spin-spin interaction, which create a $m_s = 0$ ground state and two $m_s = \pm 1$ high energy states. The zero field splittings are $D_{gs} = 2.87$ GHz for the ^{3}A$_2$ and $D_{es} = 1.42$ GHz for ^{3}E. The optical excited state can decay back to ^{3}A$_2$ emitting photons with a zero-phonon line $\lambda_{ZPL} = 637$ nm (red arrow) or can decay non-radiatively (dashed lines) to a $S = 0$ ^{1}A$_1$ state, which further decays to a $S = 0$ ^{1}A level emitting infrared photons ($\lambda = 1046$ nm, brown arrow) and finally decays back non-radiatively to the ground state. Thicker lines dashed lines indicate faster decay rates.

relative decay rates of the two paths, which are dependent on the spin state, and the presence of the ISC are fundamental to control and read out the NV centre.

Because of the weak spin-orbit coupling of the NV centre, the electric dipole transitions are primarily spin-conserving, with spin-flip radiative transition rates being 2% of the spin-conserving rates [91]. As mentioned above, the relaxation rates into the different levels are dependent on the spin. The $m_s = 0$ excited state preferentially undergoes a radiative transition to the ground state, whereas the dark transition to the shelving state is slower. On the other hand, the decay rates from $m_s = \pm 1$ to the ground state and to the ISC have similar magnitudes. The ^{1}A$_1$, which has a lifetime of few hundreds of nanoseconds, couples at approximately the same rate to $m_s = 0$ and $m_s = \pm 1$ in the ground state. Consequently, after few cycles of excitation and decay the quantum states is polarised into the $|^3\text{A}_2, m_s = 0\rangle$ state of the system. At room temperature, the degree of polarisation with off-resonant excitation can reach up to $\sim 80\%$ [92].

The spin-dependent decay rates into both the ^{3}A$_2$ or into the shelving states are also fundamental to read out the NV centre. The $m_s = 0$ of the optically excited state ^{3}E, which decays preferentially emitting photons, yields a higher fluorescence

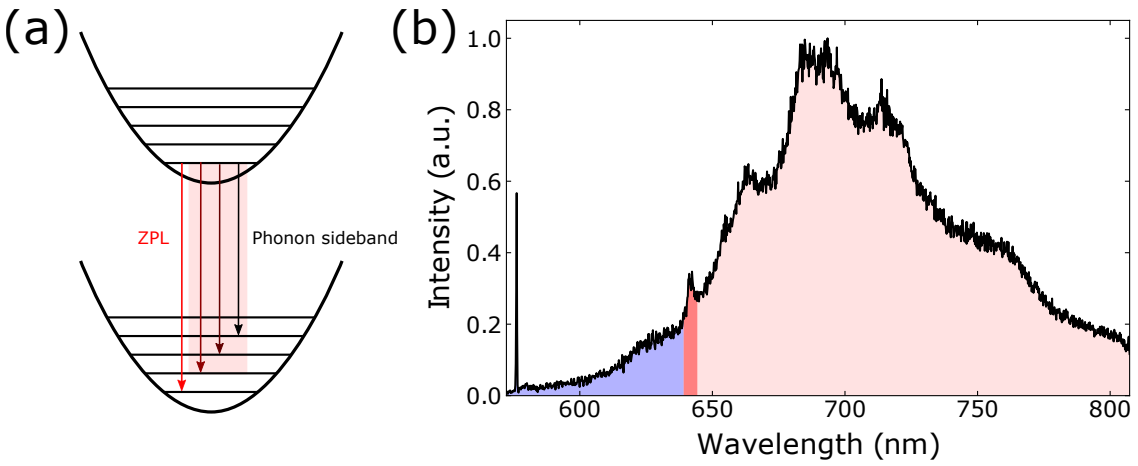

Figure 2.4: NV emission spectrum. (a) Depiction of the relaxation from the excited state to the vibrational levels of the optical ground state. When the population is in the excited optical state and in the vibrational grounds state, it couples with different strengths to the different vibrational levels of the optical ground state. This gives rise to a spectral phonon sideband at lower energies than the zero-phonon line. (b) Typical spectrum of an NV centre in bulk diamond at room temperature, measured on one of our diamond tips 5. The ZPL peak is located at $\lambda_{ZPL} \sim 637\,\text{nm}$. The peaks at lower energies correspond to different vibrational transitions. The sharp peak at $\lambda = 575\,\text{nm}$ corresponds to the Raman line of diamond for an excitation wavelength $\lambda = 532\,\text{nm}$.

rate compared to the $m_s = \pm 1$ level. This means that in a scheme of averaged readout [93] one can distinguish the spin state by applying off-resonant excitation and reading out the intensity of the NV fluorescence. As I will discuss in the next section, this readout technique is fundamental to perform scanning NV magnetometry.

Although the ZPL of the NV centre is $\lambda_{ZPL} = 637\,\text{nm}$, the fluorescence spectrum is distributed from $\sim 600\,\text{nm}$ to $\sim 800\,\text{nm}$. The origin of such a broad emission spectrum is attributed to the lattice vibrations coupled to the NV centre. Within the Born-Oppenheimer approximation, which assumes that the nuclear coordinates do not change on the time scale of an electronic optical transition, the intensity of the decay (absorption) from a defined vibrational state in the excited state (ground state) is proportional to the overlap integral between the excited state and ground state electronic wavefunctions. The strongest transition is thus the one which leaves the nuclear coordinates unchanged (Fig. 2.4(a)). In the NV centre case, the ZPL does not correspond to the most allowed transition and it accounts only for 4% of the total emitted photons, even at cryogenic temperatures [90]. Depending on the NV environment, i.e. whether the NV is found in a bulk diamond matrix or within a nanodiamond, three or more phonon sidebands are resolvable (Fig. 2.4(b)).

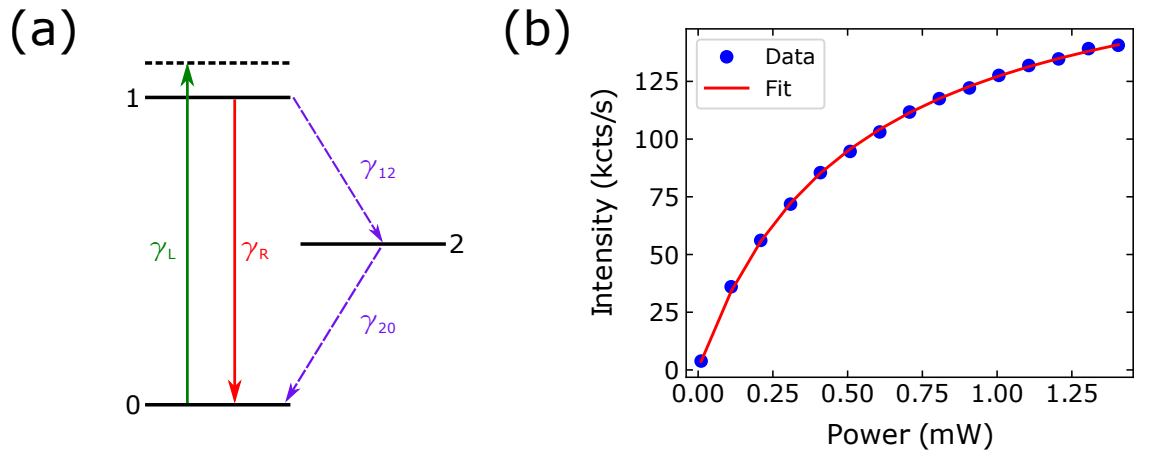

Figure 2.5: NV power saturation. (a) Three-level system model used to compute the fluorescence dependence on optical excitation power. The solid arrows are optical transitions, the dashed arrows are non-radiative transitions. (b) Experimentally acquired saturation curve of a single NV centre, fitted with equation 2.4.

2.1.1 Power dependence of the NV fluorescence

The fluorescence of an NV as a function of power is non-linear, since the NV is an optically-addressable multi-level system. When the optical excitation rate is much larger than the decay rates in the system the fluorescence rate saturates to a constant value. A three-level system model can be developed to capture the response of the NV as a function of green excitation power (Fig. 2.5(a)). The corresponding rate equations are:

$$\frac{\mathrm{d}n_0}{\mathrm{d}t} = -\gamma_L n_0 + \gamma_{rad} n_1 + \gamma_{20} n_2 \ , \tag{2.1}$$

$$\frac{\mathrm{d}n_1}{\mathrm{d}t} = \gamma_L n_0 - \gamma_{rad} n_1 - \gamma_{12} n_1 \ , \tag{2.2}$$

$$n_0 + n_1 + n_2 = 1 \ . \tag{2.3}$$

Solving for the steady-state solution yields the population in the excited state, which when multiplied by the optical decay rate yields the fluorescence rate I of the NV centre as a function of laser power P [94]:

$$I(P) = I_\infty \frac{P}{P + P_s} \ , \tag{2.4}$$

where $I_\infty = \gamma_r^2 \gamma_{20}/(\gamma_{20} + \gamma_{12})$ is the maximum emission rate and $P_s \propto \gamma_{20}(\gamma_r + \gamma_{12})/(\gamma_{20} + \gamma_{12})$ is the saturation power. A typical saturation curve is shown in Figure 2.5(b).

Even if the fluorescence saturation has no direct application for quantum sensing,

it is still important to consider during measurements. When the pump rate is high, most of the population gets trapped in the shelving state. The optical ground state gets depopulated and the population difference between $m_s = 0$ and $m_s = \pm 1$ decreases. For experiments where continuous-wave laser excitation is used the spin readout contrast is reduced at high optical powers, effectively decreasing the signal-to-noise ratio (SNR). This is because when the pump rate is high the electron population is high in the shelving state and reduced in the $|^3\mathrm{A}_2, 0\rangle$ and $|^3\mathrm{A}_2, \pm 1\rangle$ states typically used for sensing.

2.2 Ground-state Hamiltonian

As mentioned in the previous section, the ground state of the NV centre is a spin triplet. Spin-spin interactions lift the degeneracy of the $m_s = 0$ state, which is the lowest energy state at zero magnetic field, and the $m_s = \pm 1$ levels. Adding the interaction with the crystalline fields and the Zeeman interaction, the Hamiltonian takes the form [95]:

$$\mathscr{H} = hD\left(S_z^2 - \frac{2}{3}D\right) + hE\left(S_x^2 - S_y^2\right) + h\tilde{\gamma}\,\mathbf{B}\cdot\mathbf{S}\,, \tag{2.5}$$

where the zero-field splitting $D = 2.87\,\mathrm{GHz}$, E is a parameter in units of Hz which is changed by the local off-axis strain field, h is the Planck constant, $\tilde{\gamma} = \gamma/(2\pi) \simeq 28.025\,\mathrm{GHz/T}$ and γ is the gyromagnetic ratio for the free electron, $\mathbf{S} = (S_x,\, S_y,\, S_z)$ is the vector of Pauli operators and $\mathbf{B}$ is an external magnetic field. I neglect the on-axis strain in this expression since it is usually small and it has the effect of changing the D parameter. The $\hat{z}$ unit vector lies on the symmetry axis of the NV centre, pointing along the vector connecting the nitrogen atom to the vacancy atom. The E parameter depends on the NV diamond host. In bulk diamond $E < 2\,\mathrm{MHz}$ usually, while in nanodiamonds it can vary a lot, typically between 5 MHz and 20 MHz.

As mentioned above, the parameter D represents the spin-spin interactions between the two NV electrons. Hence, this parameter is influenced by the volume of the wave function and thus by temperature. An expansion of the lattice due to an increasing temperature results in a reduction of the zero-fields splitting. Conversely, a decreasing temperature increases the spin-spin interaction, resulting in a larger D. This effect forms the basis of temperature sensing with NV centres [96]. I also point out that the Hamiltonian in Equation 2.5 neglects the effect of external electric fields. The presence of the latter can induce further shifts to the zero-field splitting and introduces a coupling term between the two upper levels of the ground

state manifold [97]. However, electric fields are not present in the NV magnetometry applications discussed in this work and are therefore neglected.

Knowing the form of the Hamiltonian allows us to study the energies of the eigenstates as a function of an externally applied magnetic field, and thus the evolution of the two ODMR spectral lines ν_- and ν_+ can be extracted. The eigenvalues of the Hamiltonian as a function of $\mathbf{B}$, D and E can be obtained by solving the corresponding secular equation. However, the solutions are complex and do not offer much insight in the physics of the NV centre. I will consider the limiting cases in the following discussion.

2.2.1 Zero-field and weak off-axis field regime

When the only perturbation along the quantisation axis is a magnetic field, the Hamiltonian depends only on the azimuthal angle ϑ between NV axis and magnetic field vector and not on the equatorial angle φ. Equation 2.5 can be more conveniently rewritten in terms of off-axis (perpendicular to the NV symmetry axis) and on-axis (parallel to the NV symmetry axis) magnetic fields as:

$$\mathscr{H} = hD\left(S_z^2 - \frac{2}{3}D\right) + hE\left(S_x^2 - S_y^2\right) + h\tilde{\gamma}\,\mathbf{B}_\perp \cdot \mathbf{S}_\perp + h\tilde{\gamma}\,B_z S_z\,, \tag{2.6}$$

where $\mathbf{B}_\perp = (B_x,\, B_y)$ and $\mathbf{S}_\perp = (S_x,\, S_y)$.

When $\mathbf{B}_\perp \ll D$ and $\mathbf{B}_\perp \ll B_z$, the contribution of the off-axis magnetic field can be neglected and one can work in the so-called weak-field regime. In this regime, the quantisation axis is set by the zero-field splitting, which constitutes the intrinsic quantisation axis of the NV centre. For this reason, I can write the eigenvectors of the Hamiltonian as linear combination of the eigenbasis $\{|0\rangle, |-1\rangle, |+1\rangle\}$, formed by the eigenvectors of S_z. The eigenstates are:

$$\begin{cases} |G\rangle = |0\rangle \\ |-\rangle = \dfrac{1}{\sqrt{2\left(\tilde{B}^2 + E^2 + \tilde{B}\sqrt{\tilde{B}^2 + E^2}\right)}}\left(E\,|1\rangle - \left(\tilde{B} + \sqrt{\tilde{B}^2 + E^2}\right)|-1\rangle\right) \\ |+\rangle = \dfrac{1}{\sqrt{2\left(\tilde{B}^2 + E^2 + \tilde{B}\sqrt{\tilde{B}^2 + E^2}\right)}}\left(\left(\tilde{B} + \sqrt{\tilde{B}^2 + E^2}\right)|1\rangle + E\,|-1\rangle\right) \end{cases} \tag{2.7}$$

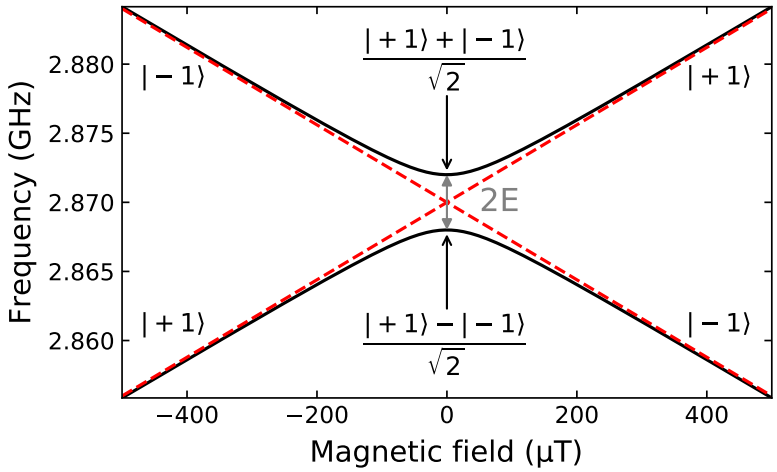

Figure 2.6: Ground state transition frequencies as a function of a magnetic field applied along the NV axis. The solid black lines are the solution for $D = 2.87\,\text{GHz}$ and $E = 2\,\text{MHz}$. The dashed red lines are the solution in the case of $E = 0$.

with eigenvalues:

$$\begin{cases} \nu_0 = -\dfrac{2}{3}D \\ \nu_- = \dfrac{D}{3} - \sqrt{\tilde{B}^2 + E^2} \\ \nu_+ = \dfrac{D}{3} + \sqrt{\tilde{B}^2 + E^2} \end{cases} \tag{2.8}$$

where $\tilde{B} = \tilde{\gamma} B_z$. At zero field, the degeneracy between the $|-1\rangle$ and the $|+1\rangle$ levels is lifted by the off-axis strain. The two transition energies are split by $2E$ and the eigenstates are linear superpositions of the $|\pm 1\rangle$ states. The E parameter effectively induces an avoided crossing at zero-field. Hence, the states at zero-field are robust against weak perturbations induced by an external magnetic field. In the regime where $\tilde{\gamma} B_{stray} \simeq E$, the response to magnetic fields is not optimal, since $\mathrm{d}\nu_\pm/\mathrm{d}B = \pm\tilde{B}/\sqrt{\tilde{B}^2 + E^2}$. When $\tilde{B} \gg E$, the quantisation axis is completely determined by the magnetic field and thus lies along the NV axis. The magnetic field Hamiltonian in this scenario commutes with the S_z operator and the common eigenstates are $|0\rangle$, $|-1\rangle$ and $|+1\rangle$ (Fig. 2.6), while the transition energies are linear with the applied magnetic field.

This has important consequences for NV magnetometry. If the stay field produced by the object under study is too weak, the NV sensor might not respond to it because it is protected by the strain energy. A bias field is thus required to bring the NV centre the regime where the transition frequencies are linearly dependent with the magnetic field, which corresponds to the highest sensitivity. It is preferable to choose NVs which show low strain splitting, since strong bias fields can perturb a

sample (i.e. a ferromagnetic thin film). This is particularly important for NV centres in nanodiamonds, where it is not uncommon to find strain fields up to 20 MHz.

2.2.2 Non-zero off-axis field regime

In the more general case of a magnetic field with arbitrary magnitude and angle ϑ relative to the NV axis, the magnetic field does not commute with the S_z operator and thus the spin-projection quantum number is no longer a good quantum number. The analytical function describing the eigenfrequencies for arbitrary $\tilde{B} = \tilde{\gamma}\,|\mathbf{B}|$ and ϑ can be obtained solving the secular equation [48]:

$$\lambda^3 - \left(\frac{D^2}{3} + \tilde{B}^2 + E^2\right)\lambda - \frac{\tilde{B}^2}{2}\Delta - \frac{D}{6}\left(\tilde{B}^2 + 4E^2\right) + \frac{2}{27}D^3 = 0\,, \tag{2.9}$$

where $\Delta = D\cos(2\vartheta) + 2E\cos(2\varphi)\sin^2(\vartheta)$. The full analytical solution is presented in Appendix A, as it is symbolically heavy and does not give further insights in the physics of the NV. Here I will discuss the effects that an arbitrary magnetic field has on the NV centre.

In the case of very large magnetic fields, the quantisation axis is no longer determined by the zero-field splitting but it is defined by the direction of the magnetic field vector. A consequence of this is that also the ground state $|0\rangle$ is no longer an eigenstate of the full Hamiltonian (Fig. 2.7(b)). As I will discuss later (Sec. 2.6), this affects the branching ratios of the decay paths from the excited state and consequently modifies the photodynamics of the NV centre. In this regime, the eigenfrequencies are no longer symmetric with the zero-field splitting D. As shown in Figure 2.7(a), when the magnitude of the magnetic field vector and its angle relative to the NV axis are large enough, the resonance frequencies of the NV not only split but they also shift to larger frequencies. For example, in the extreme case where the magnetic field is fully perpendicular to the NV axis and $\tilde{B} \gg D$, the eigenstates are:

$$\begin{cases} |G\rangle = \dfrac{1}{\sqrt{2}}|0\rangle + \dfrac{1}{2}\left(|-1\rangle + |+1\rangle\right) \\ |-\rangle = \dfrac{1}{\sqrt{2}}\left(|+1\rangle - |-1\rangle\right) \\ |+\rangle = \dfrac{1}{\sqrt{2}}|0\rangle - \dfrac{1}{2}\left(|-1\rangle + |+1\rangle\right) \end{cases} \tag{2.10}$$

The converse problem of extracting the magnetic field amplitude and angle given the two transition frequencies $\bar{\nu}_+$ and $\bar{\nu}_-$ is also of interest in an experimental scenario

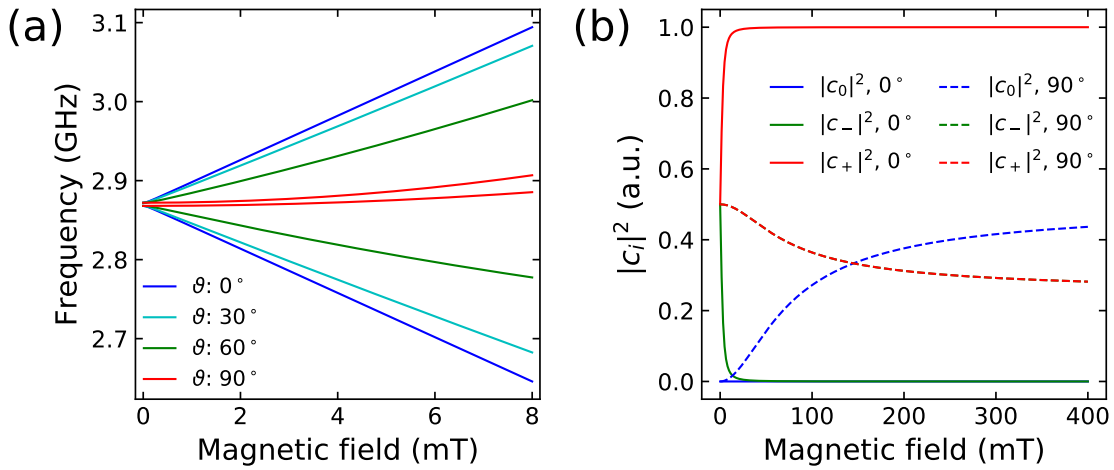

Figure 2.7: (a) Magnetic field-dependent ground state transition lines for different angles ϑ between magnetic field and NV axis, with $E = 2\,\text{MHz}$. When $\vartheta = 0°$, the magnetic field splits the two transitions symmetrically with respect to the zero-field splitting $D = 2.87\,\text{GHz}$. When the magnetic field is not aligned with the NV axis, the splitting is smaller than $\vartheta = 0°$ at fixed magnetic field value. The two transition lines also have an increasingly large common shift towards higher frequencies. (b) Squared moduli of the coefficients of the highest energy state, written as $|+\rangle = c_0\,|0\rangle + c_-\,|-1\rangle + c_+\,|+1\rangle$, for a magnetic field aligned along the NV axis (solid line) and a field at 90° (dashed line). When the off-axis component is large, the new eigenstates are superpositions of all the three S_z eigenstates. The dashed red and green lines are overlapped.

where the only known quantities are the two NV resonance frequencies. Knowing that the Hamiltonian is Hermitian, the eigenvalues are linked to each other by three equations (Appendix. A), which can be solved to obtain the relationship between magnetic field and resonance frequencies:

$$\begin{cases} \tilde{B}^2 = \dfrac{1}{3}\left(\bar{\nu}_-^2 + \bar{\nu}_+^2 - \bar{\nu}_-\bar{\nu}_+ - D^2\right) - E^2 \\ \Delta = \dfrac{7D^3 + 2(\bar{\nu}_+ + \bar{\nu}_-)\left[2(\bar{\nu}_+^2 + \bar{\nu}_-^2) - 5\bar{\nu}_-\bar{\nu}_+ - 9E^2\right] - 3D(\bar{\nu}_+^2 + \bar{\nu}_-^2 - \bar{\nu}_-\bar{\nu}_+ + 9E^2)}{27\tilde{B}^2} \end{cases} \tag{2.11}$$

In the assumption that $D \gg E$, $\Delta \approx D\cos(2\vartheta)$, with these two equations one can extract $|\mathbf{B}|$ and ϑ.

2.2.3 Hyperfine structure

While the first-order perturbation to the zero-field Hamiltonian is given by the Zeeman interaction, there is another term that modifies the behaviour of the NV centre: the hyperfine interaction. The electron spin of the NV centre is localised at the defect site and thus interacts strongly with the nitrogen spin. The most abundant nitrogen isotope is ^{14}N (relative abundance: 99.96%), with nuclear spin $I = 1$, but it is possible to find NVs which contain ^{15}N, with $I = 1/2$. The additional

interaction term reads as [98]:

$$\mathscr{H}_{HF} = hP\left(I_z^2 - \frac{I(I+1)}{3}\right) + hA_{\parallel}\, S_z I_z + hA_{\perp}\, (S_x I_x + S_y I_y)\ , \tag{2.12}$$

where P is the electric quadrupole splitting parameter, (I_x, I_y, Iz) are the Pauli operators for the nuclear spin, $A_{\parallel}$ and $A_{\perp}$ are the axial and perpendicular hyperfine interaction terms, respectively. In the case of ^{14}N, $P \simeq -4.95\,\mathrm{MHz}$ [99], $A_{\parallel} \simeq -2.16\,\mathrm{MHz}$ [99] and $A_{\perp} \simeq -2.62\,\mathrm{MHz}$ [34]. ^{15}N has $P = 0\,\mathrm{MHz}$, since it is a $I = 1/2$ system, and $A_{\parallel} = A_{\perp} \simeq -3.05\,\mathrm{MHz}$ [100]. The nuclear Zeeman interaction term is neglected, since the nitrogen nuclear magnetic moment is approximately three orders of magnitude weaker than the electron magnetic moment.

The addition of the hyperfine coupling further splits the levels. The number of observable transition lines which varies depending on the external magnetic field. At large on-axis bias field, the transition lines within each manifold are split by $\delta\nu \simeq 2.2\,\mathrm{MHz}$ for ^{14}N. When performing NV magnetic field sensing with continuous wave (CW) excitation the perturbation of the hyperfine interaction has only marginal importance, affecting the linewidth of the resonance. The control over the hyperfine levels is of importance when sensing time-dependent (AC) magnetic fields, i.e. when performing coherent control of the spin states. In this case the level anti-crossings induced by the hyperfine interaction can be used to optically polarise the nuclear spin state, yielding a larger sensitivity to magnetic fields [101].

2.3 Optically detected magnetic resonance

The most simple spin readout experiments which can be performed on the NV is optically detected magnetic resonance (ODMR), which takes advantage of the NV spin-dependent fluorescence rate. As mentioned in the previous section, the transitions between the $m_s = 0$ and the $m_s = \pm 1$ levels in the ground state are separated by 2.87 GHz. These two transitions are electric-dipole forbidden and the strongest allowed transition has a magnetic-dipole character. If a continuous 532 nm laser excitation is applied to the NV, the population is pumped into the $m_s = 0$ state. While monitoring the fluorescence counts, the frequency of a continuous microwave excitation is scanned across the $m_0 \rightarrow m_{-1}$ ($m_0 \rightarrow m_1$) transition. When the microwave frequency is in resonance with the one of the two transitions, part of the steady-state population is transferred to the $m_s = \pm 1$ levels in the ground state. The resulting drop in fluorescence caused by the ISC reveals the exact frequency of the transition.

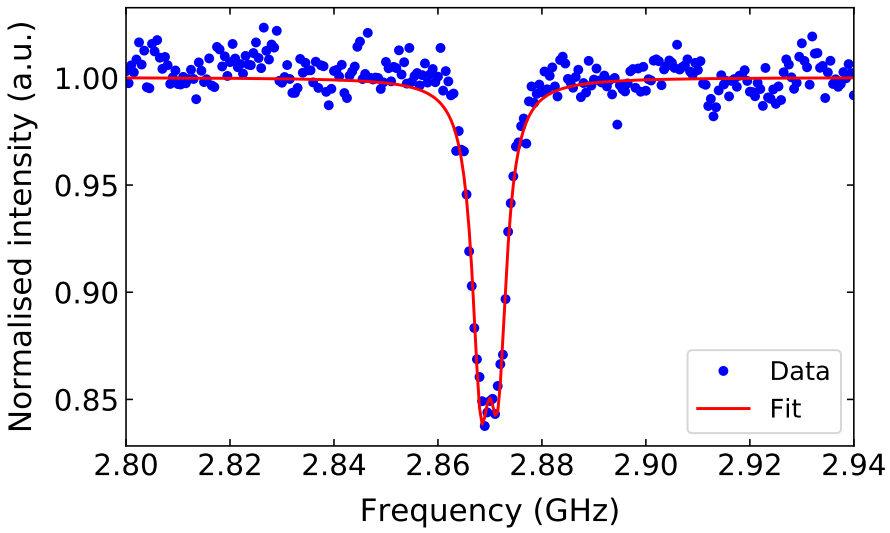

Figure 2.8: ODMR spectrum of a single NV centre, with a microwave excitation power of 23 dBm, using an optical excitation power below the saturation power. The two dips, split by $E = 1.6 \pm 0.1$ MHz, correspond to the two magnetic-dipole transitions within the ground state manifold.

A typical ODMR spectrum is presented in Figure 2.8. The transition frequencies can be modified by magnetic and electric fields (including crystal strain). Typically, the ODMR contrast is around 15% but can reach up to 30% in optimal microwave-NV coupling conditions. The contrast is also affected by the laser pumping rate. If the excitation power is well above saturation, most of the steady-state population gets trapped into the shelving state, thus decreasing the OMDR contrast. The relative amplitude of the two dips can be modified by the polarisation of the microwave excitation.

The linewidth of the ODMR resonance is fundamentally limited by the inverse of the spin-lattice relaxation time T_2^* [102] (Sec. 2.4.3). For this reason, the ODMR linewidth is strongly influenced by the local environment of the NV centre. It is narrower for NV centres implanted in bulk diamond samples, where typically $T_2^* \sim 20\,\mu$s, compared to NV centres in nanodiamonds, where $T_2^* \sim 5\,\mu$s. However, this limit can be never reached when using continuous-wave excitation. Additional broadening is given by the power broadening induced by the laser and microwave fields. The linewidth can also be influenced by samples which contain magnetic material. The increase in low-frequency magnetic noise at the NV site due to the proximity with a magnetic object deteriorates the T_2^* and thus increases the linewidth.

The relative contrast between the two peaks is also affected by the eigenstates of the NV centre, which, as we have seen in the previous section, are modified by strain

and magnetic field. When the set of eigenstates is $\{|0\rangle, |-1\rangle, |+1\rangle\}$, the transitions $|G\rangle \rightarrow |-\rangle$ and $|G\rangle \rightarrow |+\rangle$ couple to σ_-- and σ_+-polarised microwave excitation, respectively. The plane in which the magnetic field rotates is perpendicular to the NV axis. At zero field, however, the states $|+\rangle$ and $|-\rangle$ are linear superpositions of the $|-1\rangle$ and $|+1\rangle$ states. In this case the low and high energy transitions couple to V- and H-polarised microwave excitation, respectively. This picture is further complicated when the plane in which the microwave field lies is not perpendicular to the NV axis. In the general case, the two NV transitions couple to elliptically-polarised microwave excitation (Appendix A).

2.4 Coherent control of the spin state

In addition to the so-called DC sensing, which relies on CW fields and on the detection of the steady state of the NV centre, coherent control of the NV spin can be used for sensing of (typically time-independent) magnetic fields.

Restricting ourselves to one of the two ground state resonances, the system can be described as a two-level system to a good approximation, if the two upper levels are only split by a few MHz. I denote as $|g\rangle$ the lowest-energy state of the NV ground state manifold and $|e\rangle$ one of the two higher-energy states. The $|g\rangle$ and $|e\rangle$ levels are split by the energy $\hbar\omega_0$. In this picture, the unperturbed Hamiltonian is:

$$\mathscr{H}_0 = \hbar\omega_0 |e\rangle\langle e| \ , \tag{2.13}$$

and the general quantum state in the restricted Hilbert space is described as:

$$|\psi(t)\rangle = c_g(t)\,|g\rangle + c_e(t)\,|e\rangle \ . \tag{2.14}$$

I then add a quasi-resonant magnetic field excitation at frequency ω. For the sake of simplicity, I assume that the magnetic field is linearly polarised along the x axis. The time-dependent interaction Hamiltonian (in the Schrödinger picture) then reads:

$$\mathscr{H}_I = -\boldsymbol{\mu}\cdot\mathbf{B}_0\cos(\omega t) = \hbar\Omega\,\cos(\omega t)\,(|e\rangle\langle g| + |g\rangle\langle e|) \equiv \hbar\Omega\cos(\omega t)\,\sigma_x \ , \tag{2.15}$$

where $\Omega = \langle g|\boldsymbol{\mu}\cdot\mathbf{B}_0|e\rangle/\hbar$ is the Rabi frequency. In the interaction picture, the σ_x operator contains terms which evolve as $e^{i(\omega\pm\omega_0)t}$. Assuming that $|\omega-\omega_0| \ll \omega+\omega_0$, I can apply the so-called rotating-wave approximation (RWA) and neglect the terms that evolve as $e^{i(\omega+\omega_0)t}$. The Hamiltonian in the Schrödinger picture and with the

RWA is then modified as:

$$\mathscr{H}_I^{\mathrm{RWA}} = \frac{\hbar\Omega}{2}\left[\sigma_x \cos(\omega t) + \sigma_y \sin(\omega t)\right] \ . \tag{2.16}$$

Notice that, since a linearly polarised field along x can be rewritten as the sum of two orthogonal circularly polarised microwaves $(\sigma_+ + \sigma_-)/\sqrt{2}$, applying the RWA means that only the excitation which conserves the total angular momentum of the system can couple the ground state to the excited state. I also define a new pair of coefficients:

$$\begin{cases} \tilde{c}_g(t) = c_g(t) \ , \\ \tilde{c}_e(t) = c_e(t) e^{i\omega t} \ . \end{cases} \tag{2.17}$$

This corresponds to transforming the state 2.14, defined in the "laboratory frame", to the frame which rotates together with the microwave excitation. Applying the full Hamiltonian to this state yields two coupled differential equations for the time-dependent coefficients:

$$\begin{cases} i\dot{\tilde{c}}_g(t) = \dfrac{\Omega}{2}\,\tilde{c}_e(t) \ , \\ i\dot{\tilde{c}}_e(t) = -\delta\,\tilde{c}_e(t) + \dfrac{\Omega}{2}\,\tilde{c}_g(t) \ , \end{cases} \tag{2.18}$$

where $\delta = \omega - \omega_0$ is the detuning of the microwave excitation from the resonance. Given the initial conditions $\tilde{c}_g(0)$ and $\tilde{c}_e(0)$, the solution to the differential equations reads:

$$\begin{cases} \tilde{c}_g(t) = e^{i\delta t/2}\left[\tilde{c}_g(0)\cos\left(\dfrac{\tilde{\Omega}}{2}t\right) - \dfrac{i}{\tilde{\Omega}}\left[\delta\tilde{c}_g(0) + \Omega\tilde{c}_e(0)\right]\sin\left(\dfrac{\tilde{\Omega}}{2}t\right)\right] \ , \\ \tilde{c}_e(t) = e^{i\delta t/2}\left[\tilde{c}_e(0)\cos\left(\dfrac{\tilde{\Omega}}{2}t\right) + \dfrac{i}{\tilde{\Omega}}\left[\delta\tilde{c}_e(0) - \Omega\tilde{c}_g(0)\right]\sin\left(\dfrac{\tilde{\Omega}}{2}t\right)\right] \ , \end{cases} \tag{2.19}$$

where $\tilde{\Omega} = \sqrt{\Omega^2 + \delta^2}$ is the generalised Rabi frequency. The spin dynamics can then be described as trajectories in a Bloch sphere. The two poles correspond to the $|g\rangle$ and $|e\rangle$ states, while the states on the equator correspond to the superposition states $\left(|e\rangle + e^{i\varphi}|g\rangle\right)/\sqrt{2}$. The states with $\varphi = 0$ and $\varphi = \pi/2$ define the x and the y axis, respectively. The effect of the AC magnetic field in the laboratory frame is equivalent to a static effective magnetic field in the rotating frame, around which the state precesses. When the excitation frequency is on resonance with the transition, the effective magnetic field lies on the equator or the Bloch sphere. When $|\delta| > 0$, it forms an angle with the Bloch sphere axis and if $|\delta| \to \infty$ it points towards the

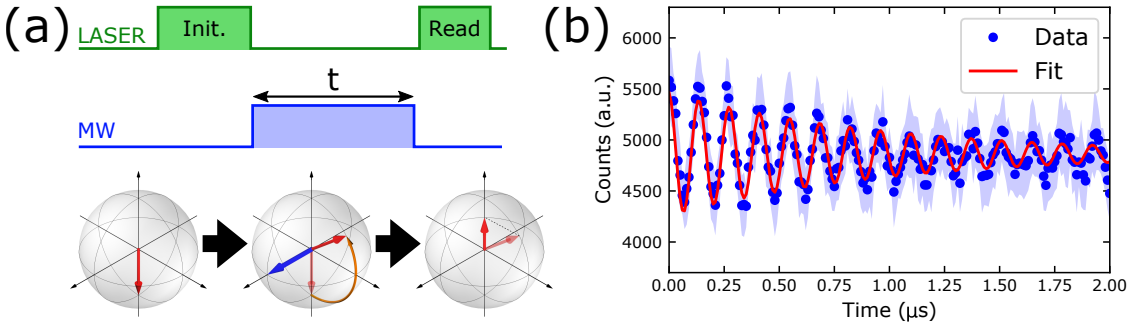

Figure 2.9: Rabi oscillations. (a) Pulse sequence for Rabi oscillations on NV centres. A long green laser pulse intialises the spin state in the ground state, followed by $300ns$ of dark time to allow the population in the shelving state to decay to the $|0\rangle$ level in the ground state. Subsequently, a microwave pulse of variable length rotates the Bloch vector in the Bloch sphere. (b) Experimental Rabi oscillations measured on an NV centre. The shaded indicates the ± 1 standard deviation from the mean (blue) obtained from 50 repetitions of the experiment.

pole.

2.4.1 Rabi oscillations

If the initial conditions are $\tilde{c}_g(0) = 1$, $\tilde{c}_e(0) = 0$, using Equation 2.19 yields the population in the excited state evolves as:

$$|\tilde{c}_e(t)|^2 = \frac{\Omega^2}{\tilde{\Omega}^2} \sin^2\left(\frac{\tilde{\Omega}}{2}t\right) . \tag{2.20}$$

Notably, the detuning from the resonance affects the oscillations. When $|\delta| \gtrsim \Omega$, the frequency of the oscillations is increased compared to the case where $\delta = 0$, whereas the amplitude is decreased. The evolution of the population is known as Rabi oscillation and it is at the heart of protocols for the coherent control of spins. Rabi oscillations on NV centre were first observed in 2004 by Jelezko et al. [30]. The experimental sequence relies on laser and microwaves pulses to manipulate the NV spin, as shown in Figure 2.9(a). An initial laser pulse pumps the spin into the $m_s = 0$ state, followed by a dark time which allows for the remaining population trapped in the shelving state to decay into the ground state. A microwave pulse of increasing length is applied to rotate the NV on the Bloch sphere and a final laser pulse reads the NV state $|\psi\rangle$. The fluorescence signal S is proportional to $|\langle\psi|0\rangle|^2$ (Fig. 2.9(b)).

Rabi oscillations can be used to experimentally measure the driving time required to rotate the state to a given angle in the Bloch sphere. The pulse of width t_π such that $\Omega t_\pi = \pi$ is referred to as π-pulse and it corresponds to the driving required to

flip the spin from one pole to the other. On the contrary, a $\pi/2$-pulse has width $\Omega t_{\pi/2} = \pi/2$ and rotates the state from a pole onto the equator of the Bloch sphere. These two pulses are the most commonly used in protocols for magnetic field sensing, as I will discuss later in the text.

2.4.2 Pulsed ODMR

As discussed in Section 2.1.1 and Section 2.3, the linewidth of the CW ODMR is influenced by the laser power and the microwave excitation power. The sensitivity of the ODMR sequence is proportional to the linewidth of the resonance and its depth (Sec. 2.4.3). With CW sensing, it is impossible to reach the ultimate linewidth limit, set by $1/T_2^*$ [102]. Pulsed ODMR allows us to overcome the limits imposed by CW excitation.

The sequence is described in Figure 2.10(a). After the laser initialisation pulse, a microwave pulse is scanned in frequency. The spin state is then read out with a short laser pulse. The microwave pulse width can be optimised to a π-pulse width to achieve maximum spin-flip probability. With this sequence the laser power broadening contribution is removed, since ODMR is performed in dark conditions and the laser pulses are used only to initialise and read out the spin state. In pulsed conditions, the ODMR linewidth mainly depends on the Fourier-transform of the pulse. The longer the pulse, the narrower its width in the frequency domain. This allows to achieve linewidths limited by the $1/T_2^*$ limit.

2.4.3 Ramsey interferometry

Another widely used technique for sensing DC magnetic fields is Ramsey interferometry, first introduced to measure the transition frequencies in molecular beam resonance experiments [103]. The pulse sequence between the laser initialisation and readout pulses is $\pi/2 - \tau - \pi/2$, where τ is the delay between the two $\pi/2$ pulses (Fig. 2.10(a)). The first pulse rotates the state to the equator of the Bloch sphere, while the last rotates it back onto the measurement basis. After the first $\pi/2$-pulse, the quantum state is sensitive to magnetic fields along the z axis. These rotate the original Bloch vector around the axis of the Bloch sphere to a new state $(|0\rangle + e^{i\varphi}|-1\rangle)/\sqrt{2}$. φ is the phase accumulated by the $|-1\rangle$ state during the Ramsey delay time τ:

$$\varphi = \gamma \int_0^\tau B_z(t)\mathrm{d}t \ . \tag{2.21}$$

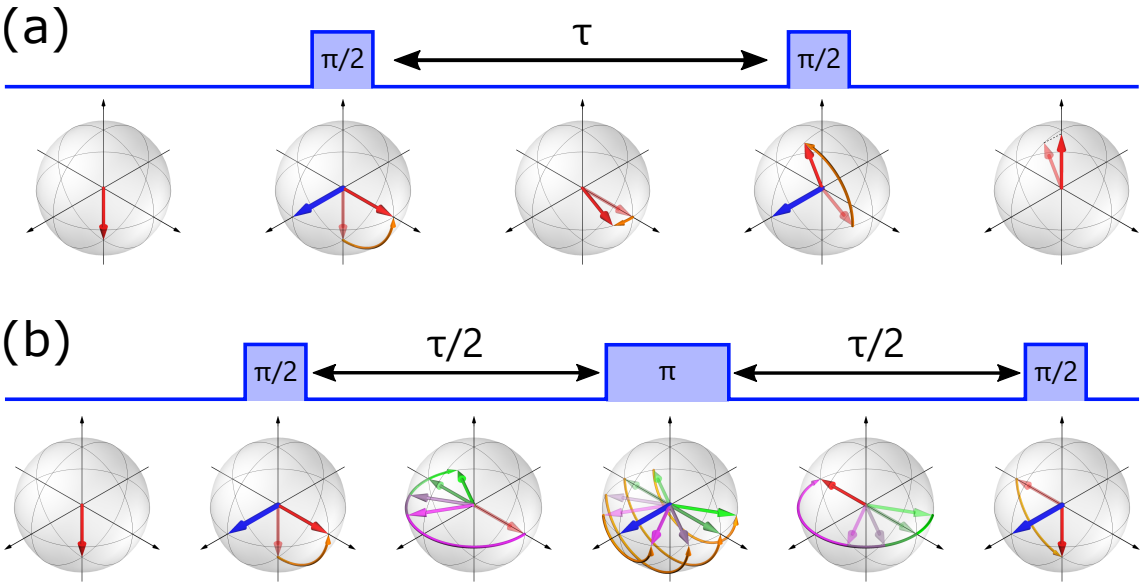

Figure 2.10: Ramsey and spin-echo sequences. (a) Ramsey sequence. After spin initialisation, a microwave $\pi/2$ pulse rotates the Bloch vector onto the Bloch sphere equator. During the waiting time τ, the vector will pick up a phase if there are slowly-varying fields along the z-axis. A final $\pi/2$ pulse is applied and a laser pulse (not shown) projects the state onto the z-axis. (b) Spin-echo sequence. After spin initialisation, a microwave $\pi/2$ pulse rotates the Bloch vector onto the Bloch sphere equator. During the waiting time $\tau/2$, time-dependent magnetic fields along the z-axis will induce different phase phase shifts of the Bloch vector state during multiple runs. A π pulse mirrors the Bloch vector with respect to the yz-plane. The Bloch vector is refocussed after a waiting time $\tau/2$ and then rotated back into the z-axis by a $\pi/2$ pulse.

If $B_z(t)$ is constant, the projection measurement after the last $\pi/2$ pulse as a function of time gives a signal oscillating with the Larmor frequency γB_z. While this is true for an ideal two-level system, the electron spin levels are split by the hyperfine interaction with ^{14}N giving two additional transitions at higher and lower energy detuned by 2.2 MHz from the $|0,0\rangle \rightarrow |-1,0\rangle$ transition. These two additional transitions introduce beating in the oscillations. This effect can be reduced by polarising the nuclear spin state into one of the three possible unclear spin values.

The NV is surrounded by a bath of other magnetic impurities. The most abundant ones are nitrogen atoms of electron spin $S = 1$ and the carbon isotope ^{13}C, which has $I = 1/2$ (the relative abundance of ^{13}C is 1.1%). The dipolar coupling between these fluctuating spins and the NV leads to inhomogeneous dephasing of the coherence. In other words, the stochastic magnetic field created by the spins induces a jitter of the NV resonance over time. Over multiple measurement runs this leads to a decay of the averaged Ramsey oscillations. The decay is characterised by the time constant T_2^*, which is is referred to as inhomogeneous dephasing time. T_2^* is of the order of tens of μs in diamond grown using chemical vapour deposition, which can be engineered to contain less than 0.1 ppm of nitrogen impurities and to

be isotopically pure ($[^{13}C] < 0.3\%$) [104]. The T_2^* is drastically reduced when the NV centre is found within nanodiamonds and is of the order of 10 μs [105].

While having an influence on the linewidth of the ODMR resonances (Sec. 2.3), the T_2^* also limits the amount of pulses which can be applied to coherently rotate the NV centre on the Bloch sphere.

2.4.4 Sensing of time-dependent magnetic fields

The NV centre can be also used to sense time-dependent magnetic fields. The most simple pulse sequence used to achieve this is called Hartmann-Hahn (or spin echo) spectroscopy [106]. The sequence is made of a π-pulse placed between the two $\pi/2$-pulses of the Ramsey sequence (Fig. 2.10(b)). The effect of the π-pulse is to mirror the Bloch vector with respect to the plane orthogonal to equatorial plane and passing through the axis defined by the excitation field. If the time interval between the π-pulse and each $\pi/2$-pulse is identical, the total phase accumulated in the presence of a magnetic field $B(t)$ is:

$$\phi = \gamma \left(\int_0^{\frac{\tau}{2}} B(t)\mathrm{d}t - \int_{\frac{\tau}{2}}^{\tau} B(t)\mathrm{d}t \right) \tag{2.22}$$

The equation shows that any dephasing induced by DC or slowly fluctuating fields is cancelled and the Bloch vector gets rotated back into its initial state at the end of the sequence. The same is true for fast magnetic field fluctuations, since in this case each of the two integrals evaluate to zero. The spin echo sequence is mostly sensitive to magnetic fields with frequency $\nu \sim 1/\tau$. It creates a bandpass filter for AC magnetic fields, dynamically decoupling the NV from noise outside the filter window. The protection from noise leads to a coherence time longer than T_2^*.

More complex sequences can be used to further extend the effective coherence time of the NV centre by reducing the detrimental impact of pulse errors, such as the the Carr-Purcell-Meiboom-Gill sequence or the XY-4, XY-8 sequences. While protecting the NV from decoherence, these sequences can also be used to perform sensing of AC magnetic fields. The narrow spectral windows they create allows for much higher sensitivities compared to ODMR or Ramsey sensing schemes, of the order of $1\,\mathrm{nT}/\sqrt{\mathrm{Hz}}$. They have been successfully used to probe ensembles of nuclear spin species surrounding the NV centre [57], image the field creating by a single electron spin [53] and is at the core of the techniques used to entangle the NV electron spin to proximal nuclear spins [33].

2.5 Sensitivity to DC magnetic fields

In the case of an ODMR measurement, a change in the magnetic field induces a change in the PL signal of the NV, caused by a frequency shift of the ODMR line. The PL intensity as a function of the frequency ν is described by an envelope centred on the resonance frequency [102]:

$$I(\nu, B) = I_0 \left[1 - \mathcal{C}\mathcal{F}\left(\frac{\nu - \nu_0(B)}{\Delta\nu}\right)\right] , \tag{2.23}$$

where I_0 is the PL rate in the absence of MW excitation, $\mathcal{C}$ is the contrast and $\mathcal{F}$ is a function which describes the resonance dip, $\nu_0(B)$ is the resonance frequency of one of the two ground state transitions at a given magnetic field B and $\Delta\nu$ is the dip linewidth. At a fixed field, the photon counts $\mathcal{S}(B)$ for an integration time interval Δt are given by $\mathcal{S}(B) = I(\nu, B)\Delta t$. The standard deviation, assuming that the photon statistics are shot-noise limited, is given by $\sigma_\mathcal{S} = \sqrt{I(\nu, B)\Delta t}$. A magnetic field fluctuation induces a change in the PL counts given by:

$$\delta\mathcal{S}(B) = \frac{\partial I(\nu, B)}{\partial B}\delta B\, \Delta t \, . \tag{2.24}$$

The signal-to-noise ratio then is:

$$\begin{aligned} SNR = \frac{\delta\mathcal{S}(B)}{\sigma_\mathcal{S}} = \\ = \frac{\dfrac{\partial I(\nu, B)}{\partial B}}{\sqrt{I(\nu, B)}}\delta B\sqrt{\Delta t} \, . \end{aligned} \tag{2.25}$$

The sensitivity to DC magnetic fields is defined as the minimum detectable signal for a signal-to-noise ratio of one with for integration time Δt [93]:

$$\begin{aligned} \eta_{DC} = \delta B\sqrt{\Delta t} = \frac{\sqrt{I(\nu, B)}}{\max\left|\dfrac{\partial I(\nu, B)}{\partial B}\right|} = \\ = \frac{\sqrt{I(\nu, B)}}{\max\left|\dfrac{\partial \mathcal{F}}{\partial \nu_0}\right|}\frac{\Delta\nu}{\mathcal{C}I_0}\frac{\mathrm{d}\nu_0(B)}{\mathrm{d}B} \, . \end{aligned} \tag{2.26}$$

This expression can be further simplified assuming that the ODMR contrast is small and that the magnetic field is such that the weak-field approximation is valid:

$$\eta_{DC} = \alpha \frac{h}{g\mu_B} \frac{\Delta\nu}{\mathcal{C}\sqrt{I_0}} \,, \tag{2.27}$$

where $\alpha = 1/\max|\partial\mathcal{F}/\partial\nu_0|$. If the dip has a Lorentzian lineshape $\alpha = 4/(3\sqrt{3})$, while in the case of a Gaussian distribution $\alpha = \sqrt{e}/2$.

Equation 2.27 indicates the crucial parameters to improve the sensitivity of magnetic field sensing with ODMR: linewidth, contrast and PL rate. For this reason, NV centres with long T_2^* are more desirable. Since the linewidth is also dependent on optical and microwave power, it is important to achieve optimal excitation of the NV centre, allowing high ODMR contrasts and PL rate while using weak driving fields.

Ramsey interferometry can also be used to detect DC magnetic fields, as explained in Section 2.4.3. The signal of the Ramsey sequence, with the addition of decoherence, evolves as:

$$S_R(t) = I_0 \left[1 - \frac{\mathcal{C}_R}{2}\left(1 + \cos\left(\frac{g\mu_B}{\hbar}t\right)\right)\right] \,, \tag{2.28}$$

where I_0 is the photon rate, $0 < \mathcal{C}_R, \leq 1$ is the Ramsey fringe visibility and $\chi(t)$ is a function describing the loss of coherence of the quantum system. This implies that also in this case the decoherence sets a limit the minimum detectable field, although arbitrarily small signals could be in principle acquired by increasing the free evolution time t. Assuming $\chi(t) = e^{-\frac{t}{T_2^*}}$, the, sensitivity for a Ramsey sequence is [93]:

$$\eta_{DC,R}(t) = \frac{\hbar}{g\mu_B} \frac{e^{-\frac{t}{T_2^*}}}{\sqrt{2t}\,\mathcal{C}_R\sqrt{I_0 t_r}} \,, \tag{2.29}$$

where t_R is the length of the final readout pulse (Sec. 2.4.3). Equation 2.29 indicates that there is an optimal readout time, given by the competition between a free evolution time t as long as possible and the signal loss, which decays with a rate given by $1/T_2^*$. The optimal readout time in this case is given by $t = T_2^*/2$ [93], so that the optimal sensitivity becomes:

$$\eta_{DC,R} = \sqrt{e}\,\frac{h}{g\mu_B}\,\frac{1}{\mathcal{C}_R\sqrt{I_0 t_r}}\,\frac{1}{\sqrt{T_2^*}} \,. \tag{2.30}$$

This gives a larger sensitivity compared to Equation 2.27, making Ramsey interferometry desirable when weak magnetic fields are to be detected. However, it is worth noting that the same sensitivity can be achieved with pulsed ODMR, when the π is optimised to be T_2^*-long [102].

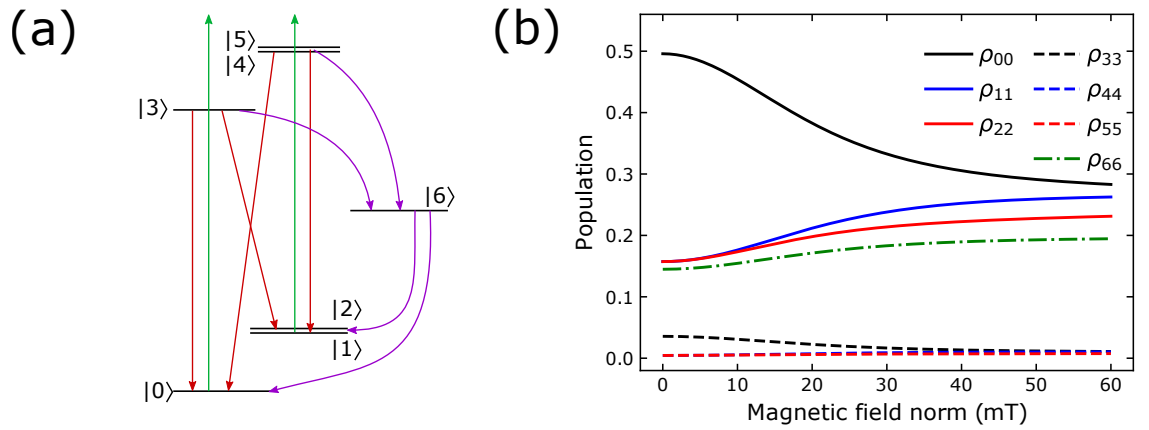

Figure 2.11: Magnetic-field dependent photodynamics. (a) Seven-level system used to capture the NV photodynamics, for an arbitrary magnetic field. In general, off-axis magnetic fields couple the zero-field eigenstates and allow for spin-flip transitions which modify the zero-field photodynamics. (b) Steady-state populations of the seven-level model as a function of the magnetic field magnitude, with an optical excitation rate $\gamma_L = 0.1\,\gamma_r$. The angle between NV axis and magnetic field vector is $\vartheta = 45°$. An increasing magnetic field magnitude changes the equilibrium populations balance, populating the shelving state $|6\rangle$ to an ever greater degree.

2.6 Magnetic field-dependent photodynamics

As discussed above, the energy level structure depends on the magnitude and orientation of static magnetic fields with respect to the NV axis. Off-axis magnetic fields introduce a coupling between the $|0\rangle$ and $|\pm1\rangle$ levels both in the optical ground and excited states. It follows that also the optical decay rates of the unperturbed NV centre are modified in the presence of an external magnetic field. This particularly impacts the application of NV centres in scanning NV magnetometry, where the stray fields generated by magnetic thin films can be very strong and with different orientations depending on the location within the sample. Here I describe some of the main aspects of the photodynamics of the NV centre in the presence of arbitrary external fields.

In order to fully grasp the photodynamics of the NV centre, I make use of a seven-level system model which includes the ground-state and excited-state fine structure of the NV centre (Fig. 2.11(a)). To simplify the treatment, I assume that the strain splitting is weak, thus $E \approx 0$. At zero-field, the levels $|i\rangle$ with $i = 0, 1, 2$ are split by $D_{gs} = 2.87\,\text{GHz}$ in the optical ground state while the levels of the excited state $|i\rangle$, $i = 3, 4, 5$, are split by the excited state zero-field splitting $D_{es} = 1.42\,\text{GHz}$. The transition rates from level $|i\rangle$ to the level $|j\rangle$ are denoted as γ_{ij}. Since the allowed decay paths from the excited state levels are known (Sec. 2.1), I can make make some assumptions on the decay rates. I assume that the optical decay rates from the excited states to the same spin quantum number in the ground state to

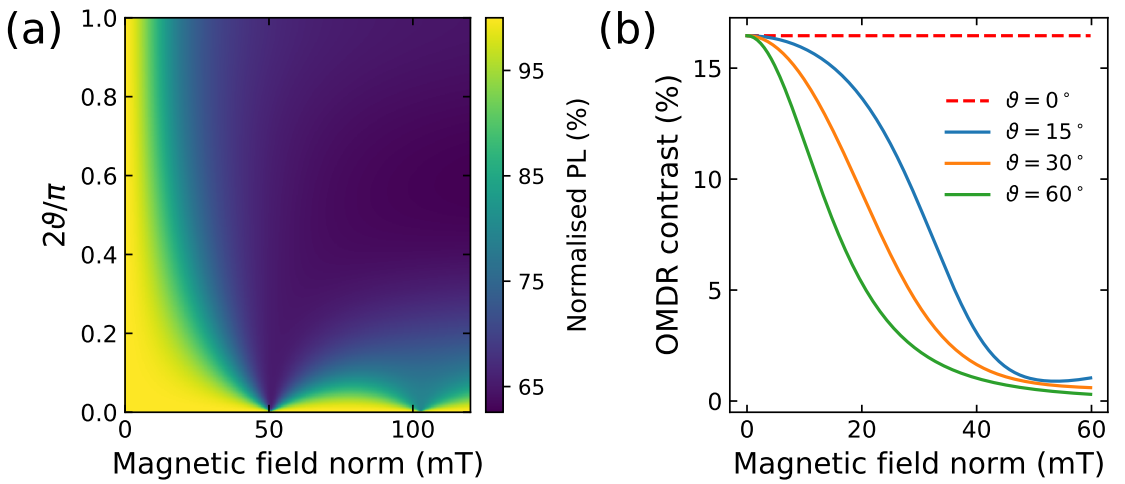

Figure 2.12: Magnetic-field dependent quenching. (a) PL intensity as a function fo the magnetic field magnitude and angle θ between NV axis and magnetic field, with a laser excitation rate $\gamma_L = 0.1\gamma_r$. At weak fields ($\lesssim 5\,\mathrm{mT}$) the PL is unchanged and independent on ϑ. The NV is more sensitive to the magnetic field misalignment when the magnetic field magnitude is large. For example, at 30 mT a $\theta = 10°$ causes a PL 10% drop. (b) ODMR contrast as a function of magnetic field magnitude for three different NV-magnetic field angles. The rates used here are $\gamma_L = 0.1\gamma_r$ and microwave driving rate (Rabi) $\gamma_{01} = \gamma_{02} = \gamma_{10} = \gamma_{20} = 1\,\mathrm{MHz}$. The changes in the branching ratios of the decays and excitations induced by an off-axis magnetic field lead to a decrease of the ODMR contrast for increasing angles and magnetic field magnitudes.

be identical, thus $\gamma_{30} = \gamma_{41} = \gamma_{52} = \gamma_r$. I also assume that the two $m_s = \pm 1$ levels in the excited state couple with the same strength to the intersystem crossing, with $\gamma_{46} = \gamma_{56}$. Conversely, the intersystem crossing has identical decay rates to $|1\rangle$ and $|2\rangle$ levels and thus $\gamma_{61} = \gamma_{62}$. The spin non-conserving transitions from the excited state are assumed to be forbidden. Optical excitation pumps the ground state populations to the excited state but stimulated emission is neglected, the laser being off-resonant and the vibrational relaxation decay time being short.

Using these assumptions, I develop a model to calculate the photodynamics of the NV within the Markov approximation, i.e. the bath into which the coherence is lost is memoryless. The evolution of the density operator for the seven-level system is given by:

$$\frac{\mathrm{d}\rho(t)}{\mathrm{d}t} = -\frac{i}{\hbar}\left[\mathscr{H}, \rho\right] - \frac{1}{2}\sum_{k=0}^{m}\left(L_k^\dagger L_k \rho + \rho L_k^\dagger L_k\right) + \sum_{k=0}^{m} L_k \rho L_k^\dagger \tag{2.31}$$

where $\mathscr{H}$ is the magnetic-field dependent Hamiltonian describing the seven-level system, ρ is the density operator and L_k are the Kraus operators which describe the m photon emission or absorption processes. I neglect T_2^* dephasing, thus working in the approximation of the MW excitation rate weaker the the laser pumping. The laser pump is described as an incoherent absorption process. The Kraus operators

then can either take the form:

$$L_k^{abs} = \sqrt{\gamma_{ji}}\ |i\rangle\langle j|\ ,\ i = (3,4,5)\ , j = (0,1,2) \tag{2.32}$$

or

$$L_k^{em} = \sqrt{\gamma_{ij}}\ |j\rangle\langle i|\ ,\ i = (3,4,5,6)\ ,\ j = (0,1,2)\ . \tag{2.33}$$

Extra Kraus operators can be added if incoherent microwave driving is included in the model:

$$L_k^{mw} = \sqrt{\gamma_{ij}^{mw}}\ |i\rangle\langle j|\ ,\ i,j = (0,1,2)\ , i \neq j\ . \tag{2.34}$$

The steady-state populations can be obtained by imposing that the left side of equation 2.31 is zero and by extracting the diagonal elements ρ_{ii} of the density operator. The steady-state PL rate is then proportional to the sum of the populations in the excited state:

$$\Gamma_{PL} \propto \sum_{i=3}^{5} \rho_{ii}\ . \tag{2.35}$$

In general, when a magnetic field with arbitrary direction is applied to NV, the Hamiltonian eigenstates are not the zero-field eigenstates but a linear combination of them. This affects the steady-state populations and leads to changes in Γ_{PL}.

The photodynamics of the NV center can be simulated using the above treatment. The following simulations use the NV decay rates measured in references [91, 107] (Tab. 2.1). I first investigate the steady-state populations of the NV for an arbitrary magnetic field magnitude and angle (Figure 2.11(b)). At zero field, most of the population is found in the lowest-energy state (i.e. $|0\rangle$) and in the shelving state. However, the presence of a magnetic field not aligned with the NV axis couples the $|0\rangle$ level to the $|\pm1\rangle$ levels. This modifies the zero-field branching ratios which change the PL. As the magnetic field magnitude increases the population trapped in the shelving state increases, while the relative population difference between the three ground-state and the three excited-state sublevels decreases.

The change induced by a magnetic field on the steady-state populations is reflected in the NV PL rate (Figure 2.12(a)). At low fields and at small angles, the NV fluorescence rate is maximal. At the level anti-crossings (that is, when $|B| = 2\pi D_{es}/\gamma \approx 51\,\mathrm{mT}$ or $|B| = 2\pi D_{gs}/\gamma \approx 103\,\mathrm{mT}$) and small ϑ, the weak coupling between the $|0\rangle$ and the $|1\rangle$ states induced by the magnetic field off-axis component creates a cycling spin-flip transition which transfers part of the population to the shelving state. This effect creates two dips in the PL centred at the two anti-crossings, as shown in Figure 2.12(a). When the angle between magnetic

	Decay rate (MHz)
γ_r	32.2
γ_{36}	12.6
$\gamma_{46} = \gamma_{56}$	80.7
γ_{60}	3.1
$\gamma_{61} = \gamma_{62}$	2.5

Table 2.1: Decay rates used in the 7-level system model for the NV magnetic field-dependent photodynamics. The rates are measured in [91, 107].

field and NV axis increases –that is when the coupling between the levels becomes larger– the two dips broaden and for large angles the PL drops monotonically as a function of magnetic field magnitude. This is indicated in the dark region of the Figure 2.12(a), that corresponds to non-zero angle and magnetic field. Adding microwave driving to the model allows us to calculate the ODMR contrast, as:

$$\mathcal{C} = \frac{\Gamma_{PL}(B, \vartheta, \mathrm{MW} = \mathrm{OFF}) - \Gamma_{PL}(B, \vartheta, \mathrm{MW} = \mathrm{ON})}{\Gamma_{PL}(B, \vartheta, \mathrm{MW} = \mathrm{OFF})} \,. \tag{2.36}$$

Figure 2.12(b) shows the magnetic field-dependent ODMR contrast for few angles. I see that ODMR contrast drops in a way similar to the PL rate. However, while the PL is still observable even for large fields and large angles ϑ, the ODMR contrast drops sharply and is close to zero for $|B| > 40\,\mathrm{mT}$. This limits the applicability of NV centres for magnetic field sensing. If the magnetic fields produced by the sample at the NV site are too strong and not aligned with the NV axis, the ODMR signal is practically impossible to observe and thus quantitative magnetic field measurements are hard to extrapolate.

2.7 Experimental setup

A confocal microscope is used in order to address single NV centres. The confocal microscope configuration allows for nearly diffraction-limited resolution [87] and reduces the optically excited area, thus reducing the background photons and enhancing the signal-to-noise ratio. The setup is depicted in Figure 2.13. A diode pumped solid-state laser (Ventus 532, Laser Quantum) with a wavelength of 532 nm and horizontal polarisation is passed through a polarising beam-splitter (PBS). The transmitted beam intensity is controlled by an acousto-optical modulator (MT80-A1.5-VIS, AAOptoelectronics, with RF driver at 80 MHz) in "double-pass" configuration, which is used to improve extinction ratio and the rise time. The first order

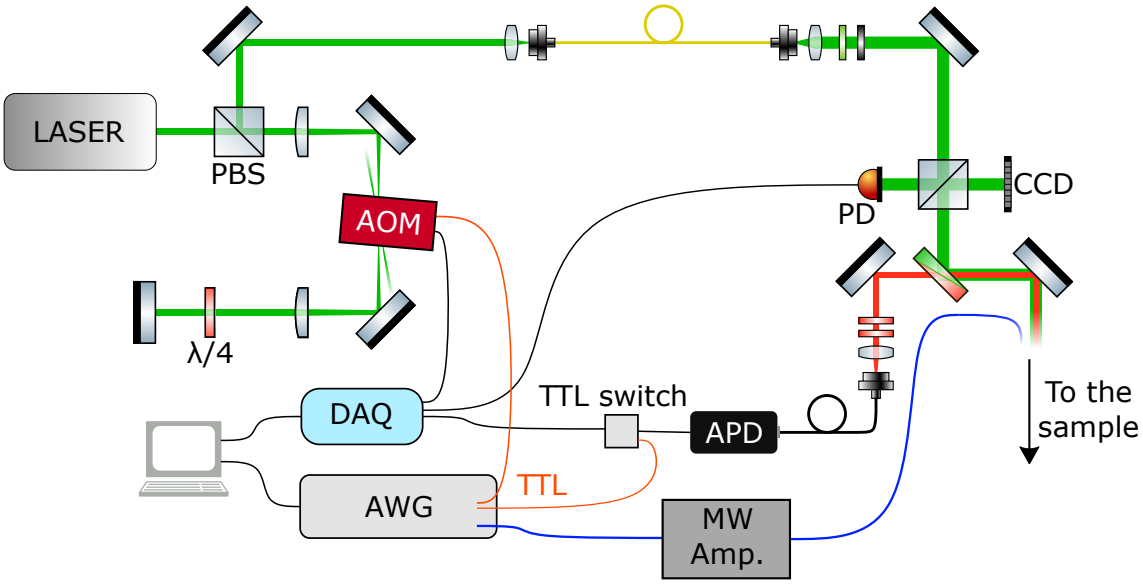

Figure 2.13: Schematic of the setup, as described in the text. Thin orange lines indicate TTL signals, blue lines carry microwave signals and thin black lines are digital/analog input/output voltages.

of the diffraction pattern is reflected by the PBS and coupled into a single-mode optical fibre (460HP, Thorlabs).

The other end of the fibre is connected to the confocal microscope. An out-coupling lens, with focal length chosen depending on the objective back-aperture, collimates the output of the fibre. The beam is filtered by a bandpass filter (FL532-3, Thorlabs) with a full-width half-maximum (FWHM) of 3 nm and a linear polariser (LPVISE100-A, Thorlabs). Part of the beam is picked by a beam sampler and measured by a photodiode (PDA36A2, Thorlabs) for optical power monitoring. The excitation beam is reflected off a dichroic mirror (LM01-552, Semrock) with the edge at a wavelength of 552 nm and to the confocal objective. The NV emission retraces the excitation path and is transmitted through the dichroic mirror, while the backscattered green excitation is reflected and monitored by a CCD camera, used to image the confocal excitation spot. The NV fluorescence is additionally filtered by two long-pass filters (FEL 600, Thorlabs) and coupled into a single-mode optical fibre (SM600, Thorlabs). The raster scanning can be achieved by either a piezo-actuated mirror (S334, Physik Instrumente) or by scanning xy stages depending on the setup. The photons coupled into the collection fibre are detected by either a spectrometer (Acton SP2570, Princeton Instruments) or an avalanche photodetector (APD, SPCM-AQRH, Excelitas Technologies).

An arbitrary waveform generator (AWG, AWG70002A, Tektronix) provides the TTL pulses which are used to control the AOM and the TTL switch (ZASWA-

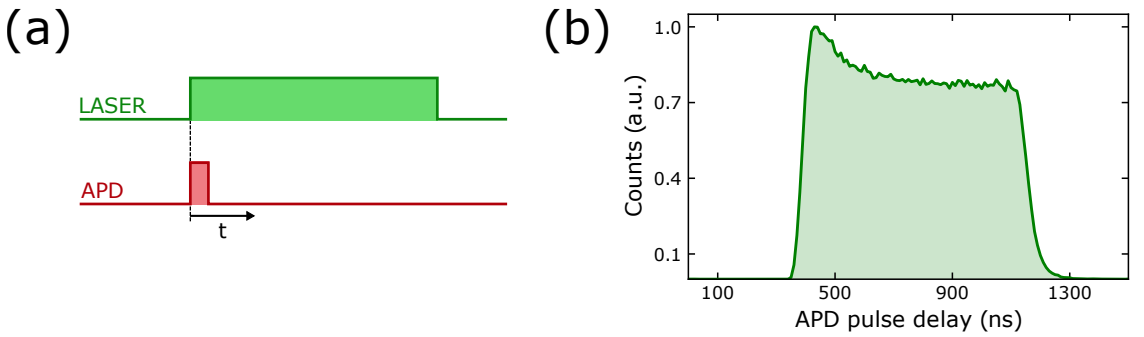

Figure 2.14: Calibration of the AOM delay. (a) Pulse sequence used to measure the AOM delay with respect to the APD pulse. An electrical pulse is sent to the AOM. A short pulse with length $t_{APD} = 50\,\text{ns}$ gates the output of the APD, so that the DAQ card records counts only within that time window. The start time of the APD pulse is scanned across the laser pulse. (b) Counts recorded using the pulse sequence described in (a), plotted against the APD pulse start time, with a laser pulse length $t_L = 1\,\mu\text{s}$. The rise in counts occurring at 350 ns is the total lag due to the electrical pulse plus the acoustic wave build-up in the AOM crystal. The signal peak occurring at the left edge with a subsequent decay is due to the trapping of the $|0\rangle$ population getting trapped in the shelving state with the increasing number of optical cycles.

2-50DR, Minicircuits) which gates the APD output. The AWG sampling rate is 25 GS/s, providing sufficient resolution both for pulses which can be as short as 40 ps and for sinusoidal waveforms at frequencies up to 5 GHz. The microwave output is amplified by a high power/high gain amplifier (ZHL-16W-43+, Minicircuits) which can supply up to 16 W of power and has a gain of 43 dB , since the AWG can supply a maximum power of -2 dBm. The output of the amplifier is connected to an antenna which is used to excite the NV centres.

A data acquisition (DAQ) card (NI-DAQ 6323, National Instruments) provides the analog and digital signals required to control the setup hardware and the counting logic to count the APD pulses. The whole setup is coordinated by a computer running a custom program to perform the experiments.

2.7.1 AOM delay and APD window size optimisation

Because of the timescales of the NV spin decoherence, occurring on the timescale of μs, pulsed measurements require precise pulse timing. The pulse delays as well as the optimal laser and APD pulse window sizes have to be calibrated in order to achieve optimal spin driving.

AOMs diffract light with a travelling acoustic wave, generated by a piezoelectric transducer at one end of the AOM crystal. When the piezoelectric is turned on, the acoustic wave takes a finite amount of time to reach the laser beam travelling through the crystal. The lag is typically of the order of 100 ns. This implies that when the AOM is pulsed there is a sizeable time shift between the pulsed laser sequence and

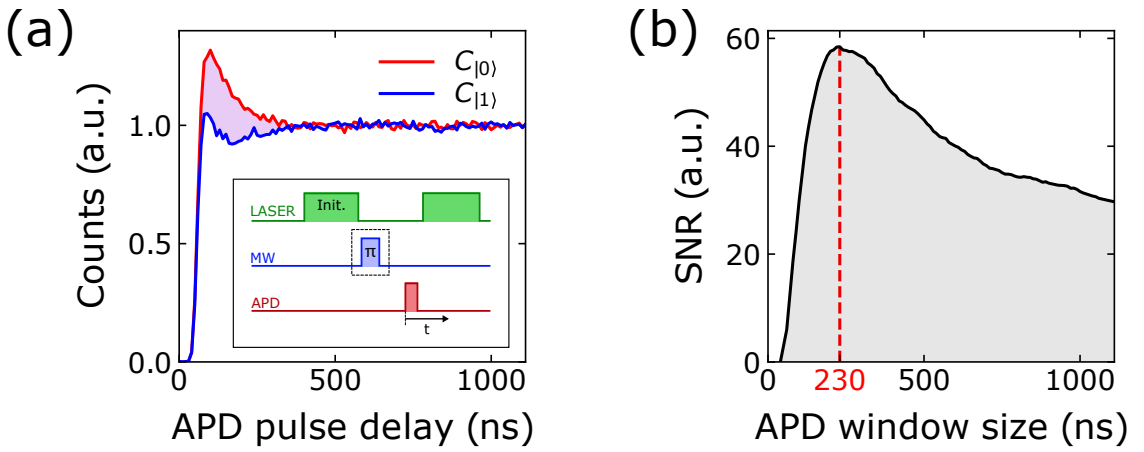

Figure 2.15: Time-dependent NV fluorescence and optimal readout window size. (a) An NV is initially prepared in the $|0\rangle$ state by a long initialisation pulse, as shown in the inset. After a dark time, a second laser pulse is used to readout the fluorescence, while a short APD pulse (50 ns) is scanned across it to detect the time-resolved NV fluorescence (red curve). An optional MW π pulse is used to flip the population into either the $|-1\rangle$ or $|+1\rangle$ state before the readout (blue curve). (b) SNR of the NV readout as a function of APD window size, calculated using the time traces in (a). The SNR peaks at 230 ns, corresponding to the APD window size for optimal spin readout.

the rest of the pulses, such as MW and APD. The delay is characterised using the pulse sequence shown in Figure 2.14(a). After focussing on an NV centre and optimising on its fluorescence, a pulse is sent to turn on the AOM. The APD output is gated in order to acquire counts only during a short time window (e.g. 50 ns) and the APD pulse is scanned across the laser pulse. The sequence is repeated approximately 10^4 times to build up enough statistics. If there was no lag between APD and AOM, the DAQ card would start recording counts as soon as the right edge of the APD pulse has crossed the left edge of the AOM pulse. However, a delay of ≈ 350 ns was observed before the counts are measured (Fig. 2.14(b)). The electric pulses sent to the AOM are shifted accordingly to compensate for this delay.

The APD readout window has an optimal length, linked to the photodynamics of the NV centre. In order to estimate it, the NV centre is initialised with a long laser pulse ($t_{init} > 5\,\mu$s). A second laser pulse occurs after at least 500 ns of dark time, to allow the relaxation of the population trapped into the shelving state to relax back into the $|0\rangle$ ground state. An optional microwave π pulse can be inserted in the sequence to flip the population into either the $|-1\rangle$ or $|+1\rangle$ state after the initialisation pulse. A short APD pulse is scanned across the laser pulse (inset of Fig. 2.15(a)). The measured signal is shown in Figure 2.15(a). When the evolution of the $|0\rangle$ state is recorded (red curve), I observe a peak followed by a decay to steady-state fluorescence rate. The fluorescence decays because part of the population initialised in $|0\rangle$ gets trapped into the shelving state over few optical cycles. The

reference trace (blue curve) drops rapidly to a lower fluorescence rate, due to its fast decay into the shelving state. The fluorescence then recovers to the same steady-state fluorescence as $|0\rangle$, because of the preferential coupling of the shelving state population to the $|0\rangle$ level.

The difference of the $|0\rangle$ and $|\pm1\rangle$ time traces is used to define the optimal APD readout window. The signal-to-noise ratio for a given APD window size t_{APD} –assuming shot-noise limited counts– is defined as:

$$\mathrm{SNR}(t_{\mathrm{APD}}) = \int_0^{t_{\mathrm{APD}}} \frac{C_{|0\rangle}(t) - C_{|\pm1\rangle}(t)}{\sqrt{C_{|0\rangle}(t) + C_{|\pm1\rangle}(t)}}\,\mathrm{d}t \tag{2.37}$$

where $C_{|0\rangle}(t)$ and $C_{|\pm1\rangle}(t)$ are the time traces of the $|0\rangle$ and $|\pm1\rangle$, respectively. The SNR is shown in Figure 2.15(b). The SNR peaks at an APD window size $t_{\mathrm{APD}} = 230\,\mathrm{ns}$.

2.8 NV centres for magnetic field sensing

The NV diamond host can be found in different forms which have been studied extensively in the past years, such as bulk diamond, nanodiamonds or engineered diamond nanostructures. The choice of diamond host is crucial to investigate specific characteristics of the samples under study. In this section I will overview the ones used in the experiments described in the following chapters.

NV centres in nanodiamonds, with an average diameter of 20 nm, have been proven to show coherence times which can be close to the coherence time in bulk materials [59]. The nanodiamonds can be drop-casted on the surface of a magnetic material (Fig. 2.16(a)). Each of the nanodiamonds can be individually addressed with the confocal microscope and probe only a small volume around them. The advantage of using NV centres in nanodiamonds to sense magnetic materials lies in the ease of fabrication and the stability of the nanodiamond location on the sample surface.

Another microscope configuration used in this thesis involves the combination of an inverted confocal microscope with an AFM which detects the cantilever oscillations using the beam-deflection method 2.9. In this case the nanodiamonds, drop-casted on a glass slide, can be picked up by the AFM cantilever (Fig. 2.16(b)). The nanodiamond can be then scanned to create 2D maps of the stray fields across a magnetic sample. The samples producing the stray fields need to be transparent, since the presence of the AFM deflection readout head allows optical excitation and readout of the NV centres only with an inverted microscope configuration (Fig. 2.16).

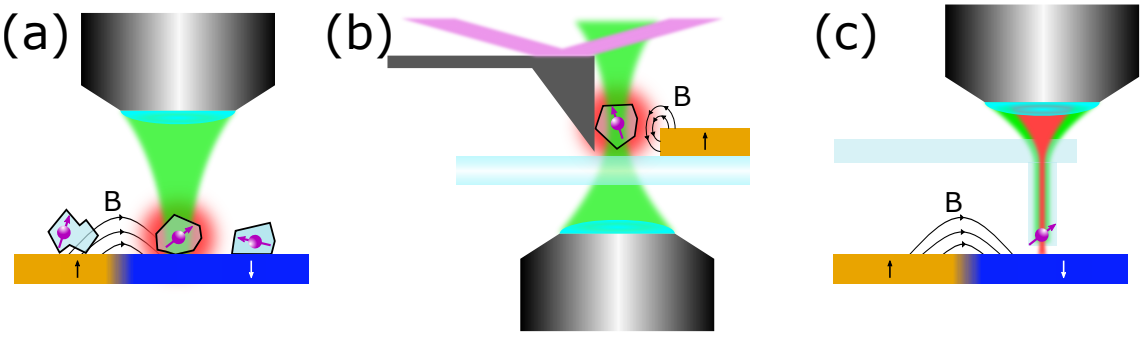

Figure 2.16: Microscope configurations for NV magnetometry, as used in this work. (a) A confocal microscope excites NV centres in nanodiamonds, drop-cast on the surface of a magnetic material. (b) An inverted confocal microscope excites and collect the PL of NV centres grafted to the tip of an atomic force microscope based on the optical deflection method. (c) An atomic force microscope with electrical readout controls a bulk diamond tip, which contains a shallow-implanted NV centre. A confocal excites and reads the PL from the top.

If the sample is not translucent, 2D mapping of the stray fields is still possible with the aid of electrical-readout atomic force microscopes. The electrical readout removes the need for a detection head, as the one used in beam-deflection method, and allows to excite and read the NV from the top (Figure 2.16(c)). In this configuration, NVs in nanodiamonds can be still picked up and used for sensing, as shown in many seminal papers. Nonetheless, the recent commercial availability of bulk diamond probes has made the diamond-picking approach less attractive. The NV centres are implanted within few tens of nanometers from the surface of the scanning tip, guaranteeing a small NV-to-sample distance [108]. Moreover, the emitter quantum efficiency is increased thanks to a weak waveguide effect create by the diamond pillar, resulting in a preferential emission along the optical axis. The T_2^* is typically longer than 1 μs since the NV are implanted in electronic-grade diamond ($[N] < 5$ ppb), resulting in a sensitivity which is better than NVs in nanodiamonds.

2.9 Atomic force microscopes

The invention of the atomic force microscope (AFM) has provided an invaluable tool for nanotechnologies, allowing to probe matter with a resolution which can be a fraction of a nanometer, with advantage of being almost non-invasive. Over the years, the primary function of AFMs – probing the topography of surfaces – has been extended to investigate other properties, such as conductivity, piezoelectricity and magnetism. As mentioned in the previous section, NV centres can be also used as scanning probes for magnetic fields. Here I will briefly describe the main configurations and operation modes of AFMs.

AFM modes AFM microscopes can be operated in a few different modes depending on the application for which they are used. Here I will briefly describe the two main modes which are routinely used in our experiments, namely contact mode and tapping mode. In both operation modes, the AFM controller reads the electrical signal generated by a detector which can record the motion of the AFM cantilever.

In contact mode the AFM tip is scanned across the surface. The presence of features on the surface causes the cantilever to bend, changing the electrical signal produced by the detector. A proportional-integral-derivative (PID) feedback loop stabilises the signal around a user-defined setpoint by controlling the z-coordinate of the cantilever through a piezoelectric actuator. The changes in the z-coordinates are recorded by the AFM controller and converted into the surface topography information. While contact mode is the simplest way of operating an AFM, is sensitive to 1/f noise, it leads to a faster tip/sample degradation and is not reliable in liquid environments.

To overcome these hurdles, AFM cantilevers can be operated in tapping mode. In this case a dither piezo oscillates at the mechanical resonance of the cantilever. Far away from the surface, the cantilever oscillates at a constant amplitude and phase relative to the piezo oscillation, both detected and read by the AFM controller. When the tip approaches the surface, the cantilever amplitude and phase change. In this case the PID loop feedbacks on the amplitude (or the phase) of the cantilever. Tapping mode probes the surface less invasively than contact mode. It is also suitable in liquid environments. The phase tracking produces an additional data channel when scanning, which can be used to highlight regions of the samples with different properties (e.g. soft vs hard regions, grain boundaries, etc.).

AFM configurations The most common way of detecting the motion of the AFM cantilever in commercial AFMs is the beam-deflection method. A light source (usually a laser or a superluminescent diode) impinges the top surface of the AFM cantilever at an angle. The beam is reflected by the cantilever and is detected by a four-quadrant photodiode. When the cantilever is scanned across a surface, the photodiode detects any change in the balance of the signal on the four quadrants and converts it into an electrical signal which is detected by the AFM controller. The beam-deflection method allows for operation in contact and tapping mode, along with derived modes as piezo-force microscopy, conductivity imaging and magnetic force microscopy. Because of the need for cantilever optical detection, this AFM configuration requires a AFM head above the cantilever. The head contains the light source, the four-quadrant detector, the piezoelectric actuator to control the

height of the tip and the electronics to interface with the AFM controller. The AFM head thus prevents optical access from the top and the confocal microscope used to read out the NV centres needs to be in inverted configuration.

The other AFM detection mode used in this work does not rely on optical beams. The AFM tip is glued across a quartz tuning fork, which is mounted on a ceramic plate. Two gold tracks are deposited on the ceramic and they are in contact with the two prongs of the tuning fork, respectively. In the standard configuration, an silicon tip is glue across the tuning fork, creating a system of two coupled harmonic oscillators. The ceramic plate is mounted on a titanium holder with an integrated dither piezoelectric. The dither piezo oscillates at a selectable frequency, which is tuned to the lowest-frequency resonance, which corresponds to the antisymmetric motion of the tuning fork prongs. The oscillation compresses and stretches the tip, creating a tapping motion. A high sensitivity amplifier detects the piezoelectric signal produced by the quartz oscillation, which is used as a signal for the AFM PID loop. Because of the detection modality, AFMs in this configuration can only be operated in tapping mode. While this limits the available imaging modes, it comes with the advantage of not requiring an AFM head over the cantilever. This allows for optical access from the top, enabling the imaging of non-transparent samples.

2.10 NV sensing techniques

As described in the previous sections, the NV centre can be a high-sensitivity probe of the perturbations induced by its surrounding environment. In addition to that, the small volume of the NV wavefunction makes it an almost point-like probe, allowing it to resolve changes in magnetic field within less than 10 nm. These two characteristics together make the NV centre attractive for imaging. Here I discuss some of the techniques used to achieve such imaging, with a focus on scanning NV sensing.

Scanning NV sensing has found most of its applications in magnetic imaging techniques. The NV centre, either in a nanodiamond grafted on an AFM tip or implanted in a diamond tip, is scanned over the surface of a material which generates stray fields at the NV location (Figs. 2.17(a-c)). If the stray magnetic fields are DC, the most basic technique which can be used is called “iso-B” imaging. At each scan pixel, the green laser continuously excites the NV. The MW excitation switches between two fixed frequencies $\nu_{\pm}$.The PL is recorded for each frequency. If the stray field shifts the resonance on one of the two fixed frequencies, a dip in PL is observed. On the contrary, if the frequencies lie on the resonance when the NV is far

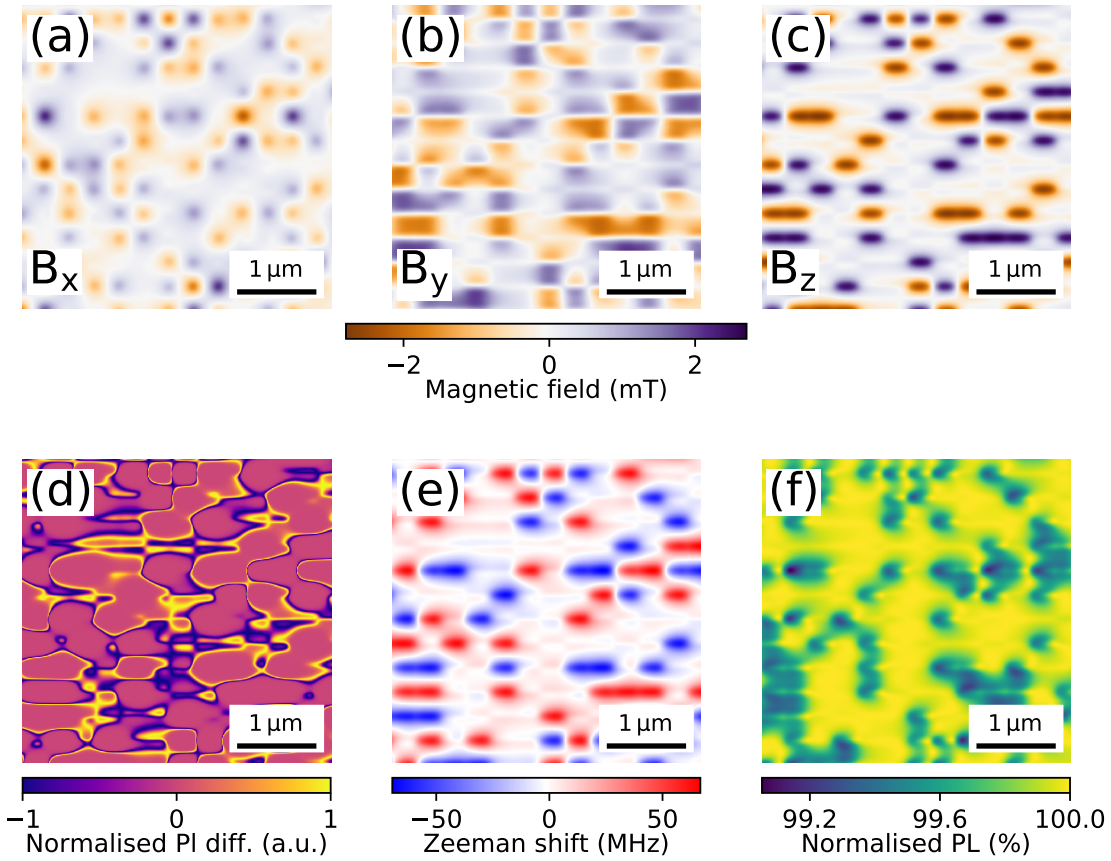

Figure 2.17: Simulation of out-of-plane magnetic bits in a hard drive. Using a grid of square bits with magnetisation randomly pointing either towards the $\hat{z}$ or towards the $-\hat{z}$ direction, the (a) $\hat{x}$- (b) $\hat{y}$- and (c) $\hat{z}$-component of the stray magnetic field at an arbitrary distance from the surface (here 100 nm) can be calculated. Given an NV axis orientation, the energy of the ground state levels can be calculated. (d) Iso-B map with an NV centre with polar coordinates $\vartheta = 35.3°$ and $\phi = 0°$, $E = 2.5$ MHz. A bias field of 3 mT is applied along the NV axis. The two iso-frequencies are $\nu_\pm = 2954 \pm 1$ MHz. (e) Zeeman shift response under the same conditions as (d). (f) PL quenching map of the same area.

from the sample, a shift is converted into an increased PL rate. This is equivalent to taking a contour map of the magnetic field, at the two values $|B_\pm| = 2\pi\sqrt{\nu_\pm^2 - E^2}/\gamma$ (Fig. 2.17(d)). While a single frequency is enough to take a magnetic field contour map, the signal of the two frequencies can be subtracted, thus eliminating any PL fluctuations which occur during the scan. The main advantage of iso-B imaging is the fast scan speed. When the NV PL rate is high (e.g. PL $\gtrsim$ 50 kHz) and ODMR contrast is $\mathcal{C} \gtrsim 10\%$, the measurement time per pixel can be as low as 20 ms. On the other hand, iso-B imaging does not allow to extract the magnetic field vectorial map. It requires to know the extent of the maximum Zeeman shift in the scan area to select the correct frequencies, resulting otherwise in a map which can be difficult to interpret.

The most complete DC imaging mode involves the acquisition of the ODMR

spectra at each pixel (Fig. 2.17(e)). This method is called "full ESR scan" or "ODMR scan". The acquisition time per pixel compared to iso-B imaging is longer, since few data points are required to map the two ODMR dips. On the other hand, knowing the position of the two ground state spin resonances allows to obtain a vectorial image of the magnetic field, projected onto the components parallel and orthogonal to the NV centre axis(Sec. 2.2). These in turn can be used to create a map of the sample magnetisation.

As any stray field in practice has components pointing in directions different than the NV axis, there is always a non-zero off-axis component. If the latter is large enough it leads to an experimentally observable quenching of the NV PL rate (Sec. 2.6). PL quenching thus can be used to image magnetic fields (Fig. 2.17(f)). In the intermediate range where PL and ODMR contrast are only partially quenched, both ODMR map and quenching map can be recorded. However, in the case of strong PL quenching the ODMR is not observable and quenching imaging becomes the only available imaging method. So far, its only application has remained limited to the qualitative imaging of magnetic patterns.

Scanning NV imaging has not remained restricted to the imaging of DC magnetic fields. Ensembles of NV centres have been used to image temperature gradients created by gold nanoparticles [67], using the temperature dependence of the zero-field splitting, caused by the changing strain fields at the NV location [109]. Using coherent control of the NV spin it also possible to image the fields generated by a wire carrying MW fields [68], probe the spatial-dependent conductivity of metals [69] and image a single electron spin [53].

When the probed features are larger than the diffraction limit, wide field imaging with NV centres is also possible. In this mode, a diamond chip with high concentration of NV centres is brought into close contact with the sample under study. A laser beam excites the whole diamond (typically side-coupling the beam by total internal reflection), a MW field excites the NVs and the fluorescence is collected by a CCD camera. An algorithm detects the four pairs of dips (due to the four NV crystal orientations) and reconstructs the distribution of the resonance shifts across the area. This technique has been used to study living cells [42], magnetic inclusions in geological samples [110], to characterise MW antennas [111] or to measure the vector magnetic field generated by electrical currents [112].

2.11 Summary

In this chapter I have summarised the main theoretical aspects of NV physics. The sensitivity of the energy levels to the magnetic field vector allows to use the NV as a sensitive spin sensor. The NV can be used to detect both static magnetic fields, by measuring the Zeemand splitting of the ODMR, or time-dependent magnetic fields, using the coherent control of the NV spin. When attached to the tip of a scanning probe, the NV can be used to achieve 2D imaging of the stray magnetic fields arising from a magnetic sample. We have also presented the three main modes for scanning NV imaging of DC fields: iso-B imaging, which effectively takes contour maps of the field; ESR imaging, which measures the full ODMR spectrum; quenching imaging, which relies on the magnetic field-dependent photodynamics of the NV.

Chapter 3

Magnetic field sensing of a thin-film perovskite

In this chapter I will discuss the sensing of magnetism arising from a thin film of $Pr_{0.8}Ca_{0.2}MnO_3$ (PCMO) deposited on $SrTiO_3$ (STO) using NV centres in nanodiamonds. In this first part, I will give an introduction on some of the properties of manganites and their potential technological applications.

Part of the data presented in this chapter were acquired by David Dominik Jarausch, Lina Klintberg and Nicolas Gauriot.

3.1 Properties of manganites

Manganites are a class of materials which follow the formula $RE_{1-x}AE_xMnO_3$, where RE is a trivalent rare earth and AE stands for divalent alkaline earth elements. The atoms are arranged in a perovskite structure as the one shown in Figure 3.1(a). The unit cell consists of a Mn ion in the middle of the cube. The corners of the cube are occupied by the RE or the AE, while the centres of the cube faces are occupied by oxygen atoms. The Mn atom can be in two different valence states, Mn^{3+} and Mn^{4+}. Usually manganites deviate from a perfect close-packed cubic structure and have lower symmetry. The distortion of the lattice is captured by the tolerance factor $t = (r_{AE/RE}+r_O)/\sqrt{2}(r_{Mn}+r_O)$, where r_i (i = Mn, O, AE/RE) are the average ionic radii [113]. A value of $t = 1$ corresponds to the ideal perovskite structure.

3.1.1 Electronic structure of manganites

Many of the ordered phases in manganites are determined by the interactions between the Mn outermost shell electrons. The five-fold degeneracy of the 3d energy

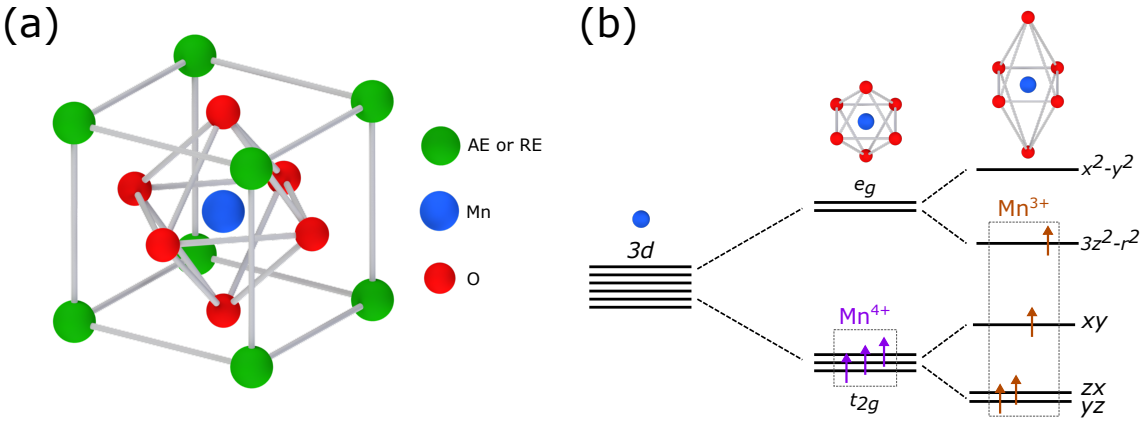

Figure 3.1: (a)Schematic structure of a manganite. A manganese ion lies at the centre of the cubic cell and is surrounded by six oxygen atoms. Rare earth or alkaline earth elements occupy the cube corners. (b) The five-fold degenerate 3d level of a manganese ion is split into a three-fold degenerate level (t_{2g}) and a two-fold degenerate level e_{2g}. Further distortion of the lattice removes the degeneracy of e_{2g} and splits t_{2g} into two more sublevels. This configuration is also the lowest energy configuration for Mn^{4+}, with three electrons filling each of the levels of the ground state. Mn^{3+} induces a distortion of the lattice to reduce the overall energy (Jahn-Teller effect). Adapted from [114].

level of an isolated Mn atom is lifted when the Mn ion is inside a crystal. The levels are split into three degenerate t_{2g} orbitals and into two degenerate e_g orbitals, split by 1.5 eV (826 nm)(Fig. 3.1(b)). The interaction energy between the electrons favours parallel alignment of the spins both for Mn^{3+} and Mn^{4+}, resulting in states with total spin quantum number $S = 3/2$ and $S = 2$ respectively. The levels are further split if the symmetry of the MnO_6 octahedron is lowered, i.e. if the octahedron is elongated. In this configuration, the energy of Mn^{4+} remains unchanged [114]. However, Mn^{3+} is energetically favoured by the lowered symmetry(Fig. 3.1(b)), an effect known as Jahn-Teller distortion. The presence of Mn^{3+} ions thus tends to distort the crystalline cubic symmetry. In this case, the interdependency of the structural deformations can create a correlation between the Mn charge states, leading to charge ordering [115].

The doping x influences the relative concentration of Mn^{3+} and Mn^{4+}. When $x = 1$, the manganese ions are in the Mn^{4+} charge state. Replacing some the RE elements with AE, which act as electron donors, leads to the formation of Mn^{3+} sites. Since Mn^{3+} favours lattice symmetry lowering, manganites with low doping ($x \approx 0$) are strongly distorted by the cooperative Jahn-Teller effect between the Mn^{3+} sites [116].

The magnetic properties of manganites are due to the interactions between Mn ions. Because of the large energy splitting, the electrons in the t_{2g} levels can be considered as always localised. If the doping is $x = 0$, also the e_g electrons are

strongly localised by Coulomb interaction and lead to the formation of a Mott insulator. When $x > 1$, however, holes are introduced in some of the e_g levels, which are then allowed to hop to the Mn^{4+} sites, through the oxygen orbitals. If the orbital configuration is $Mn^{3+}-O-Mn^{3+}$ or $Mn^{4+}-O-Mn^{4+}$, the coupling interaction is a superexchange. The Goodenough-Kanamori rules [117–119] govern this interaction and determine which spin alignment is favoured. The $Mn^{4+}-O-Mn^{4+}$ is an antiferromagnetic interaction while the $Mn^{3+}-O-Mn^{3+}$ can be either antiferromagnetic or ferromagnetic. The $Mn^{3+}-O-Mn^{4+}$ hopping is determined by a double exchange (DE) interaction [120]. The process is energetically favourable if the spin of the electron in e_g is preserved and aligned with the rest of the Mn spins and thus favours ferromagnetic alignment. DE is also the main mechanism of electrical conduction in manganites [121]. The strength of both the superexchange and the DE exchange interactions depend on the overlap integral between the ionic orbitals, which are affected by the bond angles and the crystal parameters. The complex phase diagrams of manganites depend on a large variety of parameters, such as temperature, doping and substrate choice, which stem from the competition between the ferromagnetic and antiferromagnetic interactions, which depend on such parameters. Also the size of the AE and RE cations has an effect on the magnetic interactions. It has been verified that, if the cation size is below an average radius $\langle r \rangle < 1.24\,\text{Å}$, there is an increased distortion of the Mn−O−Mn bonds, which induces the localisation of the e_g electrons and decreases the strength of the double exchange interaction [122, 123].

3.1.2 Thin films, temperature dependence and strain, doping

As I have discussed above, the ordered phases in manganites can change considerably depending on the fabrication parameters. When manganites are grown in the form of monocrystalline thin films, their behaviour is strongly affected by the substrate onto which they are deposited. The most common substrates are $SrTiO_3$ (STO), $LaAlO_3$ (LAO), MgO and $NdGaO_3$ (NGO). The mismatch between the in-plane lattice parameters of the substrate and and of the thin film induces strain, which can be either compressive ($a_{film} > a_{sub}$) or tensile ($a_{film} < a_{sub}$). Depending on the type of strain and on the film thickness, the film can either fully strained [124] or partly relax via crystalline dislocations [125]. The strain changes as a function of the film thickness. The out-of-plane and in-plane lattice parameters monotonically converge to the bulk material lattice parameters for large film thickness [126]. The unit cell deformation affects the overlap integrals of the ionic orbitals meaning that strain

has a direct effect on the magnetic phases of manganites [127]. Experiments [128] have verified that tensile biaxal strain favours the localisation of the e_g electrons because it elongates the Mn−O bonds, thus lowering the Curie temperature T_c. On the contrary, compressive strain increases the double exchange coupling, leading to a ferromagnetic phase with higher T_c.

Strain also affects the strength and the direction of the magnetic anisotropy. The anisotropy in bulk samples is negligible. In thin films, the octahedron distortion induced by the strain causes the anisotropy to be much larger than in bulk. Its direction can be determined by the direction of the octahedron elongation, resulting in an out-of-plane anisotropy for compressive strain and in an in-plane anisotropy for tensile strain [129]. However, this picture is complicated by the temperature dependence of the substrate symmetry. When the temperature is changed, a rotation of the magnetic anisotropy can be observed [130, 131].

3.2 $Pr_{1-x}Ca_xMnO_3$

$Pr_{1-x}Ca_xMnO_3$ has a rich phase diagram, with different ordered phases arising as a function of temperature and doping (Fig. 3.2(a)). At room temperature, PCMO is a paramagnetic insulator. For high doping ($0.3 \leq x \leq 0.5$), PCMO undergoes different phases as the temperature is decreased, becoming a charge-ordered insulator, an antiferromagnetic insulator and finally a canted antiferromagnetic insulator. If the doping is $1.5 \lesssim x < 0.3$, there is a single transition from paramagnetic insulator to ferromagnetic insulator with $100\,\mathrm{K} \lesssim T_c \lesssim 150\,\mathrm{K}$ and for low doping $x < 1.5$ it becomes a spin-canted insulator. When in the form of thin film, the interplay between substrate and thin film can complicate the phase diagram. STO substrates undergo a structural phase transition at 103 K from cubic to tetragonal [132]. It has been observed that epitaxial films undergo a structural transition together with the substrate [125]. When PCMO thin films are deposited on STO, lattice mismatch induces tensile strain which favours an in-plane magnetic anisotropy.

The interest in PCMO/STO arises from its relatively high-T_c ferromagnetic phase combined with its insulating properties. Ferromagnetic insulators (FI) have potential potential applications in superconducting spintronics. A $Pr_{0.8}Ca_{0.2}MnO_3$ / $YBa_2Cu_3MnO_3$ / $Pr_{0.8}Ca_{0.2}MnO_3$ trilayer grown on STO has been used to demonstrate a superconducting spin valve [134]. They also have been proposed to be used superconductor/ferromagnet interfaces in order to create spin-polarised superconducting currents [135]. However, it is expected that the microscopic spin texture plays a role at the S/FI interface [136]. This is particularly crucial for PCMO at low

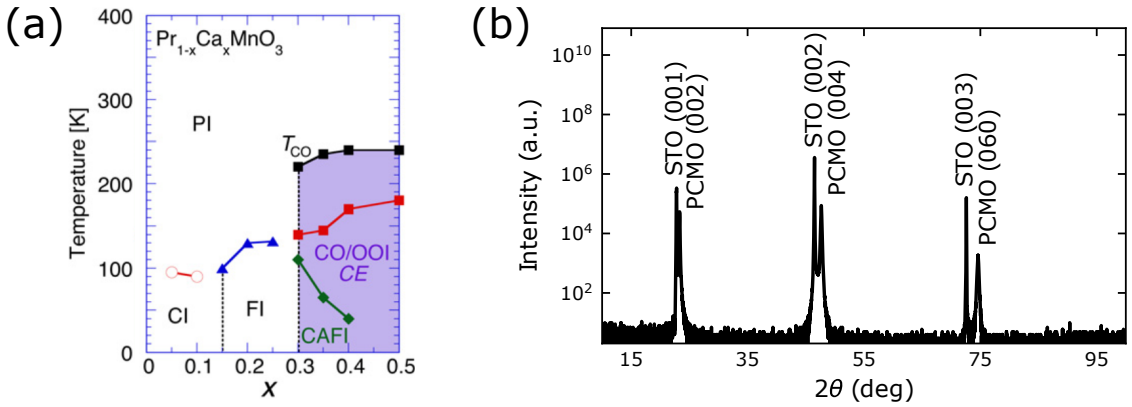

Figure 3.2: (a) Doping-temperature phase diagram for bulk PCMO. When the doping is high ($0.3 \leq x \leq 0.5$) the materials goes from being a paramgnetic insulator (PI) to a charge-orbital ordered insulator (CO/OOI) to a canted antiferromagnetc (CAFI). For intermediated doping $1.5 \leq x < 0.3$, there is a single transition from PI to ferromagnetic insulator (FI) occurring between 100 K and 150 K. Finally, when the doping is $x < 1.5$ the materials becomes a spin-canted insulator (CI) at low temperatures. Adapted from [133]. (b) High-angle X-ray diffraction data for the PCMO thin films studied in this chapter, grown on (001)-oriented STO substrate. The peaks linewidths indicate the single-crystal nature of the films.

doping, which has been reported to show an additional transition occurring after the ferromagnetic transition. This additional transition has been proposed to be caused by the existence of a phase of ferromagnetic clusters within an antiferromagnetic matrix [137].

3.2.1 Fabrication of PCMO/STO thin films

The PCMO film is epitaxially grown on (001)-oriented single crystal STO substrate (Fig. 3.2(b)) by pulsed laser deposition (KrF laser, wavelength $\lambda = 248$ nm at 780 °C in flowing O_2 at 200 mTorr with a beam energy density of 1.5 J/cm^2 and a pulse frequency of 2 Hz. Following growth the PCMO film is annealed at 500 °C in an oxygen pressure of 520 Torr and then cooled to room temperature at a rate of 5 °C/min.

3.3 SQUID measurements

The magnetism of the PCMO thin films was first characterised in terms of its bulk magnetism. We use a commercial superconducting quantum interference device (SQUID) magnetometer (MMPS Quantum Design) to measure the total magnetisation of the thin films. The SQUID magnetometer is made of four single SQUIDs connected in series, through which the sample is moved up and down. The voltage readout is locked in to the motion of the sample in order to remove any background flux through the pick-up coils, yielding greater sensitivity. SQUID are sensitive to

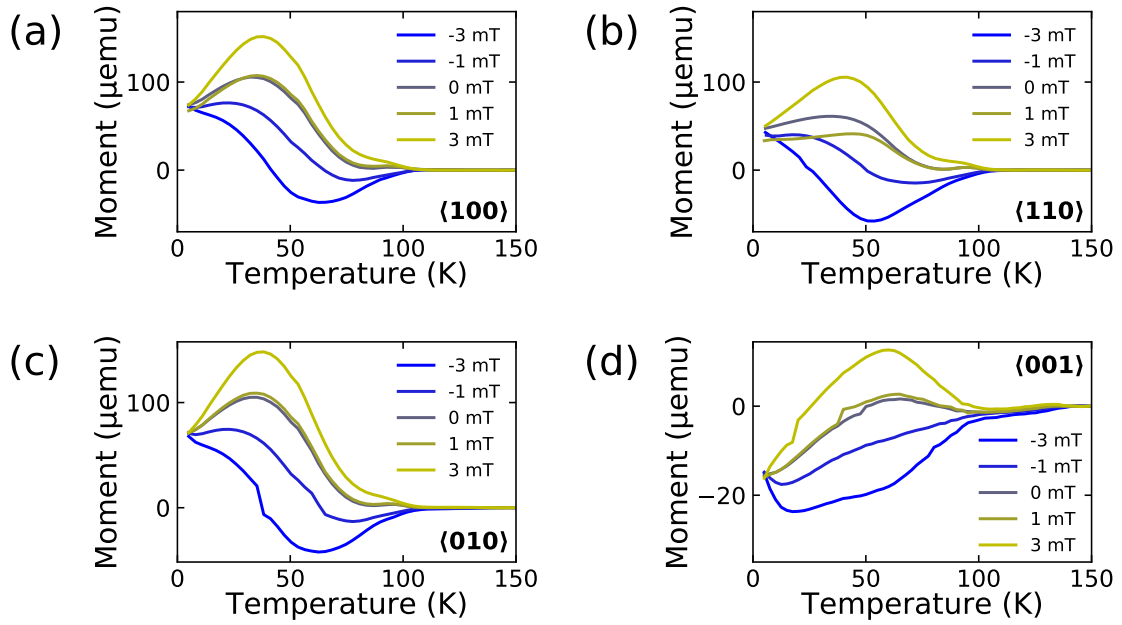

Figure 3.3: Temperature-dependent magnetisation of PCMO/STO, measured with a SQUID magnetometer. The sample is cooled down at zero field. Subsequently, a field of 4 T is applied to polarise the magnetic domains and generate a measurable SQUID. A bias field ranging from −3 mT to 3 mT is applied and the magnetisation is recorded while warming up the system, for the (a) ⟨100⟩, (b) ⟨110⟩, (c) ⟨010⟩ and (d) ⟨001⟩ directions.

the magnetic field projection along the axis orthogonal to the SQUID loop plane. For this reason, measurements of different components of the magnetisation require a physical rotation of the sample.

The measurement protocol tries to reproduce the measurement sequence done with the NV centres. In the first step, the sample is cooled down to the base temperature of the SQUID cryostat (∼ 8 K). The overall signal produced by the thin film magnetic texture cooled down in zero-field averages to a value too small to be detected by the SQUID magnetometer. A field of 4 T is applied in order to polarise the sample magnetisation to produce a detectable field. After this step, the sample is warmed up and the magnetisation is measure, while applying an additional weak bias field. The procedure is repeated using different bias fields and also rotating the samples, in order to measure the magnetisation along the ⟨001⟩, ⟨110⟩, ⟨010⟩ and ⟨100⟩ directions.

Figure 3.3 shows the the results of the experiments carried out for bias fields that range from −3 mT to 3 mT. Figure 3.3(a-c) display the in-plane moment along the ⟨100⟩, the ⟨110⟩ and the ⟨010⟩ direction, respectively, whereas Figure 3.3(d) shows the out-of-plane moment.

The much stronger response of the in-plane components compared to the out-of plane one confirms that the magnetic anisotropy lies mainly in the thin film

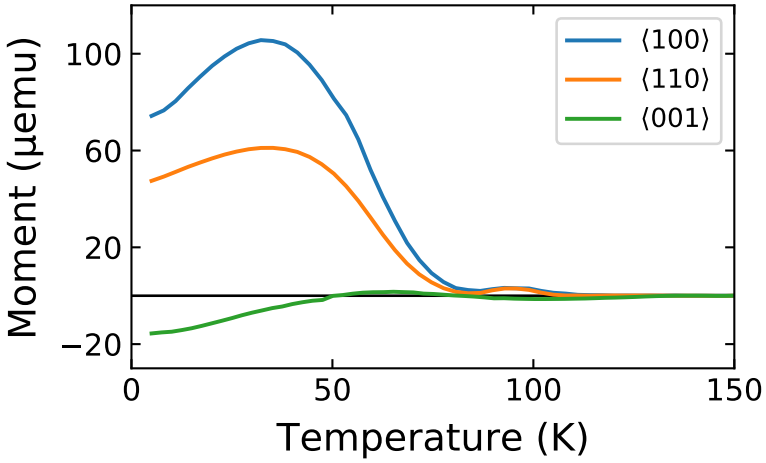

Figure 3.4: Zero-field SQUID measurements of PCMO/STO, taken along the ⟨001⟩, ⟨110⟩ and ⟨100⟩ directions. The ⟨010⟩ direction is not shown since it overlaps the ⟨100⟩ direction. The data show a first transition at $T_c \approx 80\,\mathrm{K}$, where the in-plane components increase. This is followed by a second transition occurring below 50 K, which marks a drop of the in-plane components and an increase of the out-of-plane component.

plane. This is expected, since the tensile strain due to the lattice mismatch between PCMO and STO was observed to induce an in-plane magnetisation below a threshold film thickness. The in-plane components show an onset of magnetism at a Curie temperature $T_c \approx 80\,\mathrm{K}$, which is $\sim 50\,\mathrm{K}$ below the observed Curie temperature for bulk PCMO crystals. The mismatch can be explained by tensile strain, which has an effect also on the onset of magnetic ordering (Sec. 3.1). The sweep of the bias field gives a range of intensity where the overall magnetic response of PCMO is weakly perturbed by an external field. This is of importance for NV sensing, where a weak field is required to increase the sensitivity. Large bias fields (larger than 10 mT) significantly modify the magnetisation trend measured at zero-field (Appendix B)

I now focus on the behaviour of PCMO without any applied bias field (Fig. 3.4). I notice that close to T_c there is a small peak centred around 90 K. Since the maximum moment is close to the noise level of the SQUID magnetometer, this can be attributed to an instrument artifact, which are common when measuring the remanent magnetisation close to T_c. At temperature below T_c I observe an additional transition occurring below 60 K, which is not observed in bulk monocrystalline PCMO samples. Below this temperature the absolute value of the out-of-plane component increases. A concurrent drop in the in-plane components –and in the overall magnetisation– is also visible. A similar behaviour has been observed in samples with different stoichiometry and in bulk polycrystalline samples. The drop has not been entirely understood. The proposed mechanisms for this drop are the competition between a paramagnetic insulator matrix and ferromagnetic domains [138] and

the formation of a spin glass phase [137].

The behaviour observed with a SQUID magnetometer inherently yields the magnetic field produced by the whole thin film. On one hand one can appreciate that PCMO/STO displays a behaviour that deviates from a perfect ferromagnet. On the other hand we are interested in the microscopic response of the thin film. Hence, a magnetometer which is sensitive and at the same time has high spatial resolution is needed in order to capture the nanoscale variations of the stray field, while being performant from room temperature to liquid helium temperature. NV centres can be used for this task.

3.4 Magnetometry of PCMO/STO with NV centres

3.4.1 Setup

The magnetism of PCMO/STO can be probed using NV centres in nanodiamonds. We use nanodiamonds with an average diameter of 20 nm drop-cast on the surface of the thin film 3.5(a). The sample is housed in a closed-loop cryostat (Montana instruments) which can operate from room temperature to its base temperature of $\sim 4\,\mathrm{K}$. The sample is mounted on a three-axis open-loop nanopositioning stage (Attocube ANPxyz101). A thermocouple mounted on the sample holder monitors the temperature at the sample position. The excitation beam is steered by a Physik Instrumente piezo-electric mirror (PI S334), which is used to form the PL raster scans. The rest of the confocal microscope follows the configuration described in Fig. 2.13. The excitation beam is focused by an objective with an aberration-correction ring (Zeiss LD Plan-Neofluar 63x/0.75 Corr M27) through a glass window which separates the vacuum chamber from the atmosphere. The correction ring is used to increase the collection efficiency of the confocal microsope. The microwave excitation can be delivered either by a wire antenna mounted across the sample or on the cryostat window itself.

The nanodiamonds are obtained from ball-milled high-pressure high-temperature diamond ($[\mathrm{N}] < 50\,\mathrm{ppm}$). The high purity of the diamond ensures long NV coherence times, ensuring high magnetic field sensitivity. Most of the NV centres found in these diamonds are single, meaning that only one defect is hosted in the crystal lattice and that the ODMR spectra display a single pair of dips. The small size of the nanodiamonds ensure a small sample-to-probe distance on average. Here I remark that the drop-casting process creates a random distribution of NV centres, thus

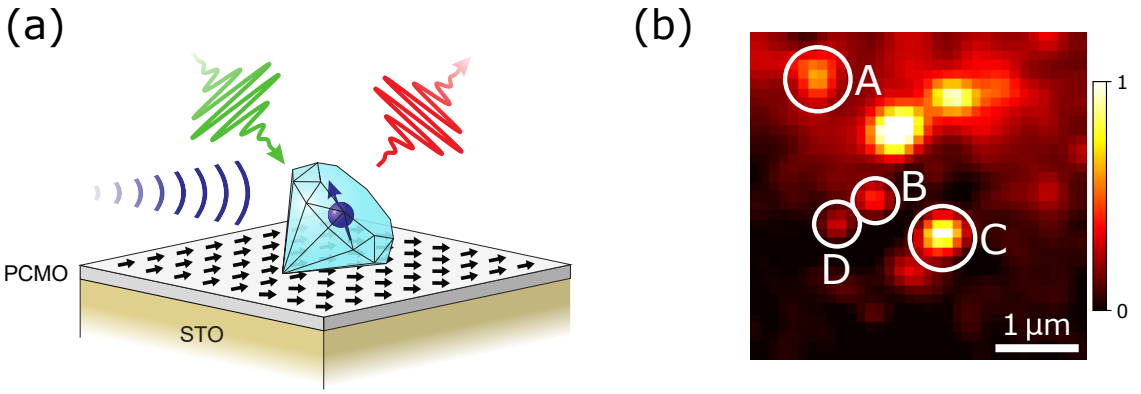

Figure 3.5: NV centres in nanodiamonds for PCMO/STO magnetism sensing. (a) Schematics of the sensor configuration. An NV in a nanodiamond is drop-casted on the surface of PCMO/STO. Laser and microwave excitation can drive the NV centre, which emits photons which are collected by a confocal microscope. (b) PL map of the four NV centres used in the experiment described in 3.4.2.

making the full mapping of the stray field distribution impossible to achieve. In this condition, NV centres are point probes of the stray field at their location. Drop-casting the nanodiamonds also randomizes the orientation of the NV axis, which can point in any direction of the three-dimensional space.

3.4.2 ODMR measurements

In the first experiment, the nanodiamonds were drop-casted on the surface of 150 nm-thick PCMO/STO. We select four emitters, which are shown in the PL map in Figure 3.5(b). Three of them are single NV centres while one of them (site B) contains two NVs. A measurement run follows steps similar to the ones described for the SQUID measurements (Sec. 3.3). The sample is cooled down to around 10 K. A weak bias field, of the order of 1 mT, is applied to split further the resonances, since NVs in nanodiamonds usually display ODMRs spectra with few MHz of strain splitting. After this step, the sample is warmed up and the ODMR spectra of each emitter are acquired at each temperature step. Each ODMR trace is averaged over about 30 measurements, which take around 1 minute each. The high stability of the cryostat ensures that the base temperature is within 0.2 K from the target. We checked the response of the NVs in two subsequent runs.

The data for the first run are presented in Figure 3.6(a-d). First of all, I notice that the NV response is consistent with the SQUID measurements: no magnetism is detected above 90 K. Each NV senses a different field at its location, hinting towards the formation of magnetic domains with feature smaller than the NV separation. However, the splitting as function of temperature for of NV B and NV D are similar,

with a resonance splitting reduction occurring over the same temperature range. I observe that in the PL map, the two emitters are separated by $\sim 1\,\mu$m. On the contrary, the response of NV A and NV C are different from each other, with the changes in splitting occurring over different temperature ranges. The two emitters in this case are spatially separated by more than $1\,\mu$m. The comparison between the ODMR splitting evolution and the spatial location hints towards a domain size of few microns.

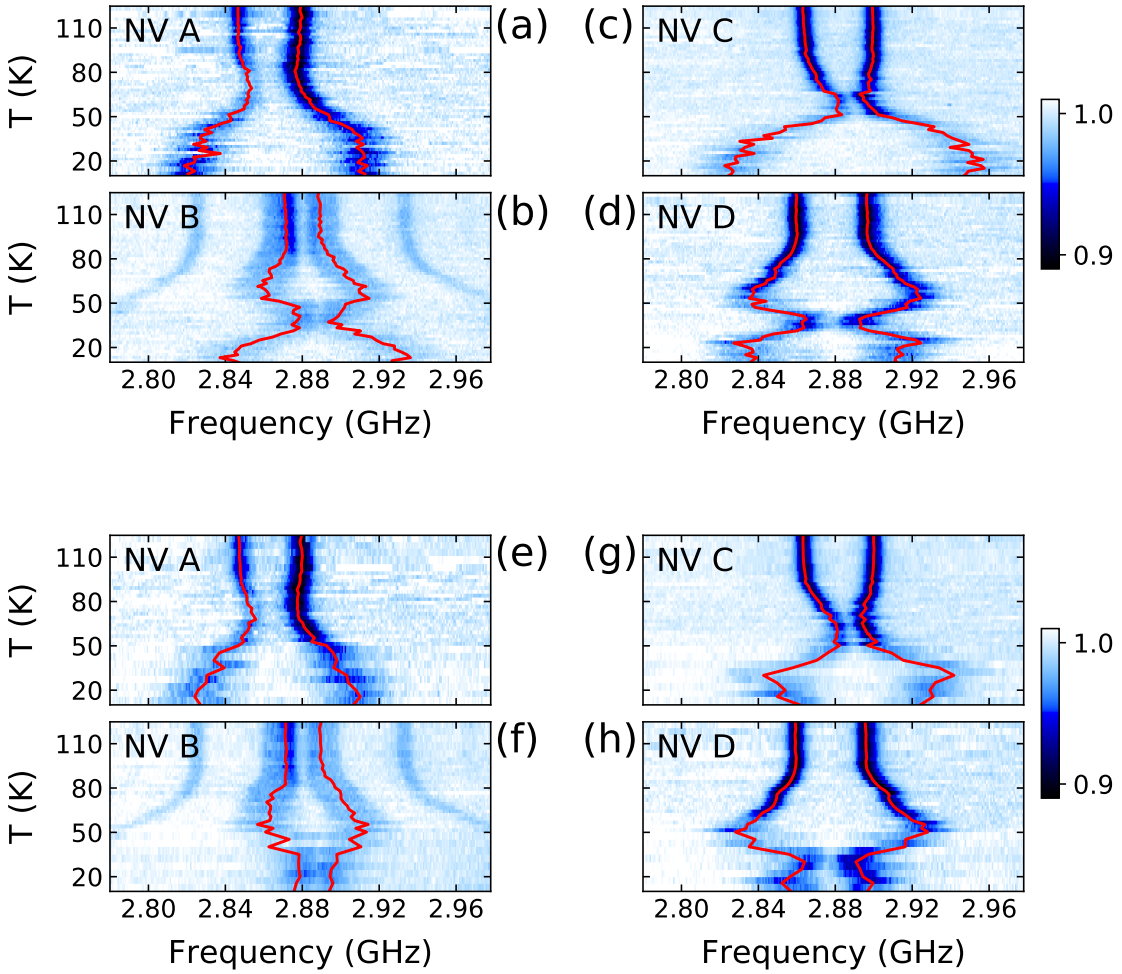

Figure 3.6: ODMR scans of NV centres on PCMO as a function of temperature. The colour bar indicates the normalised fluorescence level.The red lines mark the evolution of the resonance frequencies and have been extracted from fits to single ODMR spectra. The NV centres on the surface of PCMO sense different magnetic fields depending on their spatial location and orientation. (a-d) ODMR evolution of the four NV centres on a cool-down/warm-up cycle. NV A and NV C sense a larger stray field at low temperatures. The reduction in the splitting observed for NV C indicates that the stray field is cancelling the effect of the bias field. NV B and NV D show a similar behaviour to each other, with a pronounced reduction of the ODMR splitting in the range between 20 K to 40 K. This suggests that the magnetic environment is spatially uniform for distances comparable to the NV B-NV D separation $< 1\,\mu$m. The experiment is repeated after warming up and cooling down the sample (e-h) and the ODMR evolution changes but the NV pair (NV B, NV D) still show similar features in their ODMR lines.

A similar pattern is found in the second experimental run, presented in the panels (e)-(h) of Figure 3.6. I observe that the magnetic response of each NV changes after a warm up/cool down cycle. This suggests that no pinning sites for the magnetic domains are present at the NV locations. The similarity between NV B and NV D however is preserved. In this run I also notice that NV C displays an ODMR evolution which resembles NV B and NV D, being spatially closer to the two emitters than NV A. This reinforces the indication that the spin texture orientation changes within the distance that separates NV A from the other emitters.

In both runs, I observe that some ODMR temperature traces display a splitting reduction occurring at low temperatures. This can be due to two effects: either a reduction of the magnetic field amplitude or a rotation of the magnetic field vector, which reduces the projection of the magnetic field along the NV axis. I attempt an answer by observing the response of NV B in Figure 3.6. Above the Curie temperature, the two pairs of resonances respond differently to the same bias field, meaning that they lie along different crystallographic axes. Below the critical temperature, the outer resonance pair is increasingly split for decreasing temperatures. A reduction in the splitting however is not observed in the temperature range where the Zeeman shift of the other pair is decreased. This type of evolution indicates that, at least for NV B, the splitting reduction is due to a rotation of the magnetic field vector. A rotation can be explained different scenarios. In one case, while the sample warms up, the magnetic domains can change shape and size. The change in the spin texture then affects the stray field at the NV locations. Another explanation can be given by the structural phase transition occurring at 103 K (Sec. 3.1). The change of crystalline order can modify the direction of the magnetic easy axis and lead to a reorientation of the spin texture.

Another feature which is apparent from the ODMR traces in Figure 3.6 is the increase in linewidth occurring when there is non-zero stray field. An increase in linewidth is expected, since the slow noise induced by the ordered spins decreases the coherence time of the NV. The linewidth as a function of temperature for both runs is plotted in Figure 3.7(a-h), as extracted from the fits. The broadening of the resonance not only increases below the Curie temperature, but is also correlated with the Zeeman splitting. When the splitting decreases, the linewidth also decreases. The broadening could be entirely explained by a change in the noise environment linked to the decrease of the Zeeman splitting. However, if ODMR spectra which are averaged to form the ODMR response at a fixed temperature are plotted versus time, one can observe an oscillation of few MHz with a period of about 20 minutes. Such a slow timescale is not compatible with the dynamics of the spins in PCMO.

We verify that the noise source is due to laser-induced demagnetisation. I am going to explain in further detail the origin of the observed noise in Section 3.4.4.

All the measurements presented so far rely on CW measurements of the stray fields. However, in the last paragraph I have highlighted the existence of time-dependent dynamics in the system. DC measurements are not suitable to investigate them. To gain further insight in such dynamics, we make use of pulse sequences,

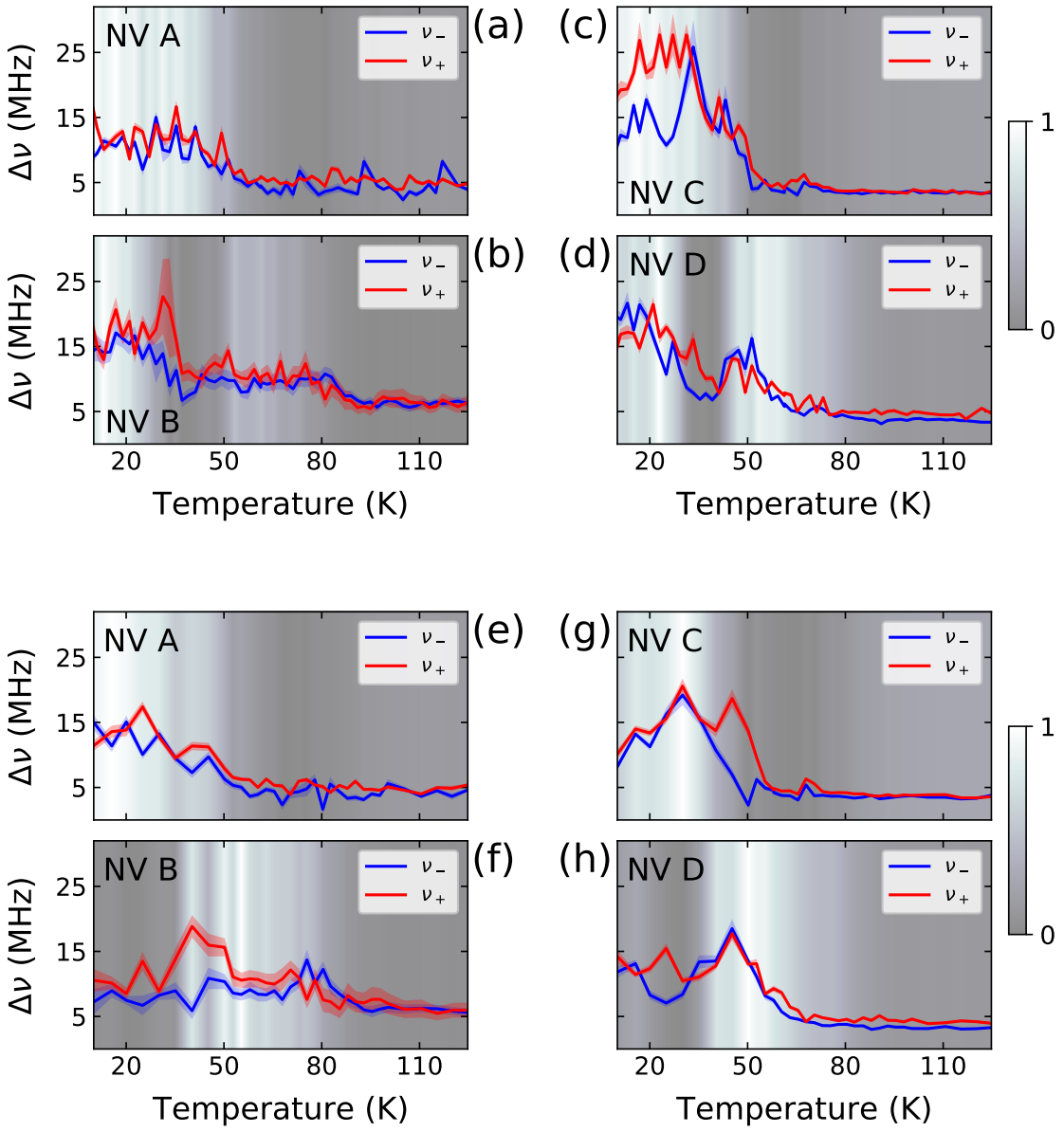

Figure 3.7: Linewidth of the ODMR resonances of NV centres on PCMO as a function of temperature. ν_- and ν_+ correspond to the lower and higher energy transition, respectively. The background of each plot is the normalised Zeeman splitting of the corresponding NV. The data are extracted for both the first experimental run (a-d) and for the second one (e-h). I observe that for each NV and for each run, the linewidths are correlated with the Zeeman splitting. A large splitting correspond to a large linewidth and viceversa. The shaded areas indicate the fit error.

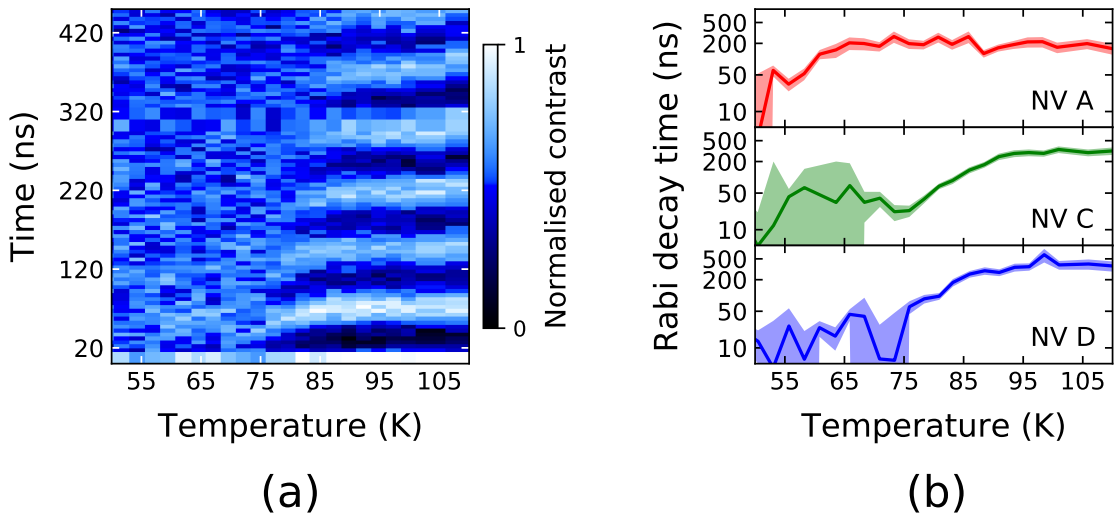

Figure 3.8: Measurement of the local magnetisation temperature using NV centres. (a) Rabi oscillations as a function of temperature measured on NV D in increments of 5 K. ordering arises when cooling through the magnetisation temperature, the NV decoherence time drops rapidly. (b) Decay time of the Rabi oscillations for different NV centres. The arrows mark the local magnetisation temperatures extracted using the double tangent method. While NV C and NV D sense similar magnetisation temperatures around 96 K, the NV A signal decays at ∼66 K indicating that magnetic ordering occurs at a different local magnetisation temperature at the location of NV A. NV B has a short $T_2 \approx 60$ ns and thus cannot be used to precisely estimate the local magnetisation temperature. The shaded area corresponds to the fit error.

namely of Rabi oscillations.

3.4.3 Rabi oscillations

In the conditions described above, performing a Ramsey or a spin echo sequence becomes challenging. Rabi oscillations, on the other hand, do not require the knowledge of the π-pulse time and are still sensitive to magnetic noise which is resonant with the transition energy. Using a pulsed measurement sequence also decreases the average optical power applied in CW, with about a 50% duty cycle.

The Rabi measurements were taken after each ODMR spectrum. The MW excitation frequency for the Rabi sequence is adjusted to each of the NV resonances at a fixed temperature point. The Rabi excitation power is always kept at -1 dBm. I show a typical plot of the Rabi signal versus temperature in Figure 3.8(a). Above the local magnetisation temperature there are clear oscillations, with a π-pulse time of about $T_\pi \approx 30$ ns. As the temperature approaches the transition, the Rabi frequency changes from the zero-field value. At lower temperatures, the coherence time of the oscillations drops sharply. No signal is observable past this transition. The same trend is observed with all the NV centres.

I fit each trace with the function $f(t) = A \sin(\Omega t)\, e^{-t/\tau} + y_0$. I plot the temper-

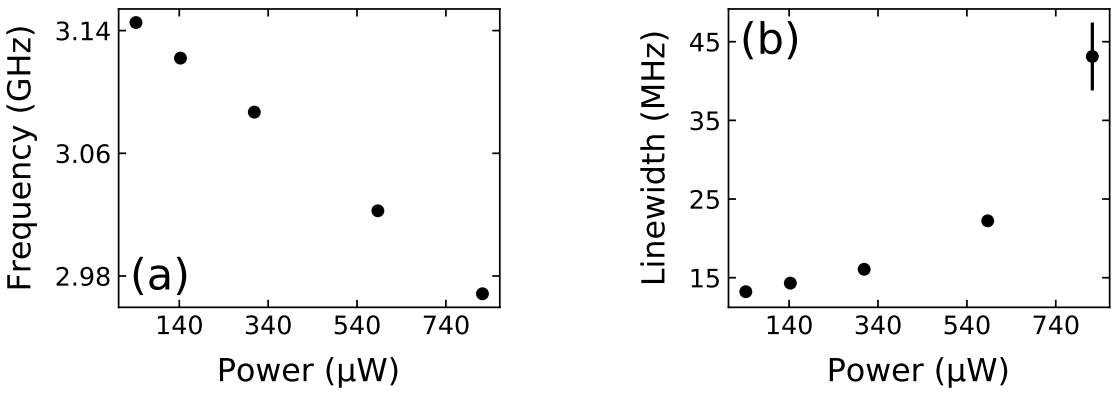

Figure 3.9: Power dependence of the ODMR of NV centres on PCMO/STO at 4 K. (a) Zeeman shift of the high-energy transition of the NV ground state as a function of optical excitation power. The splitting depends linearly on the optical power, with a slope of $-0.23\,\mathrm{MHz}/\mu\mathrm{W}$. (b) The linewidth of the same resonance. The error bars are not shown where they are smaller than the data points.

ature evolution of the τ parameter in Figure 3.8(b). I do not show the fit results for NV B because the signal-to-noise ratio is too low to obtain reliable fits. NV A dephases at a temperature of $T_m = 66 \pm 8\,\mathrm{K}$, while NV C and NV D dephase at $T_m = 95 \pm 9\,\mathrm{K}$ and $T_m = 97 \pm 11\,\mathrm{K}$, respectively. I stress that NV C and NV D are belong to the group of emitters separated by less than $1\,\mu$m. The magnetisation temperatures detected by NV C and NV D occur at a temperature which is close to the Curie temperature detected using the SQUID magnetometer. NV A, more than $2\,\mu$m away from the other emitters, on the contrary detects magnetism only 20 K below. These results corroborate the hypothesis of domains forming at different locations at different temperatures. Here I stress that I have plotted only the τ parameter but also the other two fit parameters (amplitude and Rabi frequency) lead to the same conclusions.

3.4.4 Laser-induced demagnetisation

In the previous section I have commented on the increase of ODMR resonance linewidth and its correlation with the Zeeman splitting. In this section I investigate the origin of this behaviour.

We first check the power dependence of the Zeeman splitting at 4 K with the laser power. I show the results in Figure 3.9(a,b). At extremely weak excitation powers ($P = 40\,\mu$W) the NV highest energy resonance is shifted by 275 MHz, which correspond to almost 10 mT of magnetic field projection (Fig. 3.9(a)). When the excitation power is increased, the splitting drops linearly with a slope of $-0.23\,\mathrm{MHz}/\mu\mathrm{W}$. At $822\,\mu$W the Zeeman shift is reduced to $\sim 2.97\,\mathrm{GHz}$, which corresponds to a stray

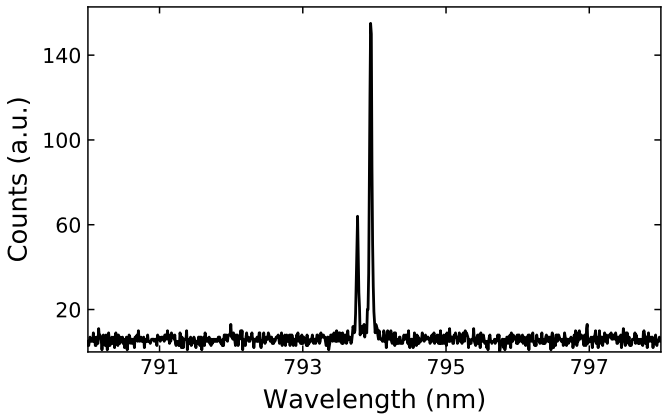

Figure 3.10: Fluorescence spectrum of PCMO/STO at 8 K, using an excitation laser at 532 nm with a power of 500 μW. I notice two sharp fluorescence peaks at 793.7 nm and 793.9 nm.

field of ~ 3 mT. At higher powers, the ODMR contrast for this specific NV is too low to observe a signal. The linewidth of the resonance (Fig. 3.9(b)) is both influenced by the magnetism of the thin film, as discussed above, and by the optical power broadening. Below 500 μW the linewidth increase is only ~ 11 kHz/μW.

Such a strong effect of the optical power on the magnetisation can stem from different effects. Photons can interact with the electron energy bands and alter the spin-spin interactions that induce the ordering [139], leading to either the creation or the destruction of the magnetic ordering. Photo-induced magnetisation was observed in bulk $Pr_{0.6}Ca_{0.4}MnO_3$/STO thin films at cryogenic temperatures [140]. Two fluorescence peaks at 793.7 nm and 793.9 nm using 532 nm excitation, coming from the PCMO/STO thin film below 150 K, are observed. This might indicate that photons are indeed absorbed by the sample and destroy the magnetic ordering of the material. However, we could not verify whether the emission occurs from the PCMO thin film itself or from the underlying STO sample.

The second effect that can explain the laser-induced demagnetisation is simply due to a local change of the surface temperature. To verify this hypothesis, we first benchmark the setup response at room temperature, exposing the sample stack to the laboratory atmosphere by removing the cryostat chamber enclosure. We locate an NV centre and we record the photon counts, along with the laser power detected by the photodiode and the temperature measured by the sample thermocouple (Fig. 3.11(a)). The data are acquired by running an ODMR experiment without applying microwaves. The top panel shows that there are temperature oscillations of 0.2 K peak-to-peak at the sample location, centred on ~ 295.8 K and with a period of 20 min. The oscillations are caused by laboratory air conditioning proportional-integral-differential (PID) loop, which tries to stabilise the tempera-

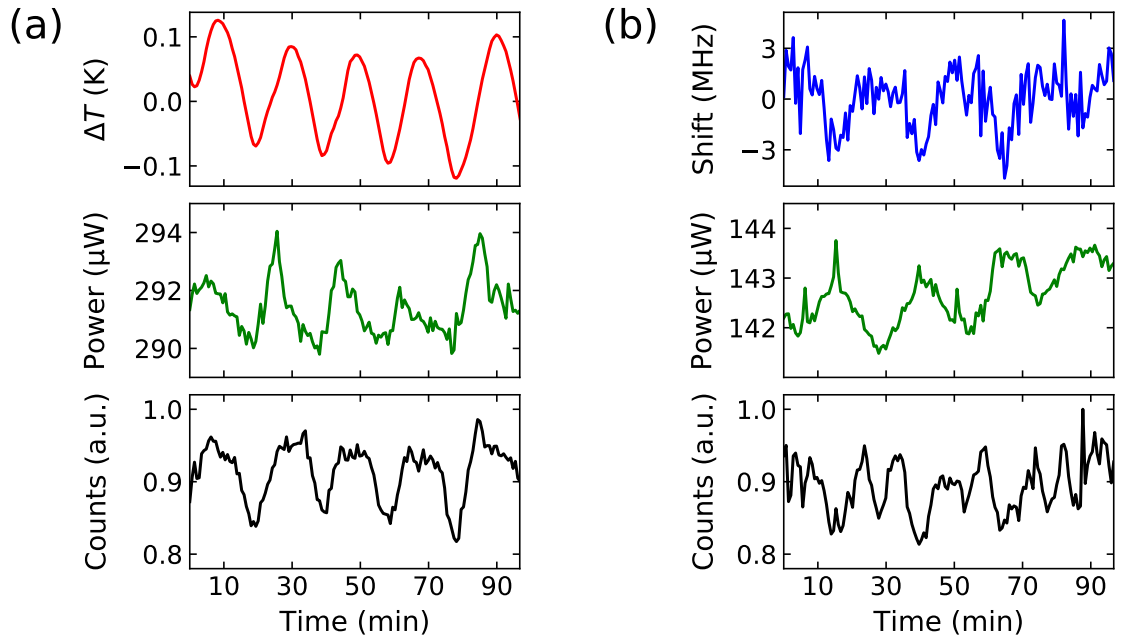

Figure 3.11: Laboratory temperature oscillations and the effects on the ODMR signal at low temperatures. (a) At room temperature, the thermocouple can record the laboratory temperature (top panel), which oscillates around a mean value of 295.18 K. The laser power (middle panel) and the fluorescence counts of an NV centre are correlated with the temperature oscillations. (b) At 8 K, oscillations of the photon counts (middle panel) and photon counts (bottom panel) are correlated with the oscillations of the ODMR resonance, which oscillates around a mean value of 3.122 MHz. All the data are acquired while running an ODMR experiment. At room temperature no microwaves are sent to the sample.

ture at a target of 294.15 K. The photodiode signal and the NV fluorescence counts show oscillations which are correlated with the temperature oscillations. This means that the temperature affects the confocal microscope, slightly changing its focus over time. The sample is then cooled down to its base temperature and the measurement repeated. This time we acquire an ODMR spectrum at each datapoint. We do not track the sample temperature, because the thermocouple cannot detect changes in the local surface temperature with the active cooling of the cryostat. I show the results in Figure 3.11(b). The fluorescence counts and the photodiode oscillate with the same period as the one measured at room temperature. The ODMR resonance frequency, shown in the top panel of Figure 3.11(b), is correlated with the other two signals. In particular, the maxima of the resonance oscillation are anti-correlated with the laser power.

The last measurement suggests that the ODMR resonance periodic shift –and thus the ODMR broadening observed in Figure 3.7– is most likely caused by laser-induced surface heating. Although during the measurements we make sure to run at low powers ($< 150\,\mu$W), the laser excitation can have a dramatic effect on the

magnetisation and thus on the Zeeman splitting of the NV.

3.5 Conclusions

Using nanodiamonds drop-casted on the surface of PCMO/STO, we have measured the temperature-dependent Zeeman splitting caused by the stray fields forming below the Curie temperature. We select few emitters and we compare the respective Zeeman shifts to their location in the PL map. The similarities of the ODMR splitting trend indicate that the PCMO/STO magnetic domains might have a size of the order of few μm. Using pulsed measurements, we observe that Rabi oscillations dephase quickly when the magnetic transition occurs. The signal vanishes entirely within the range only 20 K. The analysed NV centres measure a magnetisation temperature which differs from the SQUID measurements. This might indicate that domains from at different temperature, depending on the location in the thin film. We also verified that the most likely cause for the ODMR resonance linewidth broadening is the laser-induced heating of the surface.

If on one hand drop-casting nanodiamonds on the surface of magnetic materials provide a spatially stable probe and ensures small NV-to-sample distance, on the other it does not allow for high resolution imaging of the stray fields. This complicates the interpretation of the results and can lead to wrong conclusions for what concerns the physics of a magnetic thin film. Whenever possible, the technique should be combined with other established imaging methods to provide insight into the local behaviour of a material [141].

NV centres in nanodiamonds can still be used for magnetic field imaging if grafted to the tip of an AFM cantilever. This technique however requires a different setup configuration, which will be discussed in the next chapter.

Chapter 4

Scanning NV magnetometry with an optical readout AFM

In the previous chapter, I have discussed the details of using nanodiamonds drop-casted on the surface of magnetic materials to study the spatial-dependent stray fields. The complex stray field patterns generated by magnetic domains however are difficult to interpret if scattered point probes of magnetic fields are to be used.

In this chapter I will discuss the work done towards implementing a scanning NV magnetometer which operates with the aid of a room temperature optical readout AFM [48]. If the object to be imaged is a magnetic sample deposited on a substrate, NV centres in nanodiamonds can be grafted on an AFM tip and scanned across the region of interest. Otherwise, the nanodiamonds (or shallow NV centres implanted in bulk diamond) can be deposited on the substrate and a magnetic sample attached to the AFM tips is scanned over the NV.

The data on the stray fields from MFM tips were acquired by Michael Högen.

4.1 Atomic force microscope

The atomic force microscope which is used in these experiments is an Asylum Research MFP3D-BIO. This type of confocal microscope has been specifically designed to operate with commercial confocal systems for biology and thus has optical access underneath the scanning head. The core of the AFM microscope is the AFM head, onto which the cantilever is mounted. The head houses the superluminescent diode (central wavelength: $\lambda_0 = 830\,\mathrm{nm}$) which illuminates the top of the cantilever. The quadrant photodiode which is used to read out the cantilever deflection is also housed in the AFM head. The cantilever mount is integrated with a closed-loop piezoelectric stage which controls the vertical position of the cantilever, with a range of $20\,\mu\mathrm{m}$. A

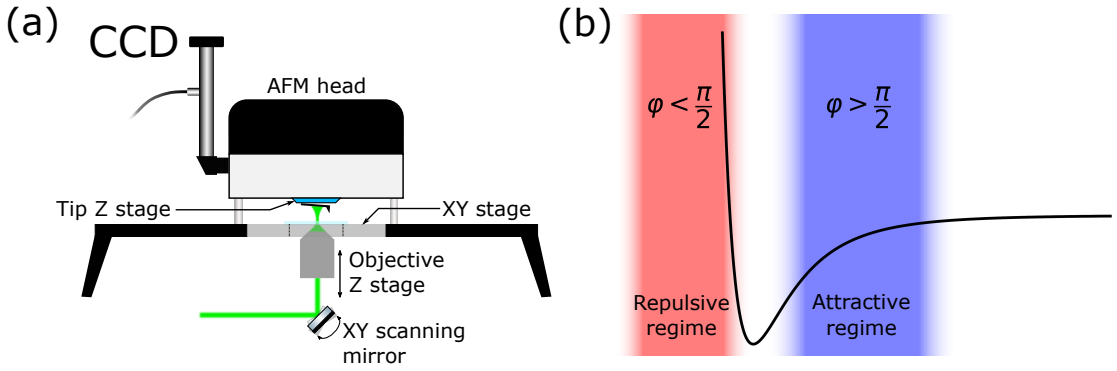

Figure 4.1: (a) Schematics of the atomic force microscope/confocal microscope for scanning NV magnetometry. A fibre-coupled white light source is collected by an objective and sent through the AFM head to the tip area. The back-reflected light is then imaged by a CCD camera. The AFM head also provides the illumination for the cantilever and houses the quadrant diode for the cantilever deflection readout. The cantilever vertical position is controlled by a closed-loop piezoelectric stage. The AFM scanning is achieved by a closed-loop xy-stage on which the sample is mounted. An inverted confocal microscope can access the the AFM underneath the AFM head. The confocal objective is controlled by a z-piezo stage. A piezo-electric mirror can steer the beam to achieve PL raster scanning. (b) Approximate probe-sample interaction potential. The tip is most sensitive to the topographic features in the repulsive regime. In tapping mode, the attractive regime corresponds to a phase $\varphi > \pi/2$, while the repulsive regime corresponds to a phase $\varphi < \pi/2$. The out-of-contact phase is $\varphi = \pi/2$.

white light from a fibre-coupled light source is focused by an objective also housed in the head to illuminate from the top the cantilever area. The wide-field image is formed onto a CCD camera, which collects the back-reflected light. Wheels on the side of the AFM head allow for optimisation of the optical readout beam, to zero the offset read by the four quadrant diode and to achieve coarse approach to the sample. Scanning of the xy-plane can be done with a closed-loop piezoelectric stage, onto which the sample is mounted, with a maximum range of 90 μm. Two pairs of micrometric screws on the AFM plate allow for coarse positioning of the sample under the cantilever tip or to move the whole plate (AFM head and sample) to a new xy position. The whole AFM assembly and the confocal microscope –which is described below– rest on a minus-K stage for vibration insulation.

As discussed in Section 2.9, this AFM has two main operation modes: contact mode and tapping mode. In order to operate in contact mode, the only parameter to be tuned before scanning is the deflection set-point, which sets the voltage of the quadrant photodiode on which the PID loop feedbacks. The output channels of the AFM in this mode are the height channel –the voltage of the z-piezo corrected by a conversion factor-, the Z sensor channel, which is the motion of the z-piezo stage tracked by the closed loop sensor, and the deflection channel, i.e. the error signal fed to the feedback loop which controls a constant deflection. The voltage set-point s_0 needs to be $s_0 > 0$ for an initial deflection signal $s = 0$. A large s_0 value corresponds

to more force applied to the sample by the cantilever.

The tapping mode requires the optimisation of a few additional parameters before a scan can be attempted. The first parameter to be tuned is the frequency of the dither piezo which excites the vibrational modes of the cantilever. This is done by scanning the frequency of the AC voltage applied to the dither piezo and by detecting the voltage on the quadrant photodiode. The highest-amplitude resonance is then selected and the excitation is applied at the resonance frequency. The phase reference of the AC driving is shifted so that the phase at resonance is $\pi/2$. In this way the remaining free parameters are the amplitude of the dither piezo voltage, which also sets the amplitude of the cantilever oscillation, and the feedback set-point. In this case s_0 needs to be a value smaller than the free-oscillation amplitude s, since the oscillation is reduced when the sample surface is approached. The initial s_0 is usually set to $0.8\,s$. When the cantilever is in contact with the sample, the phase is an important parameter to be taken into account. The interaction between tip and surface can be approximately described by a Lennard-Jones potential. The interaction forces can be distinguished into long-distance attractive forces and short-distance repulsive interactions. The correct imaging conditions are achieved only when the probe-surface interaction is repulsive. The resonance phase φ is related to these interactions and can be used to correct the set-point to enter in the repulsive regime. When $\varphi > \pi/2$, the interaction is attractive, while if $\varphi < \pi/2$ the interaction is repulsive.

The coefficient that is used to convert the deflection amplitude signal into the amplitude is of particular importance if quantitative imaging of the surface topography is required. Knowing the amplitude of the oscillation in tapping mode is also important for NV magnetometry. Indeed, the period and the amplitude of the cantilever oscillation can induce broadening of the ODMR resonance when an NV grafted to the cantilever tip moves inside a magnetic field gradient [142]. A precise control of the oscillation amplitude is needed when the average NV-to-sample distance needs to be controllably reduced. The cantilever oscillation amplitude can be controlled with two different methods. The first method can be used with commercial AFM cantilevers. In this case the dimensions and the material of the cantilever are known and stored in a database which can be accessed by the AFM software. The elastic constant and the optical lever sensitivity (OLS) (defined as the ratio between the cantilever deflection and the displacement of the z piezo) can then be retrieved by recording the thermal vibration of the cantilever resonance in the absence of piezo driving.

Alternatively, if the parameters of the cantilever are not known, the oscillation

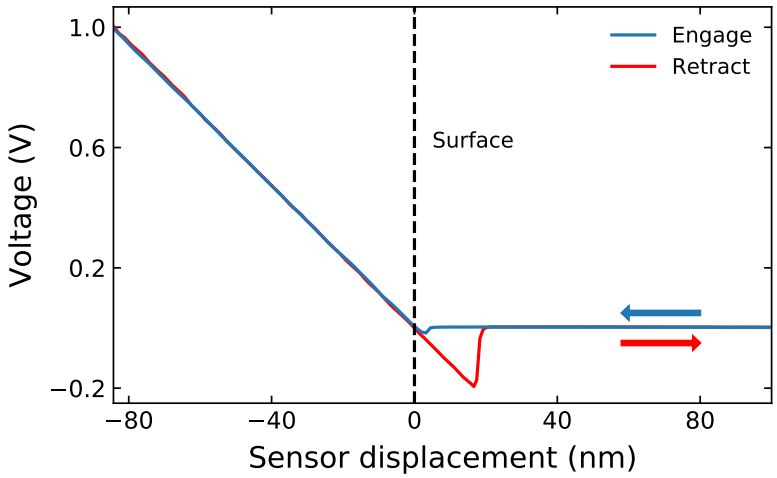

Figure 4.2: Force curve of a silicon tip on a quartz coverslip. The tip is moved towards the sample surface from far away (positive displacement area). Few nanometers before the surface is reached, the tip "snaps" to the surface, because of the van der Waals forces. In the case of an ideal hard surface which does not interact with the tip the dip would not be visible. The piezo pushes the tip against the surface. This causes a linear increase of the quadrant photodiode voltage until the set-point is reached (in this case it corresponds to 1 V). The z-piezo then lifts the cantilever up to the initial position. Notice that when the cantilever is being retracted the adhesive forces cause the tip to snap back to its unperturbed position at a larger sensor displacement.

can still be calibrated. The cantilever OLS can be retrieved by taking a force curve. A force curve consists essentially of four steps. The cantilever, initially out of contact, is lowered towards the surface. When the tip is contact, it is pushed down further until the used-defined deflection setpoint is reached. The cantilever is then retracted. A typical force map is shown in Figure 4.2. The slope of the position-deflection curve is fit to obtain the OLS. In order to obtain a correct estimation of the OLS, it is important to perform the calibration on the surface of a clean, hard material, which does not tend to form bonds with the tip (i.e. as a silicon sample with a silicon tip). The enhanced probe-sample interaction introduces nonlinearities in the force curve that lead to an incorrect estimation of the OLS. Once the OLS is measured, the spring constant can be obtained by capturing and fitting the thermal vibration of the cantilever.

The complexity of the AFM system requires a central control system which is able to coordinate each signal during an AFM scanning and to respond quickly to changes in the scanning conditions, e.g. topographic features on the sample surface. In particular, the feedback loop which controls the cantilever height cannot be reliably closed through software because of lags which can lead to the probe destruction. The signals are elaborated by digital signal processor (DSP) which reads the position of the piezo, applies the feedback and generates a voltage (range: $0 - 10$ V). The voltage is then converted to an analog signal by a digital-to-analog

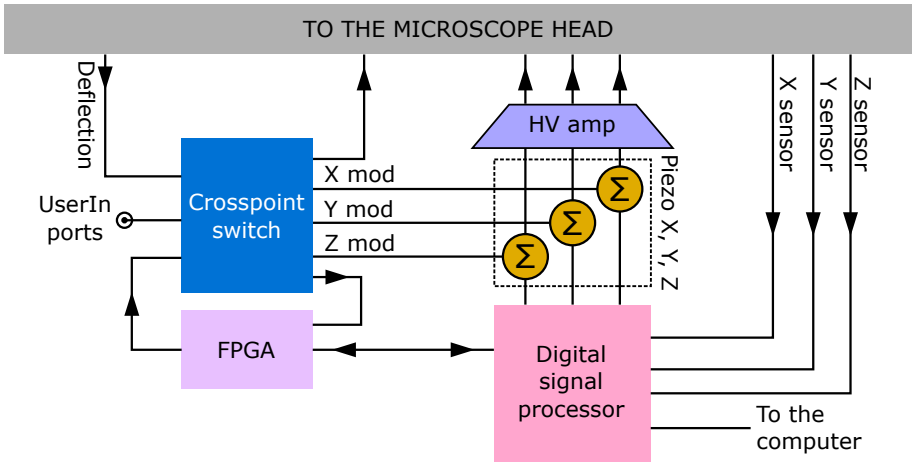

Figure 4.3: Simplified block diagram of the AFM controller. The digital signal processor and the FPGA control the inputs and outputs of the signals of from and to the AFM head. The crosspoint switch is a unit which can be programmed by the user to remap and activate electrical connections within the AFM controller. For example, the signals connect to the UserIn ports can be connected to the X, Y, Z modulation, which are added to the voltage generated by the digital signal processor.

converter (DAC) and then amplified by an amplifier with gain $G = 150$. User defined ports allow the user to input or read analog voltages between 0 V and 10 V.

4.1.1 Integration of the confocal microscope

The main body of the confocal microscope follows the scheme described in Section 2.7. The microscope objective, as shown in Figure 4.1(a), is mounted in an inverted configuration and illuminates the sample area from underneath. This requires the sample substrate to be transparent, in order to excite the NV centres on the top surface of the substrate and to collect their fluorescence. The substrate used in this experiments are 200 μm-thick quartz coverslips (CFQ-1520, UQG optics). The objective has an aberration-correction ring (Zeiss LD Plan-Neofluar 63x/0.75 Corr M27) which corrects for the optical aberration of the substrate. The objective vertical position is controlled by a closed-loop linear stage (Q-545, Physik Instrumente) with a resolution of 1 nm. Raster scanning is achieved with a tip-tilt mirror (S-334, Physik Instrumente). I observe that when the microscope objective is focused on the top surface of the quartz coverslip and the AFM cantilever is in contact with the surface, with the deflection readout on, the light of the superluminescent diode couples into the confocal microscope. Since the collection arm was initially equipped with long-pass filters with a cut-off wavelength $\lambda = 561$ nm (BLP02-561R-25, Semrock), the NIR photons are detected by APD, which then returns an average count rate of ~ 500 kHz even when the confocal is not collecting light from an emit-

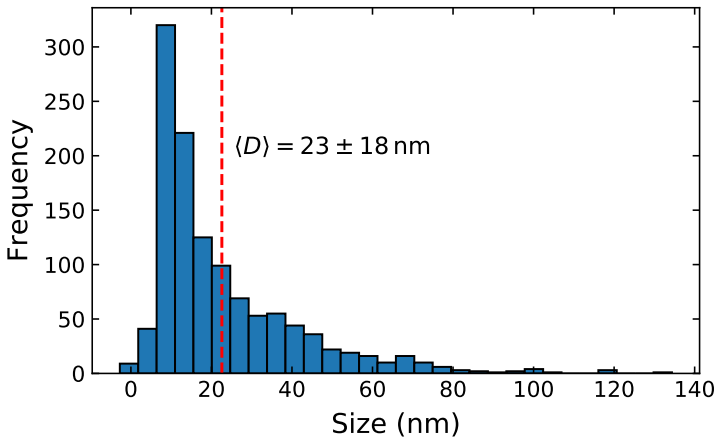

Figure 4.4: Histogram of the nanodiamond size, obtained by analysing the nanocrystals dispersed on a quartz slide. The average nanodiamond size is $\langle D \rangle = 23 \pm 18\,\text{nm}$, for a statistical sample size $N = 1188$.

ter. Hence, I add an additional shortpass filter with a cut-off wavelength of 750 nm (750nm 25mm Diameter, OD 4 Shortpass Filter, Edmund Optics). The CCD camera also images the NIR light from the cantilever optical readout beam, since it picks up the light in the excitation arm. This is useful, since it allows to form an image of the shadow of the cantilever tip when in contact, and thus allows precise alignment of the confocal spot with the AFM tip, as I am going to describe in Section 4.3.

4.2 Nanodiamond sample preparation and characteristics

The nanodiamonds which are drop-casted on the coverslip are prepared in a solution. I use two different types of nanodiamond crystals and solutions. The first type of nanodiamonds are milled from high-pressure high-temperature bulk diamond, with a nitrogen concentration between type Ib and type IIa diamond from NaBond. These diamonds are the same ones used in the PCMO sensing experiment 3.4.1. I prepare the solution by dispersing 10 mg of nanodiamonds in 25 ml of EtOH. The purity of the diamond ensures that most of the fluorescent nanodiamonds contain single NV centres. On the other hand, most of the nanodiamond will not contain any NV (Sec. 4.3). The other nanodiamonds I use are from Adamas (NDNV40nmLw10ml), which are sold already in a 1 mg ml solution of deionised water. Most of these nanodiamonds are fluorescent, but on average they contain more than one NV centre.

Prior to deposition, the nanodiamond solution is sonicated for 1 h in order to

break up nanodiamond clusters which naturally form when the nanodiamonds deposit at the bottom of the container. The quartz slides are sonicated for 10 min in acetone and for 10 min in isopropanol, in order to ensure a clean surface. The nanodiamonds can be dispersed with two methods. Using a pipette, $\sim 20\,\mu$l of solution are deposited on the glass slide, which is subsequently rinsed with deionised water. The other method uses a nebuliser to spray the solution directly on the glass slide. The drop-casting method gives a high nanodiamond concentration but can create inhomogeneity in the nanodiamond distribution if not executed correctly. The nebuliser ensures an even nanodiamond distribution across the sample, at the expense of a lower density of nanodiamonds per deposition. Usually, if the drop-casting method is used, I further dilute the solution to avoid having a too high density of nanodiamonds on the surface.

Figure 4.4 shows a typical histogram of the nanodiamond size distribution. I see that the average size of the diamonds is 23 ± 18 nm, while the mode is 6.4 nm. The small size of the nanodiamonds thus ensures a small sample-to-probe distance.

Above I commented on the influence of the diamond purity on the amount of emitters relative to the nanocrystal number. I can evaluate this number by measuring the surface topography and comparing it to the PL map of the same area. I show the result of the AFM/CFM scans in Figure 4.5. The top row (Fig. 4.5(a, b)) is obtained from a quartz slide with dispersed NaBond nanodiamonds, while the bottom row shows the maps of a sample with Adamas nanodiamonds (Fig. 4.5(c, d)). The topography map of the NaBond sample shows that the surface has a high density of nanodiamonds. The PL map of the same area, however, shows that most of the nanodiamonds do not contain NV centres, with only $\sim 1\%$ displaying fluorescence. The Adamas sample shows the opposited trend. A low density of nanodiamonds yields an emitter density comparable to the one observed for the NaBond sample in Figure 4.5(b). However, not all the emitters are single NV centres or yield an ODMR with good contrast (i.e. $\gtrsim 10\%$). This reduces the number of NV centres suitable for scanning NV magnetometry even further. It is thus important to ensure that the nanodiamond concentration allows to resolve single nanodiamonds on the surface, while yielding at the same time a high amount of single NV centres with high ODMR contrast.

4.3 Synchronisation of the AFM/confocal scans

Any scanning NV magnetometry experiment requires the synchronisation between the AFM and the confocal microscope. At each pixel, the scanning stage needs to

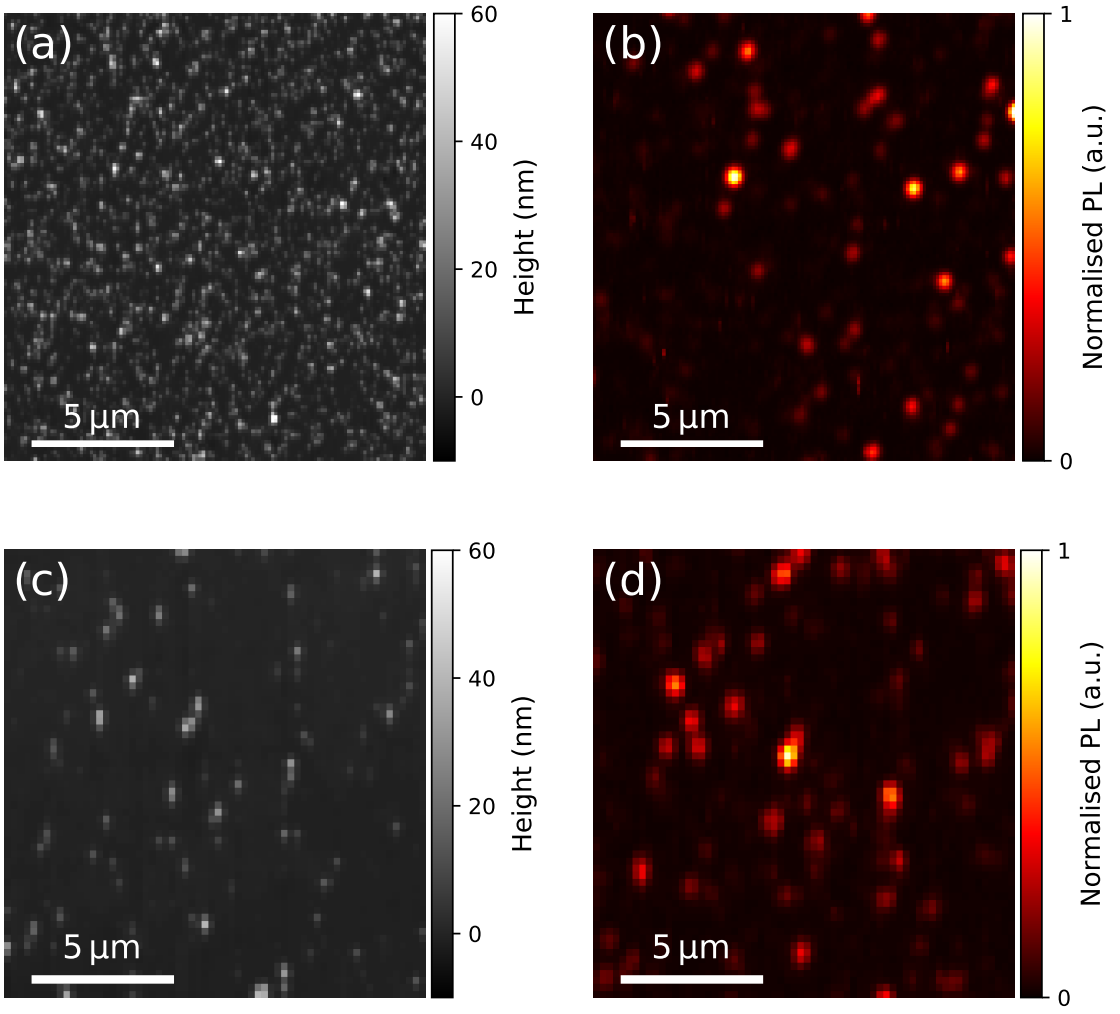

Figure 4.5: NV centre concentration using different types of nanodiamonds (NaBond and Adamas). (a) Topography of NaBond nanodiamonds dispersed on a quartz slide and (b) the PL map of the same area. The large amount of nanodiamonds corresponds to only few emitters observable on the PL map. (c) Topography of Adamas nanodiamonds dispersed on a quartz map and (d) the respective PL map. The Adamas nanodiamonds have a much larger impurity content, which results in a higher yield of NV centres.

wait for an experimental sequence to be completed, whether it is PL acquisition, ODMR sequence or more complex and long pulse sequences. The MFP-3DBIO allows for a few different strategies to achieve this, which I will discuss below. In order to choose the best control type, I have to choose whether to operate the AFM in "master" mode – the AFM software and hardware controls the rest of the hardware, possibly through an additional software – or in "slave" mode – a main software controls all the hardware, including the AFM, and acquires the data accordingly.

The first synchronisation solution consists in operating the AFM in master mode and feeding the photon counts into the AFM controller. The AFM controller has indeed an external module, called External Digital Interface Module (EDIM), which

allows the user to input voltage pulses, which are to be read by the AFM controller. The photon count acquisition can then be achieved by connecting the APD output to the EDIM. In this way the AFM scanning is automatically synchronised with the PL count acquisition without the need of an external software. However, the pulse width of the electrical pulses generated by the APD is $\sim 20\,\text{ns}$, while the timing resolution of the AFM controller counter is 25 ns. This means that most of the time the AFM controller controller does not record any photon count. I circumvent this by adding a custom-built pulse extender, which detects an incoming rising edge and generates a square pulse of user-defined width. This solution however is not optimal, because it introduces additional noise, related to the limitations of the pulse extender. I thus decide to record the photon counts using a DAQ card and a custom software, which I also use to control additional hardware like the objective piezo stage, the scanning mirror. The software creates an analog voltage output which ranges from 0 V to 10 V and is proportional to the photon counts. The maximum count rate, which corresponds to 10 V, is user defined. The analog signal can then be fed into one of the UserIn ports of the AFM controller, which can be read during an AFM scan. While this method can be an efficient and simple solution to acquire AFM maps and PL maps, there is no additional synchronisation signal shared between controller and computer. This has two consequences: the user needs to make sure that the integration time of the photon counts is of comparable length or shorter than the AFM integration time; running longer sequences is likely to induce non negligible lags between the NV measurement sequence and the AFM scan.

The AFM scanning and the data acquisition software can be threaded together using the AFM controller as a clock that coordinates the whole setup. The FPGA of the AFM controller generates voltage pulses during a scan. The pulses are distinguished into "pixel" pulses, which signal the step to a new pixel, "line" pulses, indicating the start or the end of a line, and "frame" pulses, which are generated after a full scan is completed and a new one is started(Fig. 4.6). The pulses can be accessed through three channels on the EDIM. During a scan the sample scanner traces and retraces each line which makes up the AFM scan before moving to the next one. The direction along which this motion happens is known as slow axis, while the direction towards which the scanner steps upon the completion of a slow axis is called the fast axis. Because of the tracing and retracing, the AFM uses extra pixels, which are not plotted in the AFM map, in order to invert the scanning direction. These extra pixels are called the "turnaround" region. The turnaround region pixels are about 25% of the plotted scan pixels. For example, if the scan resolution is 256 px, the total pixels will be 32 px (half-turnaround) + 256 px (trace)

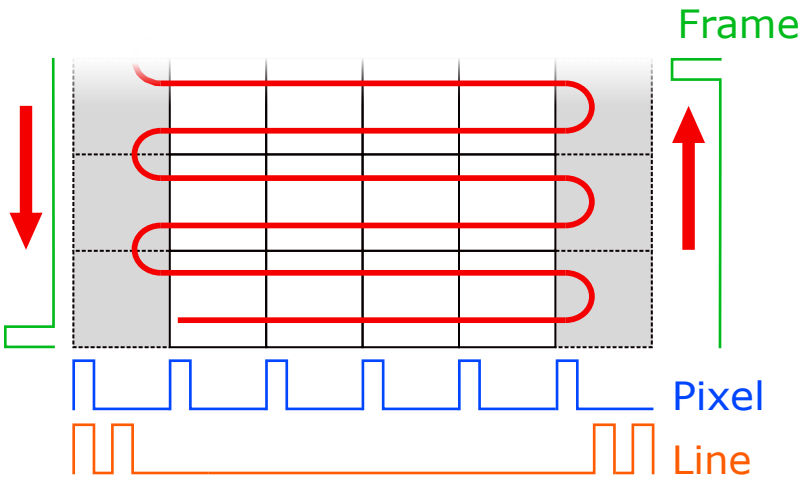

Figure 4.6: Schematics of an AFM scan. The xy scanner moves the sample along the horizontal axis, called also the fast axis. At the end of the scan area (white background), there are few extra pixels, not recorded by the AFM software, which are used as a "turnaround" area (grey background). After tracing and retracing the fast axis, the scanner makes one step towards in the vertical direction, called also the slow axis. When the whole scan is completed – a frame – the scanner retraces back the same trajectory. The AFM outputs a pixel pulse at each new pixel (also in the turnaround area), a line pulse in the turnaround region, while moving forward, and another line pulse when starting the retrace. An additional frame pulse is output each time the scan is completed.

+ 64 px (full turnaround) + 256 px (retrace) + 32 px (half-turnaround). The EDIM outputs all the pixel pulses, including the ones in the turnaround region. There are two line pulses in the turnaround region, one indicating the end of a trace (retrace) and one indicating the start of the retrace (trace). A frame pulse is generated synchronously with the first line pulse of a scan frame. All the pulses can be read out by the software to launch the data acquisition. Receiving the pulses however does not ensure full synchronisation in the case where the AFM pixel integration time is shorter than the NV measurement time. This can be avoided if the AFM is reprogrammed to wait for a pulse sent by the DAQ card through the acquisition software at the end of the NV acquisition sequence. Moreover, a scan control designed in such a way requires the user to input the number of AFM scan pixels in the NV acquisition software.

The synchronisation issues can be overcome if the software can control the AFM scanning. This can be done by using two analog voltage channels of the DAQ card and generate a grid of voltages which are fed into the user input ports. The crosspoint switch can then be reprogrammed to route the two channels to the X and Y modulation ports. The modulation ports are added to the internal x and y voltages generated by the DSP and then amplified by a high voltage amplifier which is sent to the xy scanners. The z motion is still coordinated by the AFM software in order to avoid any latency issue, which can arise if the loop is closed externally

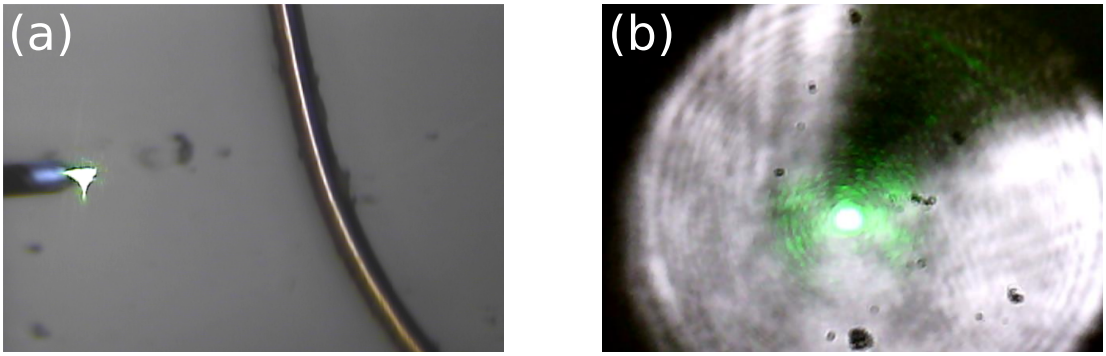

Figure 4.7: Coarse alignment of the confocal microscope with the AFM. (a) The wide field imaging is used to achieve rough positioning of the confocal spot (bright green spot) on the tip of the AFM cantilever (black arrow). The wide field image also shows the cantilever readout beam (blue spot on the cantilever) and a copper wire used to deliver the microwaves to the NV. (b) Wide field image of the confocal CCD. The shadow of the AFM tip is visible thanks to the top illumination of the cantilever readout beam. The green spot is the confocal beam focused on the top surface of the sample substrate.

to the AFM hardware. The z coordinate can be read out by the NV acquisition software through the front panel of the AFM controller, which outputs the signals generated by the AFM sensors. Although synchronisation issues can still arise for fast scanning, NV measurements take at least $\sim$ 20 ms per pixel, making signal delays negligible. The simplicity of this solution however comes at the expense of closed-loop scanning. The full scan range is also reduced from 90 μm to 15 μm.

Prior to a NV magnetometry experiment, the confocal microscope and the AFM coordinate systems need to be matched. When the scanning tip is in contact with the surface and the confocal microscope is focused on the same plane, there is still a xy shift between the tip position and the confocal spot. In this condition, the topography and the PL maps during the scan are decoupled. A first coarse alignment can be achieved with the following steps. First, using the AFM wide field imaging, the tip of the cantilever is aligned with the confocal spot (Fig. 4.7(a)) using the xy micrometric positioners which adjust the position of the whole AFM plate. If a satisfactory alignment is achieved, the shadow of the AFM tip can be seen on the confocal CCD camera, together with the confocal spot. A finer alignment can be then achieved by adjusting the voltage of the tip-tilt piezo mirror in order to overlap the spot with the tip shadow (Fig. 4.7(b)). Once this step is completed an AFM/CFM scan is launched, which outputs the AFM channels and an additional PL map. In order to obtain a fine aligment, the spatial distribution of the nanodiamonds (Fig. 4.8(a)) is compared to the distribution of emitter in the PL map (Fig. 4.8(b)) to find a matching pattern. If the coarse alignment step has been performed correctly, the mismatch between AFM and PL is typically of the

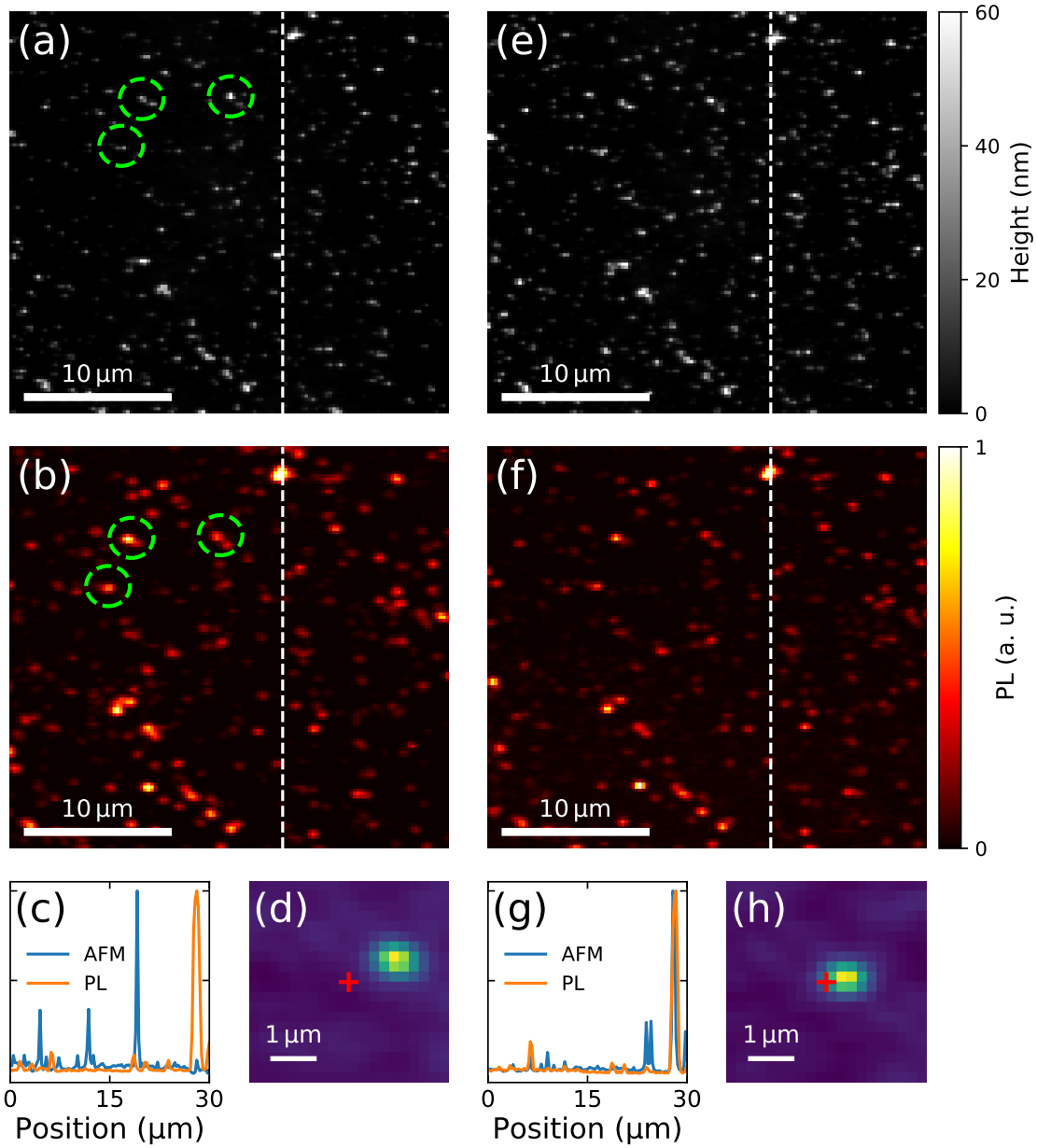

Figure 4.8: Alignment of the AFM/CFM scans. After coarse alignment, the combined AFM (a) and PL (b) maps typically look as shown in the panels. The line cut of the two plots (c), taken along the dashed line, stresses that there is a shift of $\sim 1.1\,\mu$m between the AFM and the CFM maps, as shown by their cross-correlation (d), where the red cross marks the origin of the map. However, patterns are recognisable, highlighted by the green circles. The PL spots can be correlated with the nanodiamonds positions. After moving to a diamond and optimising on its corresponding PL spot, the AFM (e) and CFM (f) maps are overlapped. The line cut along the white dashed line (f) shows that now the two maps more similar, with the (h) cross-correlation indicating a shift of $\sim 240\,$nm.

order of $1.1\,\mu$m(Fig. 4.8(c,d)). Once the nanodiamond which is the source of the emission is identified, the AFM tip is positioned over it. A PL map is then retaken and the signal is optimised on the chosen PL spot. The AFM/CFM maps then

overlap (Fig. 4.8(e,f)) with a mismatch of $\sim 200\,\mathrm{nm}$ (Fig. 4.8(g,h)) or less, if more precision is required.

4.4 Nanodiamond grafting and measurements on magnetic particles

Part of the experiments described here rely on grafting nanodiamonds to the tip of the AFM cantilever. In this configuration, the NV position is fixed with respect with the confocal axis, while the sample is scanned by the xy piezo stage. In this section I describe the strategy followed to identify and pick up nanodiamonds.

The first step consists in scanning the sample surface to identify emitters and control their properties. A suitable candidate for scanning magnetometry needs to be as bright as possible (typically the saturation count rate is $I_{sat} \approx 40\,\mathrm{kHz}$) and needs to contain a single NV –or many NVs pointing along the same crystalline axis– with good ODMR contrast ($\gtrsim 10\%$) and low strain splitting ($E \lesssim 5\,\mathrm{MHz}$). I verify this by inserting a small permanent magnet between the AFM head and the plate. If the observed dips are only two, I conclude that the NV is single. Alternatively, it can also mean that, if there is more than one NV centre, the axes all point in the same crystalline orientation. There is 25% probability of finding two NVs with the same orientation. Nonetheless, the high strain inhomogeneity in nanodiamonds usually lead to resolvable ODMR resonances, even if the NV axes have the same orientation. If the strain environment is homogeneous and the dips are not resolvable, CW-ODMR can be still performed if the resonance linewidth corresponds to the desired magnetic field sensitivity. The requirement for having strictly only a single NV applies only when performing coherent control of the spin state.

Once a candidate NV is selected, the next step is grafting it to the AFM tip. As described in the previous section, achieving an alignment between AFM and CFM images is essential, since the AFM/CFM images need to be overlapped also when small scans – of the order $\sim 300\,\mathrm{nm}$ – are taken. A typical grafting procedure is describe in Figure 4.10. A small scan of the area where the emitter is found is taken. If two nanodiamonds are found in the same area (Fig.4.9(a)) and are separated by less than the diffraction limit of the confocal microscope, the actual source of the emission needs to be identified. This is done by tracking simultaneously the AFM map and the PL map while pushing around the nanodiamond. If the fluorescent diamond is displaced, an immediate change occurs in the PL scan.

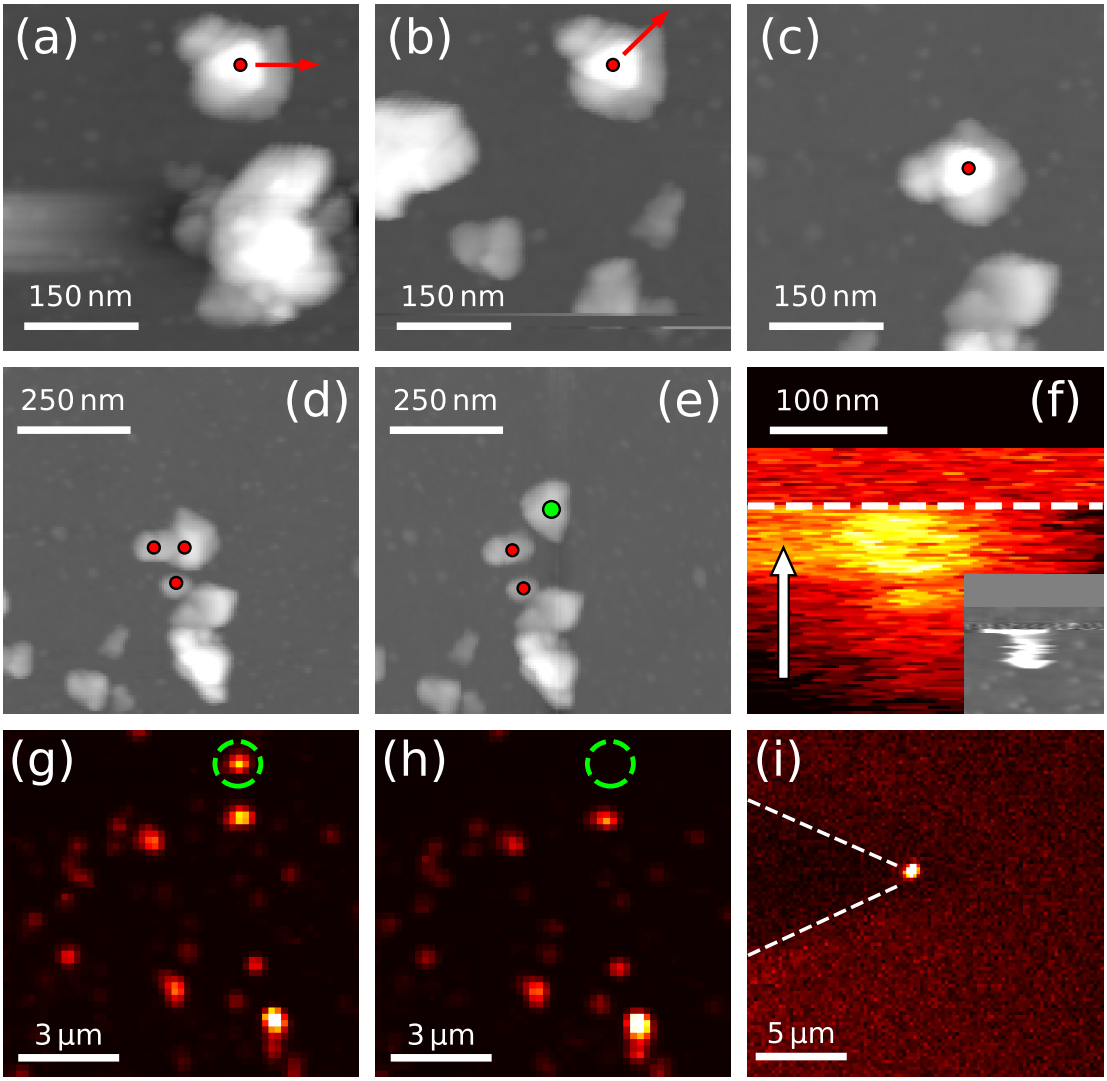

Figure 4.9: Tracking the motion of a nanodiamond and grafting to an AFM tip. (a) After having aligned the AFM with the confocal microscope, an area that contains a single NV centre is selected, as observed in the PL map. Two nanodiamonds are present and separated by less than the diffraction limit. By pushing one of the two nanodiamonds (marked by the red spot) in the direction indicated by the red arrow the PL signal is shifted. I move to the new position (b) and attempt to graft it, but the diamond is pushed to a new location (c). More grafting attempts (d) reveal that the nanodiamond is a nanodiamond cluster. (e) Moving the nanodiamond marked by the green dot shows a shift in the PL. (f) By repeatedly scanning over the NV (the white arrow indicates the slow axis direction) the PL suddenly becomes flat with constant brightness. At the same time the nanodiamond disappears from the topography map (inset). The PL map taken (g) before and (h) after the grafting, with the tip retracted, shows that the PL spot is no longer visible. (i) PL map of the nanodiamond grafted on the tip, when the latter is hovering $\sim 20\,\mu$m above the sample surface.

Once the nanodiamond is identified, I attempt to graft it on the AFM tip. I do this by modifying the scanning parameters. The mode of AFM operation (i.e. contact or tapping) has a strong influence over the process. I choose to operate in tapping mode, since contact mode tends to wear the tip more quickly and also displaces the nanodiamonds by larger distances when trying to push them or graft them. The crucial scanning parameters parameters are the scan speed, the PI feedback gains and the AFM setpoint. A successful strategy is lowering the setpoint while scanning over the nanodiamond. At the same time, I also change the proportional gain to slow down the feedback response or deactivate it entirely. Up to now, a deterministic strategy to select and graft a nanodiamond at the first attempt has not been found. A nanodiamond can be thus displaced while following this procedure (Fig. 4.9(c)).

It is also possible that a nanodiamond is actually a nanodiamond cluster. In this case, the grafting attempt can break up the cluster (Fig. 4.9(d)). In this case, I need to identify which nanocrystal is the fluorescence source (Fig. 4.9(e)). Tracking the PL of the emitter shows clearly when the nanodiamond adheres to the AFM tip (Fig. 4.9(f)). If the nanodiamond is on the surface, the PL has a Gaussian shape, which can be distorted if the nanodiamond moves while scanning. When it sticks to the tip, the recorded PL counts are constant and high (Fig. 4.9(f) above the white dashed line). This happens because the nanodiamond is now at rest in the confocal microscope reference frame. The topography (Fig. 4.9(f), inset) also shows that the nanodiamond disappears from the scan.

The comparison of the PL map measured before (Fig. 4.9(g)) and after the grafting, when the tip is retracted from the sample surface (Fig. 4.9(h)), shows that the emitter (highlighted by the green circle) is not on the surface any more. One can also check that the emitter is grafted to the tip by locating the tip of the cantilever with the confocal microscope and by taking a PL map of the area. A bright spot is visible at the very end of the tip, and its spectrum confirms that it is indeed an NV centre (Fig. 4.9(i)).

In order to verify the performance of the NV magnetometer, 20 nm-thick CoFeB/Pt nanoparticles are deposited on the surface of a glass slide (Fig. 4.10(a)). The thin films out of which these particles are made are magnetic with out-of-plane magnetic anisotropy. The magnetic nanoparticles are thus expected to have non-zero stray field only around the edges of the particles (see also Chapter 5). Scanning the NV over the magnetic particle shows a bright constant PL rate when the tip is scanning on glass, while an enhancement of the photoluminescence occurs when the edges of the particle are approached (Fig. 4.10(b)). The effect can be attributed to the

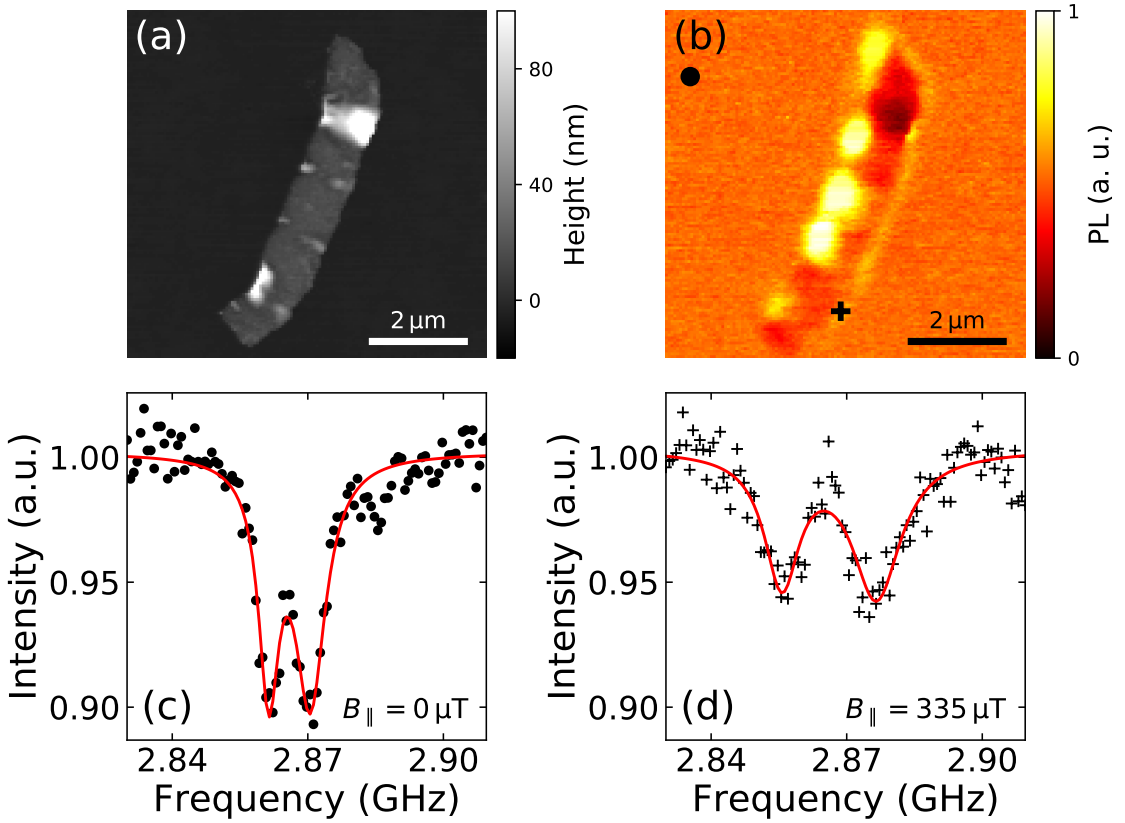

Figure 4.10: Thin CoFeB/Pt nanoparticles on quartz coverslips. (a) The topography of a magnetic nanoparticle and (b) the corresponding PL map, obtained by the scanning an AFM tip with a grafted nanodiamond. The ODMR spectrum is measured under the solid black dot in (c) and the one taken at the black cross at the edge of the particle in (d).

plasmonic coupling between a dipole emitter and the plasmon of the metallic surface [143]. The PL drop within the particle itself is only $\sim 4\%$, but is also strongly dependent on the imperfections on the material. The maximum PL observed drop is $\sim 70\%$, where the particle is thicker. The ODMR spectrum is also measured at a location far from the particle (black dot in Fig. 4.10(b)) and at its edge (black cross Fig. 4.10(b)). I show the respective spectra in Figure 4.10(c,d). The ODMR splitting far from the particle matches the NV response at zero-field on the glass slide measured before the grafting, whereas I observe a splitting corresponding to a magnetic field $B_\parallel \approx 335\,\mu$T. This confirms that the magnetism of the particles can be successfully detected using nanodiamonds grafted to an AFM tip.

The measurements described so far have been made using the AFM in "master mode", by feeding the APD signal into the AFM controller. This mode is suitable for nanodiamond grafting, since it allows for large, closed-loop scans which allow to move reliably to the same position each time a scan is repeated. However, as I have discussed in Section 4.3, this mode is not suitable for large magnetic field maps,

which require a long integration time on each pixel, of the order of few minutes.

4.5 Preliminary characterisation of an MFM tip stray field

In this section I discuss some of the preliminary measurements lead on the quantitative characterisation of the stray field of an MFM tip using NV centres. The interest in the precise characterisation of MFM magnetisation distribution arises from the complex task of interpreting MFM maps quantitatively. Commercial MFM tips are fabricated from silicon AFM cantilevers by coating them with a thin layer of magnetic material. The interaction between the magnetic coating can be used to generate images which can have a resolution as low as 20 nm [144]. However, tasks like the extraction of the full vectorial map of the magnetisation of a magnetic thin film are complex, because of the three-dimensional distribution of the tip magnetisation and the disturbance induced by the tip on the sample. The characterisation can be done using calibration samples and modelling the tip-sample forces through dipole-dipole interactions [145]. Alternatively, the tip stray field can be reconstructed using Lorentz electron microscopy [146, 147]. Here we explore an alternative approach that uses nanodiamonds on a glass slide to provide an in-situ measurement of an MFM tip stray field. While previous works with NV sensors showed the iso-B responses [48] of MFM tips or used them to perform AC imaging of its mechanical oscillation [148], there has been no systematic characterisation of the magnetic field with full ESR maps.

In this experiment we control the AFM scanning externally via the DAQ card analog voltages. The closed-loop operation is thus no longer available. We verify that the image distortion induced by the scanner hysteresis is negligible when $\sim 1\,\mu$m away from the scan edges and especially when the scan range is limited to few μm. We also need to modify the way a scan is operated. In the experiments where the scanning is performed by a nanodiamond grafted on the tip, the emitter is fixed with the confocal microscope axis. Hence, the confocal microscope needs only to compensate for slow alignment drifts which occur in the timescale of hours. However, the "sample" probed by the NV centres is an MFM tip. The probing NV needs to be scanned to form an image. At each pixel, the nanodiamond is moved to a new position. The scanning mirror below the confocal steps the beam position by the same amount and optimises on the fluorescence of the emitter. An ODMR sequence is then acquired.

The MFM tips we study (ASYMFMLM-R2, Asylum Research), are silicon cantilevers with a mechanical resonance at 75 kHz. The three-sided tip, with a radius of 20 ± 7 nm, is coated with ~ 15 nm of CoCr, with a nominal magnetic moment $M_t = 3 \times 10^{-17}\,\mathrm{Am}^2$. Figure 4.11(a) shows the topography scan of the area scanned with the MFM tip. The nanodiamond highlighted by the red circle contains an NV centre, which is the one tracked by the confocal microscope during the scan. The NV Zeeman splitting is shown in Figure 4.11(b). We observe a dipole-like pattern with two lobes where the stray field increases. In this case, one of the two lobes is much stronger than the other because of the relative orientation between the magnetic dipole and the NV centre. We also observe a splitting decrease in the middle of the main lobe. It is caused by topography of the nanodiamond containing the NV centre, which is ~ 130 nm-thick. When the tip is scanning over the nanodiamond, the separation between MFM tip and NV increases, leading to the observed Zeeman splitting reduction.

I fit the Zeeman splitting by modelling the tip stray field as a magnetic dipole:

$$\mathbf{B}(\mathbf{r}) = \frac{\mu_0 M_s}{4\pi}\left[\frac{\mathbf{r}(\mathbf{r}\cdot\hat{\mathbf{m}})}{|\mathbf{r}|^5} - \frac{\hat{\mathbf{m}}}{|\mathbf{r}|^3}\right] \tag{4.1}$$

where M_0 is the dipole strength, $\hat{\mathbf{m}}$ is the unit vector defining the magnetic dipole direction and $\mathbf{r} = (x - x_0, y - y_0, z_{topo} + d_{NV})$ is the position vector for a dipole centred at $\mathbf{r}_0 = (x_0, y_0, 0)$. z_{topo} is the experimentally-measured topography, while d_{NV} is a constant describing the separation between tip and surface. I then input the simulated field to a numerical model which solves the NV Hamiltonian for arbitrary fields. The model is used to perform least-squares minimisation on the experimental data, using M_s, x_0, y_0, d_{NV} and the dipole orientation as free parameters. The zero-field splitting shift and the Zeeman splitting produced by the fitted dipole field are shown in Figure 4.11(c,d), respectively. The topography contribution is removed. The shift induced by the magnetic field component orthogonal to the NV axis is of the order of 100 kHz. Although the fitted Zeeman splitting seems to have good agreement with the experimental data there are two caveats. The NV-to-sample distance estimated from the fit is $d_{NV} = 498 \pm 5$ nm. This is not compatible with the experimentally measured tip oscillation amplitude, which is ≈ 60 nm. The measured splitting also shows stray field "plumes" which extend away from the main lobes (Fig. 4.11(b)). The dipole model obtained from the fit does not have the same behaviour. Moreover, the total magnetic moment obtained from fit is $M_s = (1 \pm 0.5) \times 10^{-15}\,\mathrm{Am}^2$, which is two order of magnitudes larger than the nominal value.

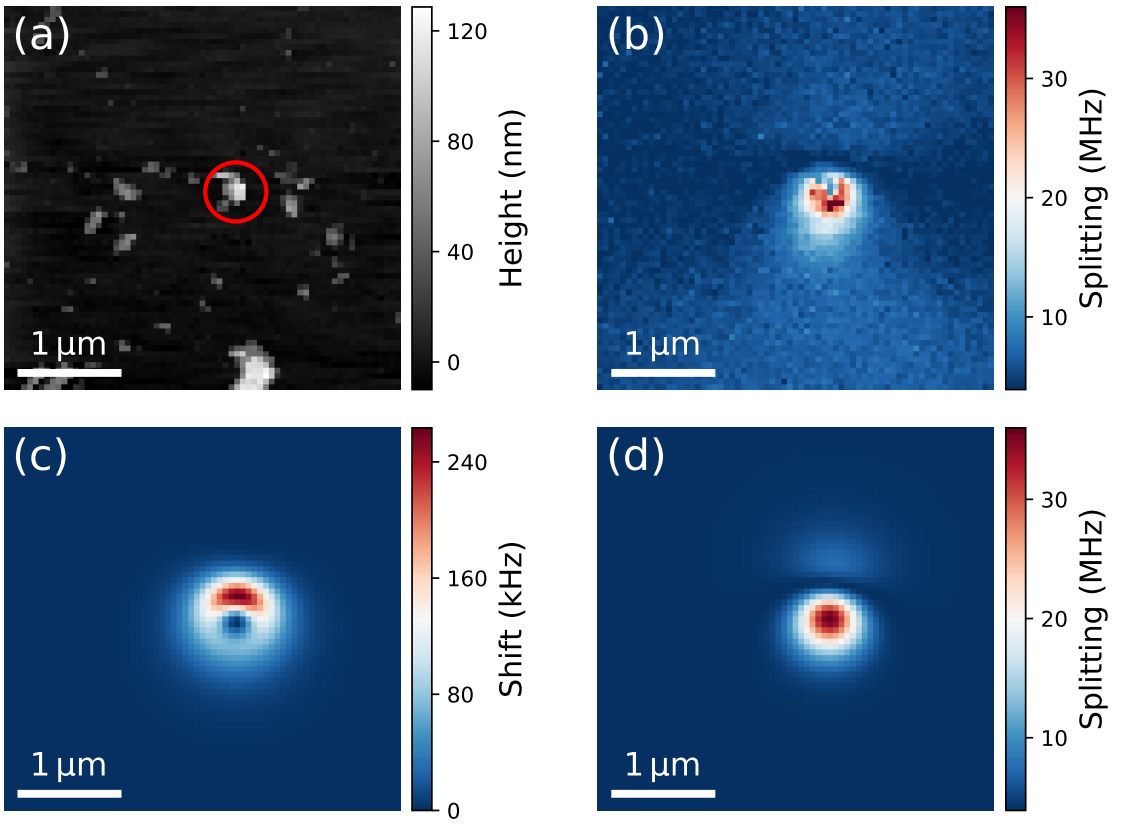

Figure 4.11: Stray field of an MFM tip. (a) Topography of the area scanned by the MFM tip. The nanodiamond in the centre of the figure, highlighted by the red circle, contains the NV used to measured the tip stray field. (b) ESR splitting of the NV, obtained from fitting the ODMR dips at each pixel. The reduced splitting in the middle of the lobe is due to the non-negligible size of the diamond, which increases the separation between tip and NV. (c-d) NV response to a magnetic dipole, with orientation and strength given by fitting (b). (c) shows the common shift of the resonances, caused by the magnetic field orthogonal to the NV axis and (d) is the Zeeman splitting due to the parallel component. Both plots are corrected for the sample topography.

The most likely explanation for the difference between the data and the fit results is the model incorrectness. Although a magnetic dipole is a good first-order approximation of an MFM tip stray field, it is not satisfactory when the separation between probe and tip is of the order of few tens of nm. A more suitable model is adding multipole terms to the stray field approximation and including the three-dimensional shape of the tip in the model.

4.6 Conclusions and outlook

In this chapter I have described the technical problems that had to be overcome to implement a scanning NV magnetometry experiment, along with some preliminary results that indicate the feasibility of the operation in the two possible experiment

configurations.

The most promising near-term measurement is the determination of the MFM tip magnetisation distribution. As discussed above, the tip model needs to be refined in order to include the three-dimensional tip shape. The measurement accuracy could also be improved by replacing NV centres in nanodiamonds with NV centres implanted in bulk diamond, thus removing the topography contribution to the measured stray fields.

The narrow space between AFM head and AFM plate does not easily accommodate for a vector magnet, which could be used both to apply a bias field to the NV centres or, more importantly, to measure the NV axis direction. Since the estimation of this quantity is crucial for quantitative magnetic field imaging, one could implement alternative ways to measure it, namely the NV polarisation-dependent fluorescence [149, 150]. The implementation of such a setup requires precise compensation of any ellipticity induced by the confocal optics to estimate the NV axis correctly.

The setup configuration is not the most suitable for scanning NV magnetometry. The lack of commercially available diamond tips containing implanted NVs for standard AFM cantilevers and the requirement of transparent samples puts a limit to the materials which can be studied. Alternatively, the setup could be transformed into a wide field NV imaging setup. In this configuration, a dense layer of NVs close to a diamond chip would probe the a material deposited over the diamond, while the AFM microscope could be used to induce local perturbations, for example by applying pressure, electric fields or magnetic fields.

Chapter 5

Imaging of magnetic thin films with an electrical readout AFM

The experiments described in the previous chapters rely either on drop-casted nanodiamonds, which can explore temperatures that range from room temperature to 4 K, or on nanodiamonds grafted to AFM tips to image 2D maps of magnetic fields. In this chapter, I am describing the realisation of a setup which combines both the NV/AFM imaging and the temperature tuning capabilities.

The results presented in this chapter were acquired in close collaboration with Anthony Tan, who also ran the mumax^3 simulations to obtain the stray fields used in the scanning NV simulations.

5.1 Setup description

The scanning imaging capability is given by a cryogenic-compatible atomic force microscope with optical access (attoAFM/CFM). Both sample and tip are controlled by two independent stacks, each consisting of a XYZ slip-stick positioners stack (ANPx51/LT, ANPx51/LT, ANPz51/LT) and a XYZ piezoelectric ceramic actuator scanner stack (ANSxyz50/LT) (Fig. 5.1(a)). This allows to align the AFM tip with the confocal microscope while using the other stack to explore different regions of the sample, or viceversa. The positioners are equipped with resistive position sensors, with a maximum travel range of 3 mm. Motion is achieved by supplying a sawtooth voltage wave, with typical peak-to-peak voltage and frequency ranging from 30 V and 100 Hz to 60 V and 400 Hz, depending on the AFM temperature and the desired motion speed. The scanners are open loop and scanning is achieved by supplying them with DC voltages from 0 V to 150 V. The radical difference from the setup described in Chapter 4 is the type of readout, i.e. electrical readout,

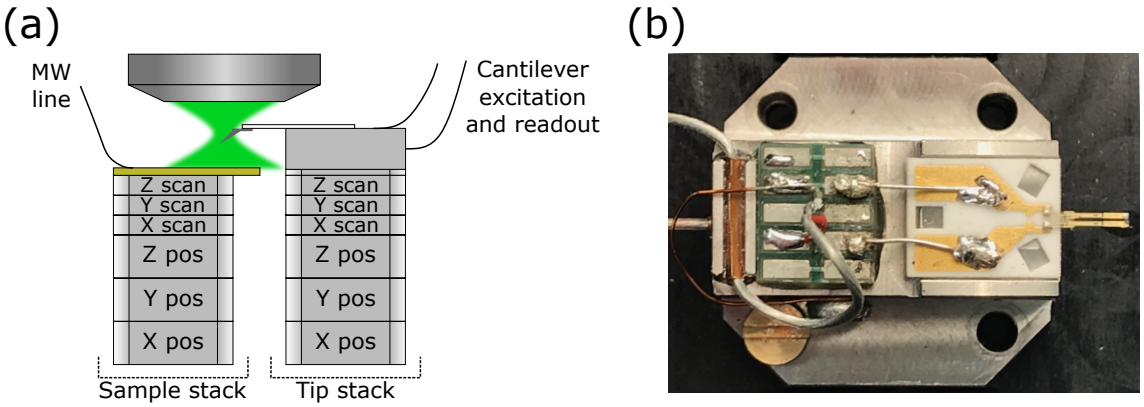

Figure 5.1: Electrical readout AFM schematics. (a) Two attocube stacks, with positioners and scanners, move the sample and the tip independently. A coaxial wire is connected to a custom PCB which is used as a sample holder. Two more wires provide the dither-piezo excitation and the tuning fork readout. (b) An electrical readout probe, mounted on the tip holder. The tuning fork is visible on the right side of the image.

and the type of probe required for it. The AFM silicon tip is glued across the two beams of a quartz tuning fork, which is mounted on a ceramic PCB (Fig. 5.1(b)). Two gold tracks are connected to the two beams respectively. When the tuning fork is excited, the mechanical oscillations of the beams compresses and stretches the silicon tip glued across them, creating a tapping motion. While this probe – known as Akiyama probe– can be self-actuating in its original design, the Attocube design uses an external piezo shaker to drive the tuning fork oscillations, soldered underneath the tip holder. The shaker oscillation frequency can be tuned to match the tuning fork resonance. The PCB tracks are used to pick up the electrical signal generated by the quartz oscillator. The signal is amplified by a low-noise amplifier (charge amplifier HQA-15M-10T, FEMTO) and read out by the AFM electronics. As stressed before, since the electrical signal is generated by the vibration of the quartz oscillator, the only AFM mode which can be used is tapping mode. The absence of optical beams that read out the cantilever oscillation also allows optical access from the top, which has two main advantages: the NV/AFM system can be used also with optically opaque samples; optical access is available also at cryogenic temperatures, when the AFM system is placed inside a cryostat.

Since both stacks have a z piezo scanner, the electronics can use either of the two to close the AFM feedback loop. For example, when the sample stack is the one that does the xy scanning, the sample z scanner is connected to the PI loop. If the sample needs to be kept at a fixed position, then the scanning and feedback is transferred to the tip stack.

The control electronics of the AFM system originally allow for the control of only one scanner set. However, scanning NV experiments require flexibility to move both

the sample and the tip independently. We thus decide to control the xy scanning using the $0 - 10\,\mathrm{V}$ analog outputs of a DAQ card. We then use the low-noise ($20\,\mu\mathrm{V}$ RMS) high-voltage (G = 20) amplifier (ANC250) which is supplied with the AFM system to control the sample xy scanners. We then use an additional amplifier from Thorlabs (MDT693B), with maximum gain $G = 15$ and 1.5 mV RMS noise, to control the tip xy position. The output noise of the amplifier is a fundamental parameter for the choice of the correct amplifier. At room temperature, the maximum scanner range is $30\,\mu\mathrm{m}$, which corresponds to a voltage of 60 V. An output noise of 1.5 mV RMS noise, for example, is converted into a position noise of 0.8 nm RMS.

Using the same approach described in Chapter 4, the control of the feedback z piezo is left to the electronics of the AFM controller. In the usual operation, the AFM tip contains an NV centre (Sec. 5.2). The feedback is thus off-loaded to the sample stack so that, once the tip position is optimised with respect to the confocal microscope, the position of the emitter is fixed.

The sample holder is a custom PCB with two conductive pads which can be screwed onto the sample stack. A picocoax cable with MMCX connector is connected to one end of the PCB, while on the other side the sample is glued. We pull a wire across the sample or we deposit a gold antenna on the sample itself and connect them to the PCB in order to deliver microwaves.

As mentioned above, the whole AFM is compatible with a closed-loop cryostat (attoDRY1000) with a base temperature of 2.8 K. The cryostat is equipped with a single-axis superconducting electromagnet which can generate a magnetic field up to 9 T.

Integration of the confocal microscope

The confocal microscope optics are arranged in the same schematics as described in Section 2.7. The optics are mounted on an optical breadboard which rests on top of the AFM insert. Since the scanning is entirely performed by the two scanning stacks, we do not use a scanning mirror. Depending on the temperature at which the experiment is run, we can select between two objective types. At room temperature, we can use an dry objective with NA = 0.9 and working distance $d_w = 1\,\mathrm{mm}$ (MPLFLN100x, Olympus), with limited chromatic aberration. The high numerical aperture ensures a high photon collection efficiency, 11%, larger than the other type of objective (with NA = 0.75) used in the previous experiments.

If the experiment is done at cryogenic temperature, a vacuum-compatible and cryogen-compatible objective is required. The objective has NA = 0.82 and $650\,\mu\mathrm{m}$

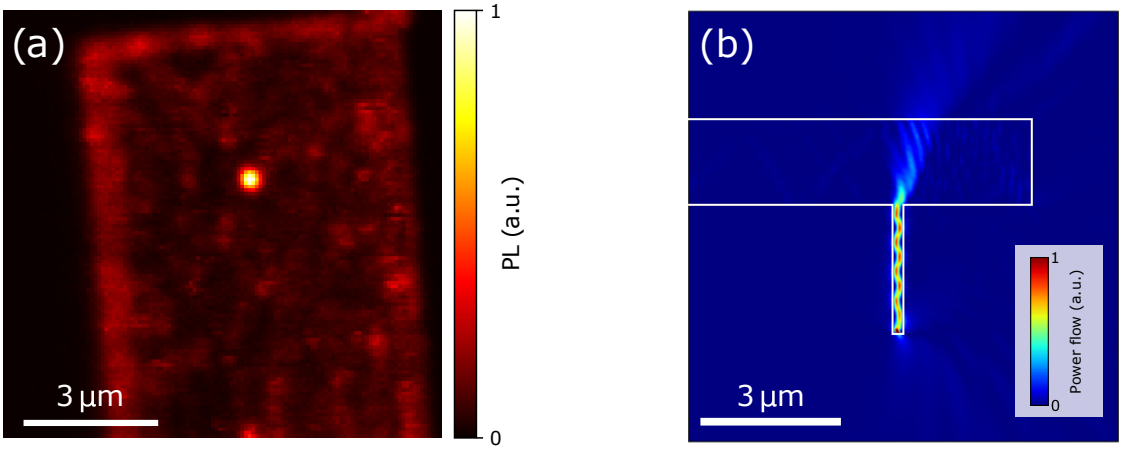

Figure 5.2: All-diamond probes for NV sensing. (a) PL map of a diamond probe. The whole diamond is weakly fluorescent, with a bright emission spot corresponding to the point where the pillar –and the NV centre– is located. (b) Normalised absolute value of the optical fluorescence intensity along the vertical direction of an NV centre inside a diamond tip. The simulation uses a single dipole radiating at a wavelength $\lambda = 637\,\text{nm}$, tilted 54.7° from the normal to the pillar surface, at 25 nm depth. The diamond refractive index is $n = 2.41$. The diamond tip is surrounded by air. The pillar in which the NV is implanted acts as a waveguide and concentrates the emission along the vertical direction.

working distance. The objective apochromatic range is between 570 nm and 790 nm. The chromatic shift between the excitation at 532 nm and the the NV ZPL at 637 nm is $\sim 2\,\mu$m. This requires additional alignment steps to achieve an overlap between the excitation and collection focal planes while at the same time maintaining an undistorted confocal spot. The smaller confocal distance also makes the alignment with diamond tips (Sec. 5.2) more complicated, since a small tip mounting error can prevent focusing on the diamond tip itself.

5.2 Diamond tips

Akiyama probes can be used for scanning NV magnetometry in the same way as an optical readout cantilever, by grafting a nanodiamond to the scanning tip. The method however is time consuming and unreliable especially when performing experiments at low temperature, since the thermal cycling might cause the detachment of the nanodiamond. The low fluorescence rate also requires a longer integration time, and full ESR imaging can take few days of measurement.

Another approach consists in using commercially available tips entirely made of diamond (Quantilever MX, QNami). A a diamond plate with (100) orientation is first mechanically polished and then etched with reactive ion etching (RIE) until reaching a thickness of around $6\,\mu$m. This step reduces the amount of structural de-

fects induced by the mechanical polishing. Nitrogen ions are subsequently implanted in the diamond, at an average depth which depends upon the implantation energy. The membrane is subsequently annealed at temperature above 800 °C. The annealing step allows the vacancies in the diamond lattice to migrate and "bond" to the nitrogen atoms, thus creating the NV defect. The implantation density influences the likelihood of finding single NV centres at a given site.

Following implantation, RIE is used to etch the diamond membrane to fabricate equally spaced diamond pillars, with a diameter of 200 nm and height of 3 μm. Statistically, few of the tips contain a single NV centre. The membrane around the pillar is further etched through in 20 μm $\times$ 5 μm rectangles. With the aid the of a micromanipulator, the diamond slab is glued to the tip of a quartz prong and detached from the diamond membrane. The prong is attached to the side of a quartz tuning fork beam, which comes free of the original silicon tip. Since the tuning fork is horizontal, as in the standard Akiyama probe configuration, the diamond tip does not have a tapping motion when the lowest energy vibrational mode of the tuning fork is excited. The tip instead oscillates left and right along the sample plane. This AFM mode is called as shear-force imaging.

An all-diamond tip has several advantages. First of all, the nominal depth of the NV is reproducibly small and can reach up to 10 nm without compromising the NV properties. The diamond pillar, which is primarily used as a scanning AFM tip, has also the effect of enhancing the collection efficiency of the PL. This is because the diamond pillar acts as a weak waveguide and focuses the emission of the NV centre in the vertical direction (Fig.5.2(b)). The high purity of the CVD-grown diamond also generally yields a narrower ODMR linewidth compared to NV centres in nanodiamonds, as mentioned previously. Because of the (100) of the diamond crystal, the NV centre's axis always subtends and angle $\alpha = 54.7°$ to the normal to the pillar facet –corresponding to an azimuthal angle of either $\vartheta = 54.7°$ or $\vartheta = 125.3°$– no matter along which of the four crystalline axes the defect points. As a downside, the directions along which the NV centre can probe the vector magnetic field are only four for the same reason, compared to nanodiamonds which can point in any direction.

Even though the implantation depth of the NV centre is shallow, the NV-to-sample distance is usually larger. A number of different mechanisms can affect it, such as the excitation amplitude, dirt accumulating on the tip, the planarity of the scanning probe with respect to the sample surface or just the simple presence of capping layers on the surface of the material, among others, leading to an observed NV-to-sample distance which is usually larger than the implantation depth. A good

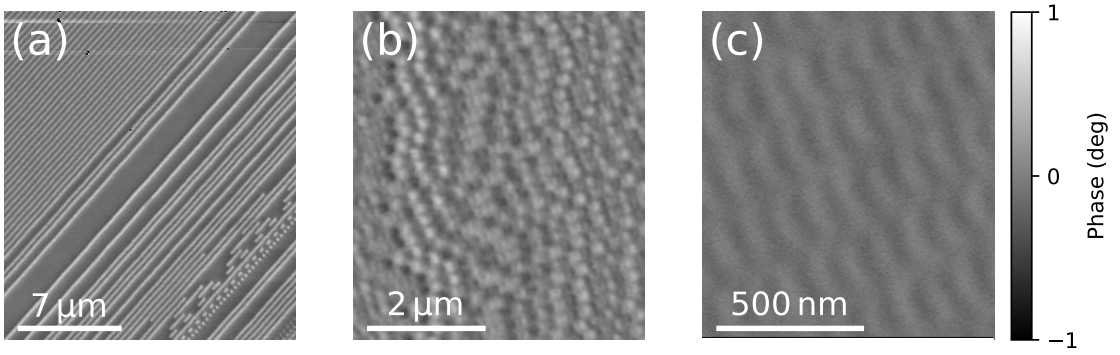

Figure 5.3: MFM imaging of a hard disk drive. Depending on the location, it is possible to observe (a) stripe bits, (b) square bits with a period of $\sim 250\,\text{nm}$ and (c) weakly magnetised bits with a period of $\sim 120\,\text{nm}$.

control of these contributions is thus essential to achieve high-resolution imaging, since the minimum resolvable feature size is approximately equal to the NV-to-sample distance.

5.3 Magnetic hard drive

The simplest way to check the performance of the NV/AFM setup is running measurements on a sample with a known behaviour and with a regular magnetic domain structure. We choose a hard disk drive (HDD), since it has regular magnetic bit patterns and also because there is literature [49, 50] that use scanning NV sensors on HDDs.

We first characterise the HDD samples using MFM. We attempt to image with standard MFM tips (ASYMFM-R2, Asylum research, $|\mathbf{m}| = 10^{-16}\,\text{Am}^2$). The stray

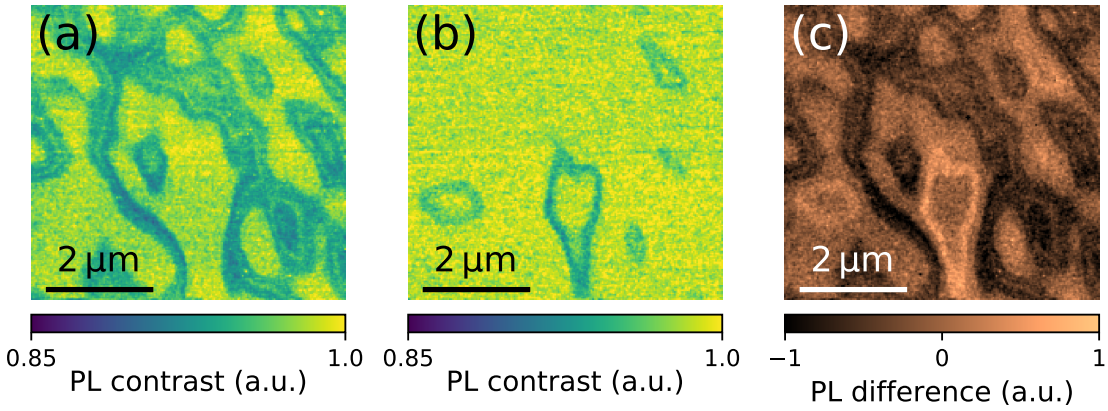

Figure 5.4: Iso-B imaging of HDD bits. Iso-B slices taken at (a) 2.876 GHz and (b) 2.891 GHz, and (c) the difference of the two signals.

field generated by the MFM tip however is too high and disturbs the magnetic ordering of the sample, leading to a domain pattern which appears to be random. We then choose to image the sample with a low moment tip (ASYMFMLM-R2, Asylum research, $|\mathbf{m}| = 10^{-17}\,\mathrm{Am}^2$). Depending on the sample location, we observe "stripe" bits, which consists of lines which are few tens of μm long and 300 nm wide, arranged periodically with 600 nm period (Fig. 5.3(a)). There are other extended regions which contain approximately square bits with lower magnetisation (as inferred from the MFM contrast) and finally other regions which contain rectangular bits which are 50 nm wide and have a 100 nm period.

Thanks to the extension of the regions, we can approximately position the NV centre in a desired area after mapping the HDD with the MFM, without further fabrication overheads. A 20 μm copper wire, pulled across the sample surface and soldered to the PCB, gives additional spatial reference. We first choose to position the NV on an area which contains the magnetic bits shown in Figure 5.3(b). We then measure the ODMR at 2 μm away from the surface –also to check the absence of stray fields at this lift height– and first decide to perform iso-B imaging of the surface. The two frequencies selected for iso-B are at 50% of the resonance dip ($\nu_1 = 2.876\,\mathrm{GHz}$), which corresponds to a stray field projection of 125 μT, and $\nu_2 = 2.891\,\mathrm{GHz}$, corresponding to 709 μT. I show the iso-B scan in Figure 5.4. At ν_1, there is a clear spatial dependence of the NV resonance. The smallest observed feature size is of the order 300 nm. At ν_2, the captured magnetic field variations are more sparse. At higher frequencies, I do not observe any spatial dependence, meaning that the stray fields at the NV site are not larger than $\approx 900\,\mu$T. For completeness, I also show the iso-B plot in Figure 5.4(c). The spatial variations I

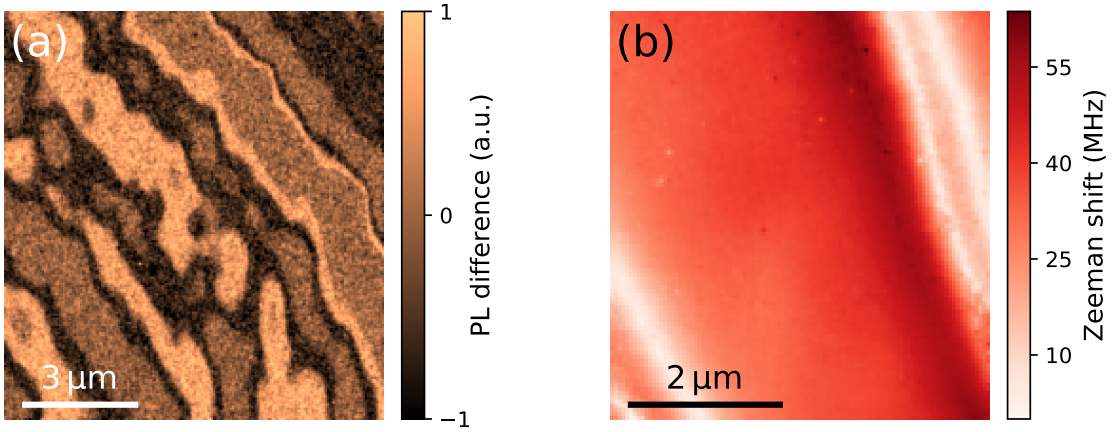

Figure 5.5: Imaging of stripe bits with an NV centre. (a) Iso-B image taken at 2.889 GHz and 2.896 MHz on a region containing magnetic stripes. (b) Zeeman shift of the NV levels on a different area containing stripe bits.

observe are not compatible with the periodicity of the square bits in Figure 5.3(b). The magnetic field intensity is also less than expected, since PL quenching imaging was observed with HDD bits in literature [49].

We repeat the iso-B imaging at another area which contains stripe bits (Fig. 5.5(a)). The iso-B image does not show features compatible with the periodicity of the stripes. Moreover, I observe that, while there is a clear signal directionality, given by the presence of magnetised stripes, the pattern is not uniform, especially in the middle of the scanned area. The interpretation of the patterns is made more difficult by the iso-B imaging. Indeed, while on one hand it provides fast imaging, the observed patterns can be misleading if the correct frequency slices are not selected.

For this reason, we run a full-ESR map of the stripe pattern at another location, using a new diamond tip. In order to improve the scan speed, we choose to record the ODMR spectrum above the zero-field splitting frequency, which is $\approx 2.87\,\mathrm{GHz}$. This is justified when the magnetic field are not strong enough to shift both resonances to higher frequencies (Sec. 2.2). I show the Zeeman shift obtained from the fit in Figure 5.5(b). The stray field in the scanned area has an average non-zero mean value of 34 MHz, which correspond to an average magnetic field projection of 1.21 mT. At the two corners of the scan, the shift decreases to $\approx 0\,\mathrm{MHz}$, showing two pairs of parallel lines. I do not observe feature length scales which are compatible with 300 nm-wide bits.

To gain further insight in the expect behaviour of the NV centre response on HDD, we numerically model the magnetic field generated by the bits. Current hard drive technology makes use of in-plane magnetic bits for storage. The pattern in Figure 5.3(b) is simulated using a grid of squares. Each square is then modelled as a uniformly magnetised domain, with magnetisation pointing randomly either in the $+y$ or $-y$ direction (in the image reference frame). Since the magnetisation $\mathbf{M}$ is uniform and static, such that $\boldsymbol{\nabla}\cdot\mathbf{M}=0$ and $\boldsymbol{\nabla}\times\mathbf{H}=0$, we can describe the bits as two parallel plates of opposite magnetic charges which are wide ($2w_x$) and tall ($2t$) as the bit width and thickness, respectively, and are separated by a distance equal to the length of the bit ($2w_y$). The stray field of single bit above its surface is [49]:

$$B_x = -\frac{\mu_0 M_s}{8\pi}\ln\left(\prod_{i,j,k=\pm1}\left(\frac{(z+kt)-\sqrt{(x+iw_x)^2+(y+jw_y)^2+(z+kt)^2}}{(z+kt)+\sqrt{(x+iw_x)^2+(y+jw_y)^2+(z+kt)^2}}\right)^{ijk}\right) \tag{5.1}$$

$$B_y = -\frac{\mu_0 M_s}{4\pi} \sum_{i,j,k=\pm 1} ijk \,\mathrm{atan}\left(\frac{(x+iw_x)(z+kt)}{(y+jw_y)\sqrt{(x+iw_x)^2+(y+jw_y)^2+(z+kt)^2}} \right) \tag{5.2}$$

$$B_z = -\frac{\mu_0 M_s}{8\pi} \ln\left(\prod_{i,j,k=\pm 1} \left(\frac{(x+iw_x)-\sqrt{(x+iw_x)^2+(y+jw_y)^2+(z+kt)^2}}{(x+iw_x)+\sqrt{(x+iw_x)^2+(y+jw_y)^2+(z+kt)^2}} \right)^{ijk} \right) \tag{5.3}$$

The total stray field at a given point (x, y, z) is given by the sum of the stray fields produced by each single bit in the grid. For square bits, we use $2w_x = 2w_y = 300\,\mathrm{nm}$. The stripes are instead generated using $w_y = 300\,\mathrm{nm}$ and $w_x \to \infty$. We use a value $2t = 10\,\mathrm{nm}$ for both bit tips, always according to [49]. The matrix of magnetic field vectors is input to a numerical simulation which solves the general NV Hamiltonian and returns the eigenfrequencies at arbitrary magnetic field orientations.

We first simulate an iso-B map on the square bit pattern for different NV-to-sample distances. The azimuthal and equatorial angles of the NVs are set to be $\theta = 54.7°$ and $\phi = 45°$. The iso-B map needs to take into account not only the resonant frequency of the NV but also of the resonance linewidth. The latter is extract from fitting the zero-field ODMR of the NV used to acquire Figure 5.4, together with the zero-field splitting and the strain splitting. The parameters are $\Delta\nu = 1.4\,\mathrm{MHz}$, $D = 2.871\,\mathrm{GHz}$ and $E = 3.9\,\mathrm{MHz}$, respectively. We then "probe" the simulated fluorescence at the 2.876 GHz and 2.891 GHz, the same frequencies used in the iso-B experiment.

I first show the response at an NV-to-sample distance $d_{NV} = 50\,\mathrm{nm}$ (Fig. 5.6(a)). The image shows that the bits outlines are visible, although the spatial resolution required to image them using iso-B is high, because of the steep stray field gradients. Overall, the NV response is qualitatively not compatible with what has been observed previously. At a height $d_{NV} = 400\,\mathrm{nm}$, the bits spatial features are not observable (Fig. 5.6(b)). What the simulations shows is slowly varying magnetic fields, with most of the signal confined at weaker magnetic fields (black lines), with only few areas which shift the NV into resonance with the second probe frequency. The simulation yields a result which is much closer to the observed behaviour, hinting towards an NV-to-sample distance which is much larger than expected. This would explain the weak magnetic fields sensed by the NV and the poor spatial resolution.

We run the same simulation on magnetic strip bits (Fig.5.6). The bits are repeated periodically along the vertical direction, alternating a magnetisation pointing upwards (within the plot plane) and a magnetisation pointing downwards. We use the periodicity of the tightly packed bits in Figure 5.3(a), i.e. 600 nm. The NV response at $d_{NV} = 50\,\mathrm{nm}$ shows that the signal has a periodicity of 300 nm (Fig.5.6(c)).

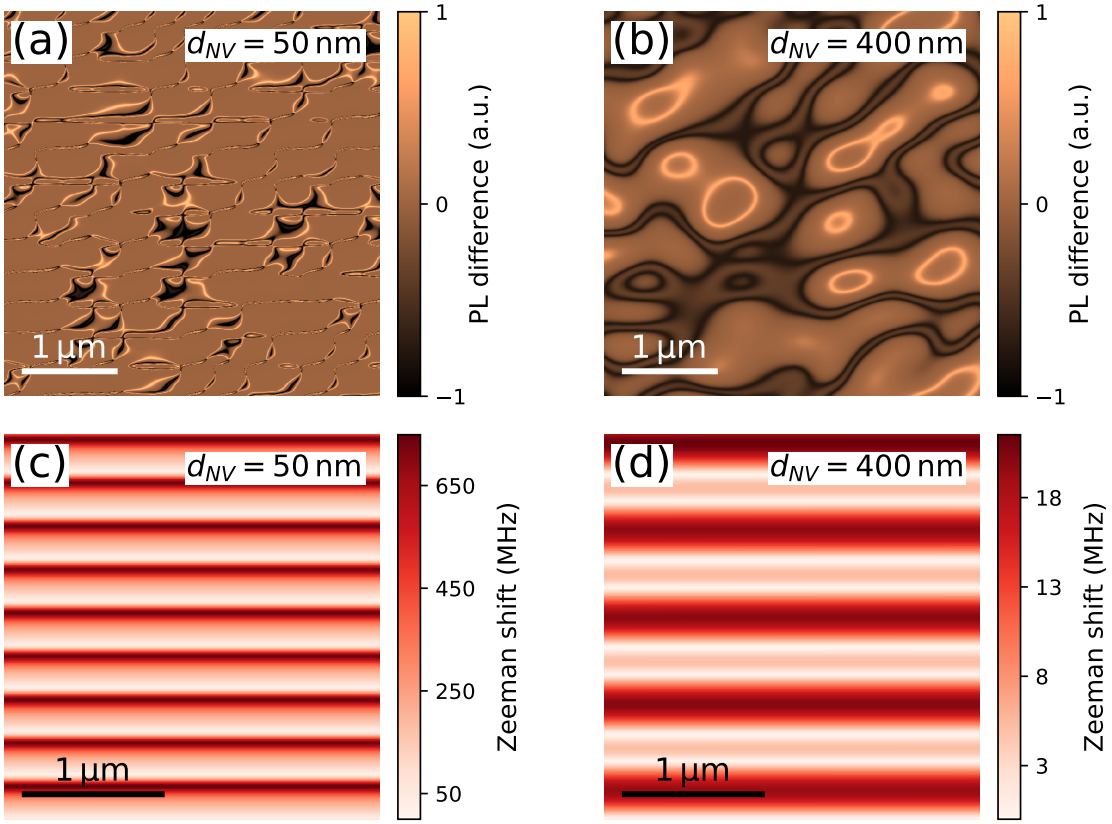

Figure 5.6: Simulation of the NV response on magnetic bits. (a) By generating a pattern of magnetic bits with randomly oriented in-plane magnetisation, we generate the three-dimensional stray field at different heights and xy positions. We then simulate the iso-B of the NV response at a height of 50 nm and (b) 400 nm. We repeat the simulation with stripe bits, with alternating in-plane magnetisation. The NV Zeeman shift at 50 nm and 400 nm is shown in (c) and (d), respectively.

The NV is unbiased, thus it effectively takes the modulus of the stray field, making down and up bits indistinguishable. We also notice that unlike magnetic domains with out-of-plane magnetisation, in-plane bits generate stray fields which are non-zero even when not in the regions proximal to a domain wall. The Zeeman shift spatial dependence at $d_{NV} = 400\,\text{nm}$ (Fig.5.6(d)) shows a periodicity which is approximately doubled compared to when the NV is close to the surface. At this distance, we notice that the Zeeman shift reaches a value close to 0 MHz along pairs of parallel lines, with a small Zeeman shift in between. This trend is qualitatively similar to the one in Figure 5.5(b). The between the line pairs can be explained by the fact that the NV is imaging an area where there is a larger spacing between two bits. The simulations on stripes also indicate that a large NV to sample distance, of the order of few hundreds of nm, is compatible with the measurements taken so far.

The results thus far hint on larger than expected NV-to-sample distance. How-

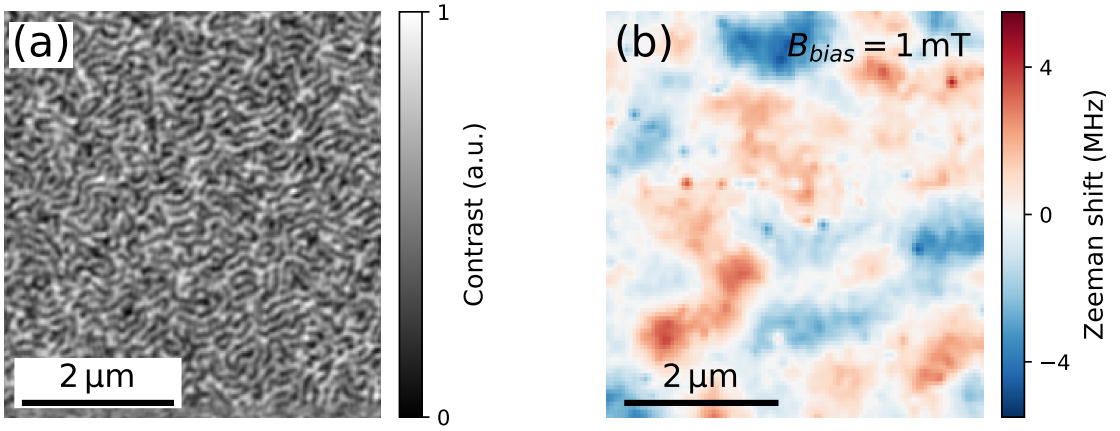

Figure 5.7: Imaging of magnetic domains of a Ir/Fe/Co/Pt multilayer. (a) MFM image of the sample, revealing meander domains with a domain width of 75 nm. (b) Scanning NV image of a different area but with the same width as (a), at a bias field $B_{\parallel} = 1$ mT. The maximum Zeeman shift corresponds to a stray field projection of 14 μT. The spatial variation of the stray field has a much larger length scale compared to the one of the domains detected with MFM.

ever, the number of unknowns in the sample, i.e. position of the NV with respect to a given bit pattern, the absolute value of the magnetisation and the presence of a capping layer, which increases the separation between the NV and the magnetic layer, or the accumulation of debris on the diamond tip prevents us from concluding with certainty that the tips are not performing correctly. We thus decide to image a Pt/Co/Fe/Ir magnetic multilayer (Sec. 5.5). The thin film displays out-of-plane magnetisation. We image the sample with MFM low-moment tips (Figure 5.7(a)), revealing that the magnetic domains are arranged in a meander-like structure. The width of the domains is ≈ 70 nm. The pattern can be observed consistently in different areas of the sample. The small size of the domains ensures that the pattern can be observed over the scale of few μm. We then proceed to image the stray field generated by the magnetic domains using scanning NV magnetometry. Using a new diamond tip, we first apply a bias field $B_{bias} = 1$ mT in order to make the NV more sensitive to external magnetic fields. We take a one-sided full-ESR map, using the same scanning range as the one used in the MFM images. The extracted signal (Fig. 5.7(b)) shows slow variations of the magnetic field, occuring over the distance of the order of 500 nm. The maximum shifts observed correspond to a stray field of only 14 μT. The image differs clearly from the one obtained using MFM, not only for the lack of clear stray field patterns but also for the weakness of the signal. The MFM image contrast indeed suggests that the NV centre, if close to the surface, should sense fields that are at least one order of magnitude larger.

None of the three tested tips seems to have an NV-to-sample distance which is compatible with the length scales of the imaged features, which is of the order of

100 nm or less. The lack of resolution does not allow us to extract any information about the magnetic samples, such as magnetisation pattern and stray field intensity. In order to understand the origin of these problems, we need to implement a way of measuring quantitatively the NV-to-sample distance.

5.4 Calibration of NV-sample distance

Quantitative measurements of the stray field direction from the NV Zeeman splitting can be obtained only if two parameters are known: the NV axis orientation and the NV-to-sample distance. In this section, I am going to explain the experimental techniques required to estimate these two quantities, and the result of the characterisation on different diamond tips.

5.4.1 Measurement of the NV axis

We first find the direction of the NV axis in the laboratory frame. We use a custom-designed vector magnet made of three pairs of Helmholtz coils. The coils are optimised for the operation with a computer-controlled three-channel power supply (2231A-30-3, Keithley), which can deliver a current of 3 A on each channel. The radius of the innermost coil is chosen to fit around the AFM insert. The coils can apply a maximum magnetic field $|B| = 3\,\mathrm{mT}$ and, using computer-controlled relays which can invert the power supply polarity, the direction can be rotated arbitrarily in the 3D space.

Since the maximum magnetic field we apply is weak, the NV energy levels are well described by the Hamiltonian in weak-field approximation (Sec. 2.2). We describe the magnetic field $\mathbf{B}$ and the unit vector $\hat{\mathbf{n}}_{NV}$ indicating the direction of the NV axis in polar coordinates. Hence, the Zeeman splitting of the NV reads:

$$\Delta\nu = 2\sqrt{\left(\frac{g\mu_B}{\hbar}\, B_{\parallel}\left(\vartheta, \varphi, \vartheta_{NV}, \varphi_{NV}\right)\right)^2 + E^2} \tag{5.4}$$

where the scalar product between magnetic field and NV axis reads as:

$$B_{\parallel}\left(\vartheta, \varphi, \vartheta_{NV}, \varphi_{NV}\right) = |\mathbf{B}|\left[\cos(\vartheta)\cos(\vartheta_{NV}) + \sin(\vartheta)\sin(\vartheta_{NV})\cos(\varphi - \varphi_{NV})\right] \tag{5.5}$$

The sequence to determine the NV axis is as follows. We first measure the ODMR with no applied bias field in order to measure the zero-field splitting and the strain splitting. We then fix the magnetic field at an azimuthal angle value and we sweep the equatorial angle. For convenience, we fix it so that the magnetic field vector

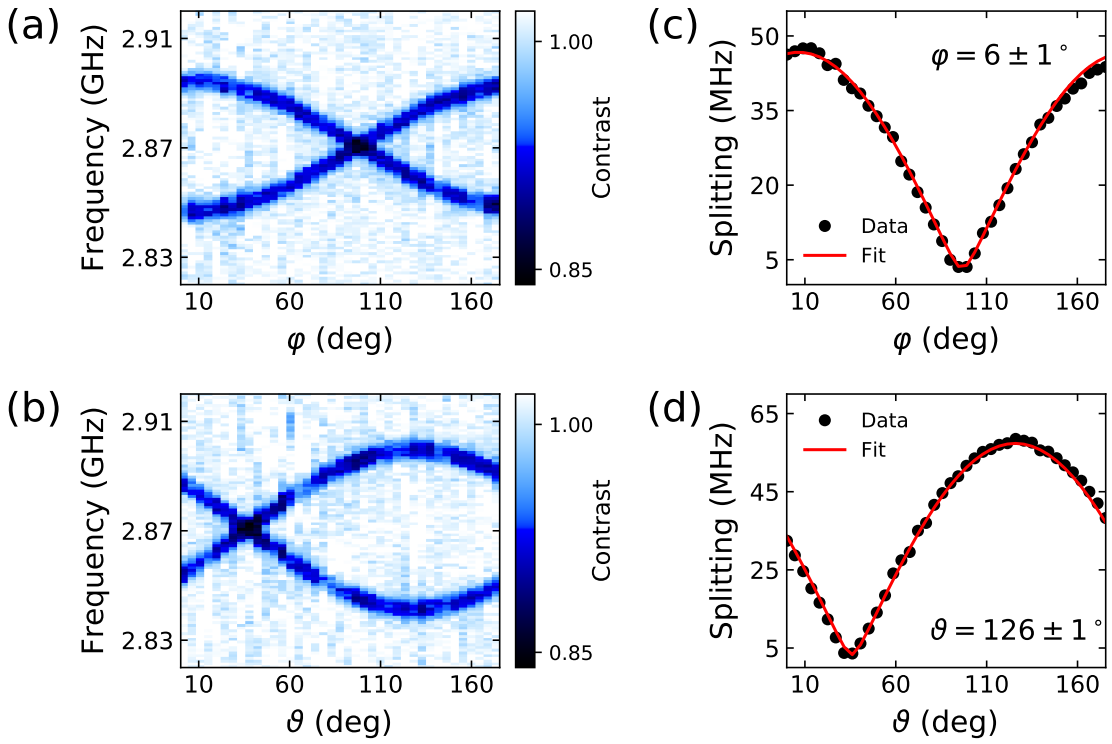

Figure 5.8: Measurement of the NV axis direction in the laboratory frame. Using a controlled magnetic field generated by a custom 3-axis Helmholtz coil system, we first apply a magnetic field at an azimuthal angle $\vartheta = \pi/2$. We then sweep (a) the equatorial angle φ and we record the the ODMR spectrum at each step. We then fix the equatorial angle at the value which gives the maximum splitting (b) and we sweep the azimuthal angle. Fitting simultaneously both datasets yields the NV direction in the lab frame (c, d).

lies on the equator of the vector magnet xy plane, thus $\vartheta = \pi/2$. In this case, the magnetic field projection is $\propto \cos(\varphi - \varphi_{NV})$. We acquire the ODMR spectrum at each value of the equatorial angle. The Zeeman splitting is maximum when $\varphi = \varphi_{NV}$ (Fig. 5.8(a)). We now repeat the process but this time we fix the equatorial angle and we sweep the azimuthal angle. Although, as above, the choice of equatorial angle does not affect the final measurement, we fix the equatorial angle so that $\varphi = \varphi_{NV}$ and $B_{\parallel} \propto \cos(\vartheta - \vartheta_{NV})$. The splitting is maximised when $\vartheta = \vartheta_{NV}$ (Fig. 5.8(b)).

The ODMR spectra are fitted to obtain the Zeeman splitting. We then apply least-squares minimisation to the Zeeman splittings acquired in the two previous steps using Equation 5.5. The only free parameters are $(\vartheta_{NV}, \varphi_{NV})$ (Fig. 5.8(c,d)).

Since we are using diamond tips which have $(1, 0, 0)$ orientation, the determination of the NV axis consistently shows that the azimuthal angle of the NV axis forms a 54.7° angle with the z axis of the vector magnet, taking a value of either 54.7° or 125.3°. I also remark that we usually run the NV axis measurement using $\vartheta \in [0, \pi)$ and $\varphi \in [0, \pi)$, i.e. the magnetic field is swept within half of the solid

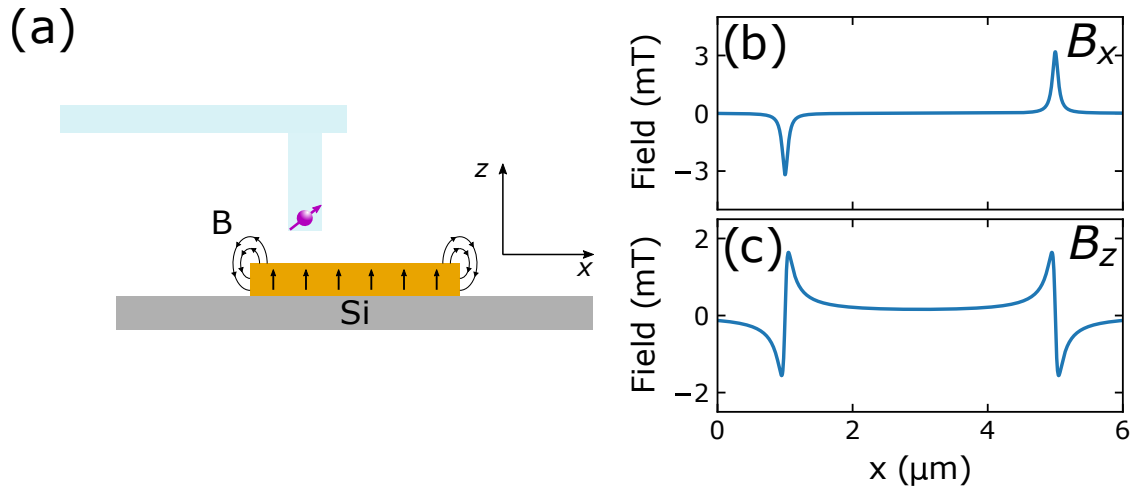

Figure 5.9: Stray field of strip for the determination of the NV-to-sample distance. (a) Scheme of the experiment. A tip containing an NV centre is scanned across a strip (along the x direction). The NV interacts with the stray fields produced by the strip with out-of-plane magnetic anisotropy. The stray field components $B_x(x, z)$ and $B_z(x, z)$, shown in (b) and (c), have been simulated using Equation 5.7, with $I_s = 8 \times 10^6$ A, $z = 50$ nm. The left and right edge are at $x_L = 1\,\mu$m and $x_R = 5\,\mu$m.

angle shell. The ODMR traces would be symmetrical in the other half of the sphere.

5.4.2 Determination of the NV-to-sample distance

Knowing the NV axis orientation allows to determine the direction of the stray field projection in the laboratory frame. This is important for quantitative imaging of the stray field, and hence also for the NV-to-sample distance determination. The method is based on the procedure devised by Hingant et al. [151].

We consider a strip of magnetic material which has infinite length along the y direction, a finite width along x and thickness t (Fig. 5.9(a)). The magnetisation of the strip is uniform and out-of-plane, and the fields are static. The strip thus behaves as a magnetic capacitor, with magnetic charges accumulating on the bottom and on the top surface of the strip. By analogy with an electric capacitor, the stray fields in the middle of the strip are approximately zero for a strip much larger than the height at which the fields are probed. The only stray fields arise at the edges of the strip (Fig. 5.9(b,c)). For the sake of simplicity, we focus on one of the two edges of the strip and we assume that the strip is large enough that we can neglect the contribution of the other edge to the total stray field. For a finite thickness t, the

stray field at a distance z from the midplane of the strip read as:

$$\begin{aligned} B_y(y,z) &= \frac{\mu_0}{4\pi} M_s \ln\left(\frac{y^2+\left(z+\frac{t}{2}\right)^2}{y^2+\left(z-\frac{t}{2}\right)^2}\right) \\ B_z(y,z) &= \frac{\mu_0}{2\pi} M_s \left[\operatorname{atan}\left(\frac{y}{z+\frac{t}{2}}\right) - \operatorname{atan}\left(\frac{y}{z-\frac{t}{2}}\right)\right] \end{aligned} \tag{5.6}$$

where we assume that $y = 0$ corresponds to the edge of the step.

Usually, the magnetic layer can be chosen to be thin, with a thickness of the order of 1 nm. The NV-to-sample distance usually is of the order of at least 10 nm. We can approximate Equation 5.6 by assuming that $z \gg t$. The expression for the stray fields thus simplifies to:

$$\begin{aligned} B_y(y,z) &= \frac{\mu_0}{2\pi} I_s \frac{z}{y^2+z^2} \\ B_z(y,z) &= \frac{\mu_0}{2\pi} I_s \frac{y}{y^2+z^2} \end{aligned} \tag{5.7}$$

where $I_s = M_s/t$ is the surface saturation magnetisation.

The two equations show that the linewidth of the magnetic response is proportional only to the distance z, while the intensity is proportional to the ratio I_s/z. In an experimental condition, z is replaced by a function of the topography measured by the scanning tip, so that $z \equiv f(y) + d_{NV}$. The model also needs to include potential shifts between the "topographic" edge and the "magnetic" edge. By knowing the direction of the NV centre (together with the zero-field splitting and the strain splitting), we can measure the Zeeman splitting of the NV across a strip and retrieve the NV-to-sample distance, together with the surface magnetisation I_s.

In practice, as mentioned above, the magnetic strip consists of a thin layer of ferromagnetic material deposited on a non-magnetic substrate, like silicon. The strips are usually over-etched, meaning that, while the magnetic material is thin, the step has good AFM contrast. The etching process is crucial to ensure that the calibration of the NV-to-sample distance is carried out correctly. If the parameters of the ion milling used to create the strips are not tuned correctly, this can lead to a significant redeposition of the etched materials on the edges of the strip, thus hindering the calibration procedure. Ideally, the strip topography is as sharp as possible, as shown in Figure 5.10(a). Using MFM scanning across the tip reveals the magnetic signal is uniform across few μm of the strip. When the diamond tip is scanned across the edge, the NV centre detects a linear combination of the two

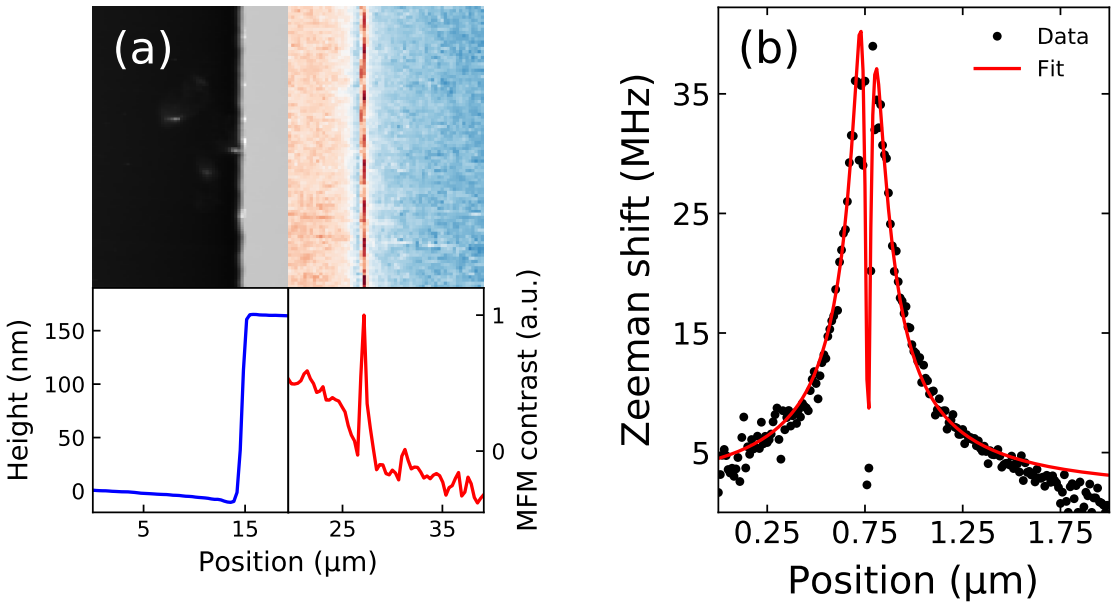

Figure 5.10: Calibration of the NV-to-sample distance. (a) The calibration sample consists of magnetic strips with out-of-plane magnetisation. In order to obtain a reliable calibration, the step needs to be as ideal as possible (left side of the image) and the strip needs to be uniformly magnetised (right side of the image). (b) Zeeman shift of the NV resonance as it is scanned across the magnetic strip. The sharp dip occurs at the edge of the strip. A fit where the NV axis direction is a fixed parameter returns both the surface magnetisation density of the material NV-to-sample distance. In this specific case, the estimated NV-to-sample distance is $d_{NV} = 50 \pm 1\,\text{nm}$.

stray field components, weighted by the azimuthal and equatorial angles of the NV in the laboratory frame. A typical NV trace over a magnetic edge is shown in Figure 5.10(b).

Although strips with out-of-plane magnetisation are relatively easy to fabricate and offer a reliable estimate the NV-to-sample distance, different structures can be used to achieve the same goal. In general, any stray field source with uniform magnetisation displays the same behaviour, where the width of the stray field variations depend only on the distance between source and probe and the peak magnetic field depends on both the saturation magnetisation and the NV-to-sample distance. An example of this is the magnetic field generated by a magnetic dipole.

Characterisation of diamond tips

We use the calibration procedure described above to characterize the performance of the diamond tips used in this work. The diamond tips used in the previous sections come from a batch of 5 tips, with nitrogen implantation energy of 18 keV, corresponding to a nominal NV depth of 25 ± 8 nm. The implantation depth however is not measured directly but only estimated using a software which simulates the

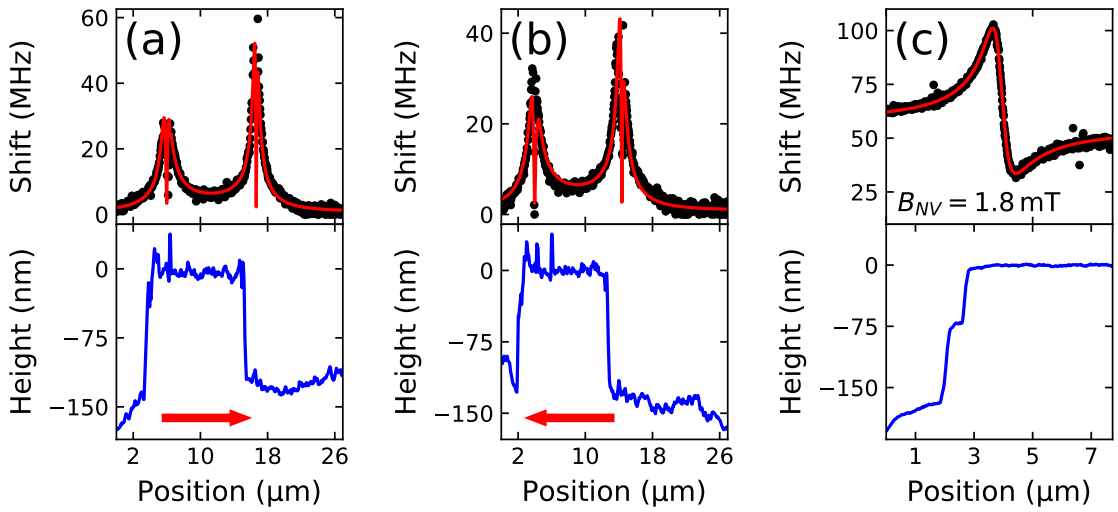

Figure 5.11: Characterisation of NV-to-sample distances d_{NV} for a batch of not performing tips. (a) Trace and (b) retrace ESR scans of the magnetic edge (the topography is shown in the lower plot). The scanning direction is shown by the red arrows. Both fits return $d_{NV} = 366 \pm 9\,\mathrm{nm}$ and $d_{NV} = 300 \pm 4\,\mathrm{nm}$, respectively. (c) ESR scan on one edge, applying a bias field $B_{NV} = 1.8\,\mathrm{mT}$. Applying a bias field allows to observe the change of the magnetic field sign.

implantation process at a given energy (srim.org). There are also other factors which influence the flying distance of the NV centre above the surface, for example the accumulation of debris on the tip, the angle between the tip and the sample surface or the AFM excitation amplitude/setpoint. The NV implantation depth thus marks only the lower limit to the minimum achievable NV-to-sample distance.

I show an example of the NV calibration curves in Figure 5.11(a), using the first batch of tips. The signal is acquired across the whole magnetic strip, scanning from left to right. The asymmetry of the ESR trace is not unexpected, being a manifestation of the rotation of the magnetic field at the two opposite edges. The fit yields a $d_{NV} = 366 \pm 9\,\mathrm{nm}$, much larger than the expected NV-to-sample distance. I also notice that there is a mismatch of $2\,\mu\mathrm{m}$ between the magnetic field sensed by the NV and the topography. While such a mismatch is not unlikely with NV centres in nanodiamonds grafted to a silicon tip, this behaviour is surprising for NVs in diamond tips, where the NV is within the scanning tip. The shift is not changed when reversing the direction of the scan (Fig. 5.11(b)).

The scans shown in Figure 5.11(a,b) are acquired without any bias field along the NV axis. The scan resolution is also limited by the scan size and the integration time per pixel required to achieve a good ODMR contrast. For this reason, we repeat the measurements by applying a bias field $B_{NV} = 1.8\,\mathrm{mT}$ and we focus on only one edge of the magnetic strip (Fig.5.11(c)). The ESR trace has a much higher resolution in this case and the presence of the bias field not only increases the sensitivity of the

NV to the stray fields, but also allows to observe its change in sign while crossing the edge. Also in this case, we still observe a shift of $\approx 2\,\mu$m between topography and magnetic signal.

In general, the fit results yield $d_{NV} > 300\,$nm for the first batch of tips (Table 5.1). The accumulation of debris on the tip does not seem the most likely explanation for this large NV-to-sample distances, since it is observed on all tips (Appendix C). Another possible explanation is the poor choice of AFM parameters, namely the excitation amplitude and feedback setpoint. In this set of experiments, we apply a bias field along the NV axis and we take an ESR trace on one of the two edges of the magnetic strip. Starting from an excitation amplitude which gives a signal of 100 mV, we systematically change the setpoint to 70%, 50% and 30% of the free oscillation amplitude voltage, until we reach 60 mV of free oscillation amplitude. We do not notice a significant difference between the ESR scan taken with 100 mV at 70% setpoint and the one taken at 60 mV at 30% setpoint, with a change in d_{NV} from $d_{NV} \approx 400\,$nm to $d_{NV} \approx 387\,$nm (Appendix C). We thus conclude that the AFM parameters are not critical to achieve a small NV-to-sample distance at least in the current conditions.

Following the same method, we characterise a new batch of tips obtained after discussions with the supplier. Although part of these tips could not be used for scanning NV experiments –one contained 3 NV centres and two had extremely unstable PL (Tab. 5.1)– we observed a much different behaviour. When we attempt to take ODMR spectra, the stray fields of the calibration strip are too strong and lead to both quenching of the photoluminescence and to the quenching of the ODMR contrast. Hence, we are not able to perform a quantitative characterisation of the NV-to-sample distance for this batch. However, all of the usable tips show PL quenching, also on the magnetic multilayers mentioned above (Sec. 5.3) and which will be the subject of the next section (Sec. 5.5). Quenching imaging was not observed with the previous batch of tips on the same samples. These results, combined with micromagnetics simulations, indicate that the NV-to-sample distance is smaller than the previous batch.

The acquisition of a new sample with weaker magnetisation – Ta / CoFeB(1 nm) / MgO / Ta with estimated $M_s = 1.2 \times 10^6\,$A/m– from the spintronics device research group in Nanyang Technological University [152] allows us to characterise tips which have a d_{NV} which is smaller than the tips of the first batch. Using this calibration sample, we verify that all the new tips have NV-to-sample distance $< 150\,$nm. Although such a distance is considerably smaller than 400 nm, it is still not sufficient to image the magnetic domains of the ferromagnetic multilayers

described in Sec. 5.5. Among all the tips measured, only one shows $d_{NV} = 55\,\text{nm}$, which is acceptable for the imaging of the aforementioned samples.

Overall, the majority of the characterised tips do not have a satisfactory NV-to-sample distance. Moreover, not all of the tips are suitable for NV magnetometry. Some of them become optically unstable after a period of time, hindering the capability of taking ODMR measurements. Two tips, while being optically stable, suddenly yielded erratic ODMR signal, which could be due to magnetic particles picked up by the diamond pillar while scanning a magnetic sample. One of the tips contained 3 NV centres. This implies that the process of finding a suitable probe for scanning NV magnetometry is not entirely deterministic yet and time consuming.

Batch	Tip code	d_{NV}
1st batch	FR03F4-3C19	Broke before cal. sample
	FR03-1JI	$\approx 400\,\text{nm}$
	FR03-1P12	$293 \pm 6\,\text{nm}$
	FR03-1T8	$400 \pm 3\,\text{nm}$
2nd batch	FR03-1Q17	3 NV centres
	FR03-2T3	Unstable PL
	FR03-2S4	Unstable PL
	FR03-1S14	NA
	FR03-1T20	NA
3rd batch	FR03-2Q3	$109 \pm 2\,\text{nm}$
	FR03-1O19	$151 \pm 3\,\text{nm}$
4th batch	FR0512-2H14	$55 \pm 3\,\text{nm}$
	FR0512-2R3	$141 \pm 3\,\text{nm}$
	FR0512-2Q17	$156 \pm 3\,\text{nm}$

Table 5.1: Characterisation of diamond probes. The tested tips from the first batch all show a NV-to-sample distance $\gtrsim 300\,\text{nm}$. The very first tip broke before the characterisation sample arrived. It is the one used to take the scans with poor resolution in Figs. 5.3, 5.7. The ODMR of the second tip disappeared after few measurements on the calibration strip, probably because of magnetic debris picked up during the scan. We infer the distance from the linewidth of the ESR scans. Although we could not measure directly the d_{NV} for the tips of the second batch, few of them showed quenching imaging on both the Ir/Fe/Co/Pt and the Co/Pt samples, indicating a $d_{NV} < 150\,\text{nm}$. The later batches have improved NV-to-sample distance, with $d_{NV} < 150\,\text{nm}$, although only one has an NV-to-sample distance small enough to image the domains in the magnetic multilayers shown in Figure 5.7.

5.5 Imaging of magnetic multilayers

As discussed in the previous section, the access to NV tips with small NV-to-sample distance is crucial to image the magnetic domains in magnetic films, such as the one we attempted to image in Fig. 5.7. In this section I am going to discuss the general physical properties of such multilayers and the results we obtained with diamond tips with $d_{NV} < 150\,\text{nm}$.

The magnetic multilayers, as the one presented in Section 5.3, have out-of-plane magnetisation and are arranged in meander domains at zero field. However, when a bias field is applied the meander domains transition into spin structures known as magnetic skyrmions. Skyrmions are winding spin textures which are topologically protected and thus are robust against film defects and temperature fluctuations. They arise in systems with broken inversion symmetry and in most cases are stabilised by the Dzyalonshinksii-Moriya interaction (DMI), which favours a canted alignment between two neighbouring spins [153]. The topological nature of skyrmions promises topological protection and particle-like nature for ease of manipulation, and topological Hall Effect for efficient electrical read-out, making them attractive not only for fundamental physics studies but also for novel memory and computing technologies [154].

The thin films we investigate in this section are fabricated in Anjan Soumyanarayanan's group at the Institute of Materials Research and Engineering, Agency for Science, Technology ant Research (A*STAR) in Singapore. They are multilayers consisting of 14 repeats of Ir/Fe/Co/Pt [155] and Co/Pt stacks [156]. Both film types are grown on a Si/SiO_2 substrate on top of which a film of Pt is deposited, and they are capped by a layer of Pt. The presence of Ir/Fe layers in the first thin film adds the capability of tuning the skyrmion properties. The DMI of the Fe/Ir interface has opposite sign [157] to the Co/Pt one [158] and thus the two stacked interfaces with opposite DMI signs contribute to an overall effective DMI, which can be tuned by varying the stack composition.

While MFM can provide high-resolution imaging of these skyrmions, extracting the skyrmion helicity remains unachievable. Other magnetisation imaging methods, as Lorentz force microscopy, are sensitive to only one component of the magnetisation. NV centres can be employed to quantitatively image the stray field and thus retrieve the source magnetisation. The study of the magnetic domains in the absence of probe back-action is also useful to confirm whether the MFM distorts the domains or not.

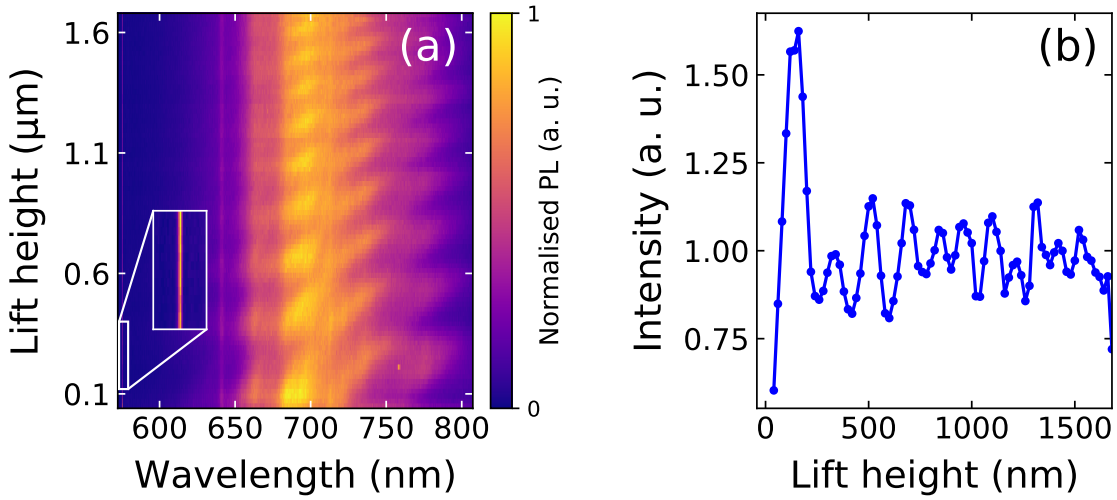

Figure 5.12: Lift height-dependent fluorescence. (a) Spectra of the NV centre as a function of AFM lift height from the sample surface, normalised by their respective numerically integrated fluorescence intensity. The inset highlights the diamond Raman line for an excitation of 532 nm. I observe a periodic modulation of the fluorescence intensity. (b) Fluorescence rate as a function of AFM lift height, obtained by integrating the un-normalised spectra in (a). Also in this case, I observe oscillations, with a period of ~ 200 nm. I attribute these oscillations to the interference effect between the dipole emitter and its image in the reflective metallic plane.

5.5.1 Lift height-dependent PL oscillations

Using tips coming from the second batch or greater ($d_{NV} < 300$ nm) we observe that while approaching the surface of the magnetic multilayers described above the NV PL shows oscillations increasing in amplitude on close approach to the sample surface.. The PL rate when the tip is contact with the surface is also modified –and usually reduced– from its out-of-contact value. Oscillations are not visible when contacting a glass surface or when using tips with $d_{NV} > 300$ nm.

We decide to investigate the origin of the oscillations by acquiring the NV spectrum of the NV centres at increasing lift heights. We also acquire two "control" spectra when the tip is not in contact before and after the measurement sequence, to verify that experimental drifts such as laser power or misalignment do not influence the measurements. I show the spectra in Figure 5.12(a), normalised for the total power at each lift height step. The plot shows a periodic modulation of the NV fluorescence spectra as a function of lift height. The modulation is more apparent looking at the phonon sideband, where a jigsaw pattern is visible. In Figure 5.12(b) I show the normalised NV fluorescence extracted from the spectra by integrating the total counts recorded by the spectrometer. The plot matches the typical counts oscillations observed while approaching the sample, with becoming more and more pronounced when in proximity with the sample.

The count oscillations have been previously recorded with all-diamond probes in the seminal paper by Maletinsky *et al.* [50]. The quenching of the photoluminescence is attributed to the change of the optical dipole lifetime, which is induced by the modified optical density of states in the proximity of an interface [159]. The results are also confirmed by Comsol simulations, using a model geometry as the one shown in Figure 5.2(b), which yields oscillations of the NV spectrum which are qualitatively similar to the data presented in Figure 5.12. Both the theoretical model presented in [159] and the numerical simulations indicate that the period of the oscillations is constant, with only the oscillation contrast becoming increasingly small for a large NV-to-sample distance. The shorter oscillation period observed at the maximum lift height of the z scanner is attributed to the non-linearity of the piezo stage.

While the change of the local density of states affects the NV dipole emission, I argue that there is also a modulation of the laser excitation, due to a weak cavity formed by the diamond and the surface. This inferred from tracking the peak intensity of the Raman line of diamond for a 532 nm excitation (inset of Fig. 5.12(a)). The Raman line, which is a bulk scattering effect, also shows a periodic modulation with lift height. This might suggest that standing wave interference of the laser excitation, a high visibility effect, may also be a source of residual oscillations.

5.5.2 Quenching imaging of magnetic domains

We first characterise the magnetic multilayers using MFM. In both multilayers, the domains are arranged in a maze-like pattern (Fig. 5.13(a,b)). The main difference between the Ir/Fe/Co/Pt stack and the Co/Pt stack is the domain periodicity. We estimate it by computing the 2-dimensional discrete Fourier transform of the MFM images and by calculating the radial average of the Fourier transform, centred on zero. The signal peak which is observed in the radial average corresponds to the inverse of the domain period. Alternatively, the 2-dimensional autocorrelation of the MFM image can be used for the same purpose. The domains periodicity is 150 ± 2 nm for the Ir/Fe/Co/Pt sample and 447 ± 4 nm for the Co/Pt sample. The different domains periodicity is expected on the basis of an enhanced DMI due to a asymmetric stack structure of Ir/Fe/Co/Pt as compared to the symmetrical Co/Pt stack.

We study the magnetic ordering of the material using diamond tips. Once approached the sample, we attempt to measure ODMR spectra. However, no signal can be observed, even when the tip is in extremely close proximity with the microwave antenna. When we repeat the measurement at a distance of 2 μm from the sample surface, the ODMR dips are visible and have high contrast. The most

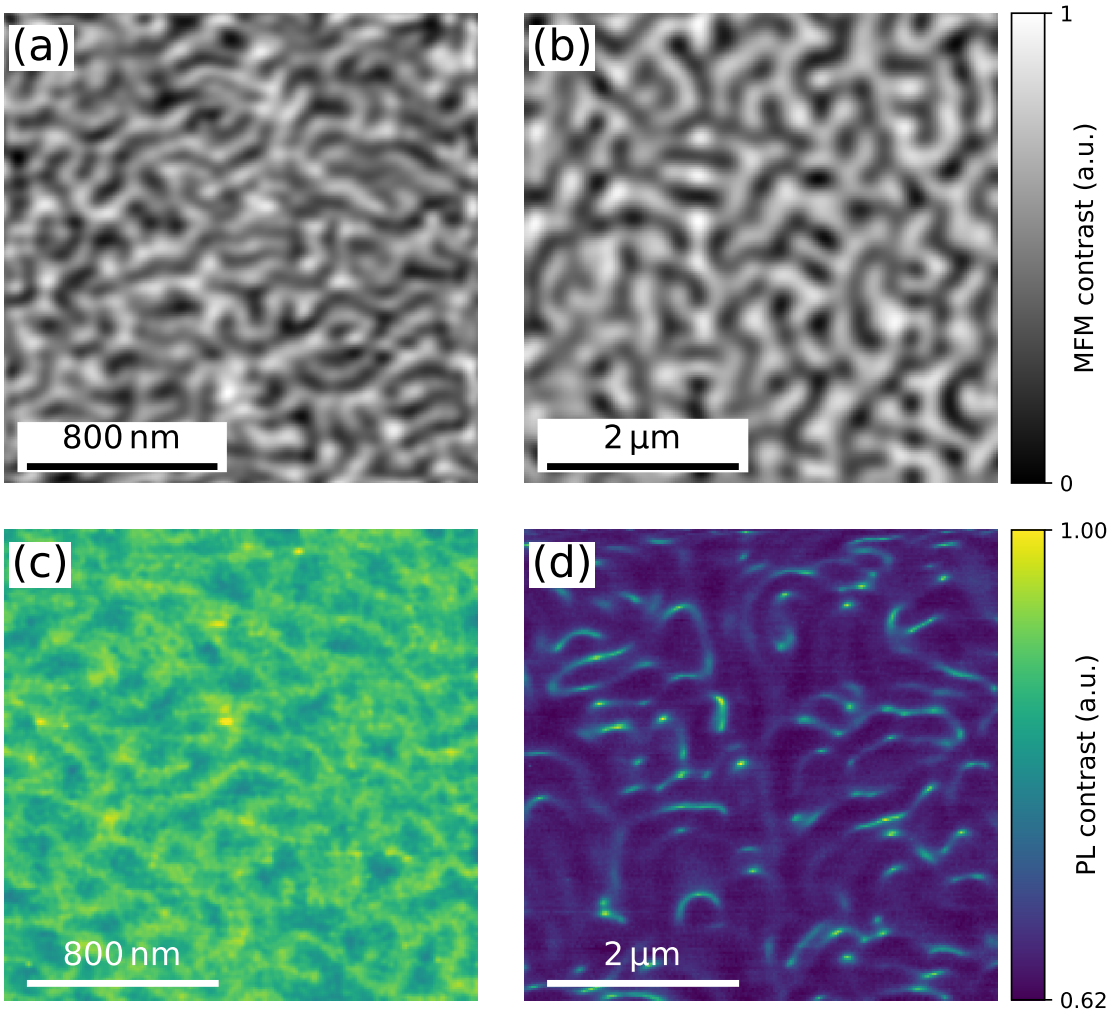

Figure 5.13: Imaging of Ir/Fe/Co/Pt and Co/Pt multilayers. MFM images of (a) 26M1 and (b) 26AA, which show meander domains with a period of 150 ± 2 nm and 447 ± 4 nm, respectively. (c,d) Scanning a diamond tip with small NV-to-sample distance shows clear signatures of photoluminescence quenching, caused by the strong stray fields of the samples. The estimated periodicity for (c) and (d) is 185 ± 4 nm and 460 ± 1 nm, respectively.

likely explanation for this effect is that the stray field generated by the multilayers is strong enough to quench the ODMR signal, as discussed in Chapter 2 (Sec. 2.6). Hence, we scan the sample while acquiring only the NV PL signal, using a software-based PID control to ensure a constant laser power during the scan. PL images from both scans (Fig.5.13(c,d)) show a clear quenching of the photoluminescence. The PL rate reduction – up to 38% for the Co/Pt stack– explains the absence of a detectable ODMR signal.

The quenching images show a domain periodicity which is different from the MFM scans shown above. I estimate the quenching image periodicity to be 185 ± 4 nm for the Ir/Fe/Co/Pt multilayer and 460 ± 1 nm for the Co/Pt. The discrep-

ancy of the domain periodicity between MFM images and quenching images is unexpected, even when taking into account the blurring of the stray field due to a non-negligible NV-to-sample distance. One possible explanation for such a discrepancy is the almost inexistent perturbation induced by the NV probe –especially for MW-free measurements– compared to the MFM measurements. On the other hand, we do not observe a considerable disturbance induced by the MFM tip, since we do not observe scars or displacement of the domains. Further investigation is needed to interpret the origin of the discrepancy. I also stress that using different tips the quenching image can vary. In particular, with one tip we observe a Co/Pt domain periodicity which is doubled compared to the image in Figure 5.13(d). The doubling of the periodicity is compatible with a larger NV-to-sample distance, highlighting the variability of d_{NV}.

Figure 5.13(c,d) show two types of quenching imaging. In Figure 5.13(c) the PL highlights the domains themselves, with bright and dark areas corresponding to the opposite directions of the out-of-plane magnetisations. The PL rate in Figure 5.13(d) is mostly reduced when the NV is scanning over the middle of a domain, and it recovers only at the domain boundaries. This effect is due to the smaller size of the Ir/Fe/Co/Pt domains compared to the Co/Pt domains. In the Ir/Fe/Co/Pt case, the NV-to-sample distance would need to be smaller than the average domain width in order for an image like Figure 5.13(d) to be observed.

Quenching imaging with a bias field

Photoluminescence quenching is the least ideal imaging mode of the NV centre, in the case where ODMR contrast is not detectable. The addition of an external bias field along the NV axis does not help reducing the ODMR contrast quenching. Even though a strong on-axis magnetic field coerces the total magnetic field –bias field plus sample stray field– closer to the NV axis, the norm of the total magnetic field is also larger than the one of the sole stray field. In Section 2.6 of Chapter 2 we show that the NV is more sensitive to small magnetic field misalignments at large magnetic field norms. This means that applying an on-axis bias field in the presence of a strong off-axis magnetic field further quenches the NV PL, meaning that the ODMR signal cannot be recovered.

Nonetheless, bias field can be used in combination with quenching imaging. We explore this using the Co/Pt sample, in the condition where the quenching highlights the domain boundary. We apply a bias field of $\approx 10\,\mathrm{mT}$ using a permanent magnet mounted on a rotation stage, in such a way that the rotation axis lies along the confocal optical axis. We then rotate the bias field in the sample xy plane to

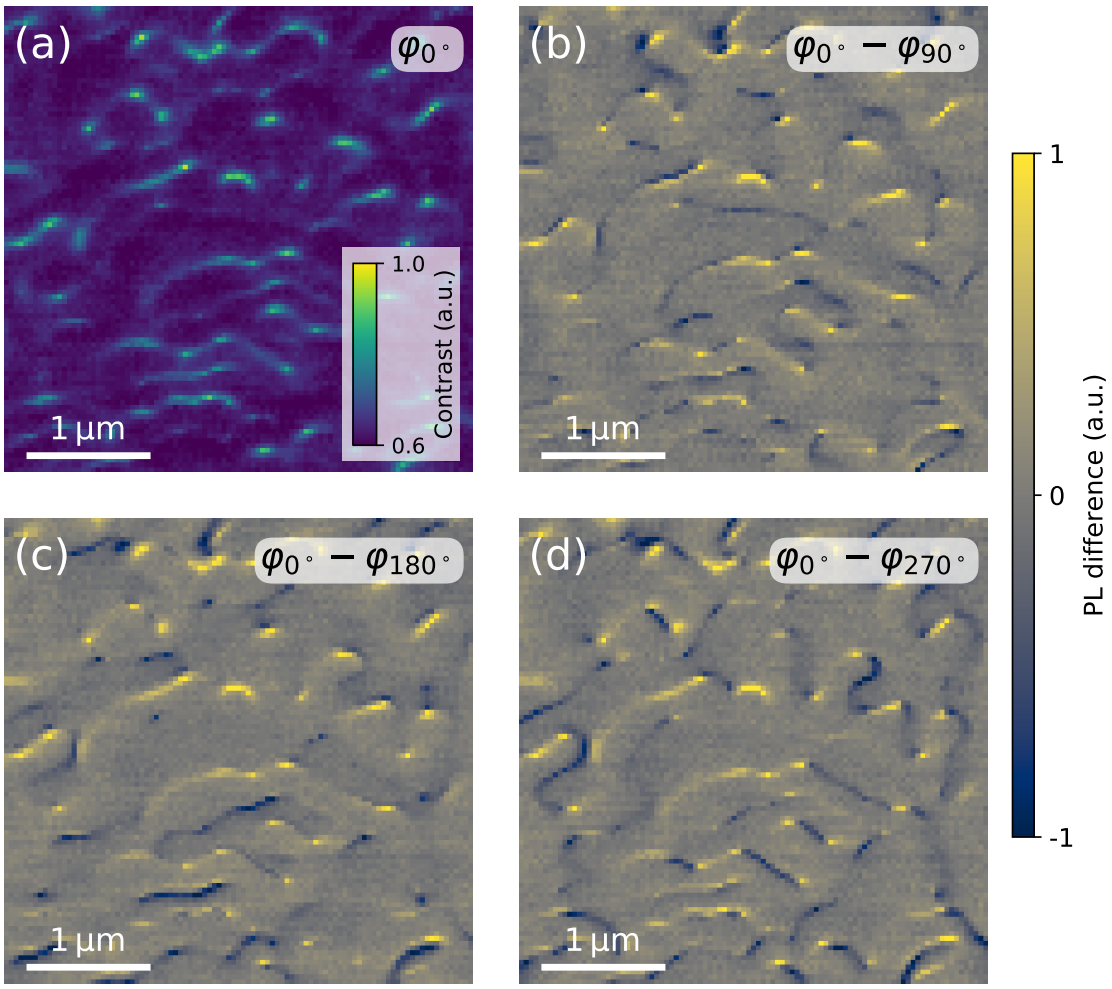

Figure 5.14: Quenching depending with an external magnetic field. (a) The quenching map is taken by applying a bias field with $|B| = 10\,\mathrm{mT}$ in the sample xy plane, oriented along the NV equatorial angle (φ_{0°). We then rotate the direction of the magnetic field within the xy plane, at 90° (φ_{90°), 180° (φ_{180°) and 270° (φ_{270°). The difference between the map at 0° and the maps at the three angles is plotted in panels (b-c), respectively. We observe that by applying the bias field at different angles we are able to highlight different portions of the domain walls.

four different equatorial angles –$\varphi = 0°, 90°, 180°, 270°$– relative to the NV axis equatorial angle. The quenching image $\mathrm{PL}(x, y, 0°)$ measured at $\varphi = 0°$, along with the maps of the difference $\mathrm{PL}(x, y, 0°) - \mathrm{PL}(x, y, \alpha)$ with $\alpha = 90°, 180°, 270°$, are presented in Figure 5.14. The rotation of the bias field highlights different parts of the domain boundaries which otherwise cannot be observed with a single scan.

We confirm the experimental results by taking an MFM scan on the Co/Pt multilayer, by extracting the domain pattern and by using it to simulate numerically the stray fields using micromagnetics simulations (Fig. 5.15). We can qualitatively replicate the results in Figure 5.14. The simulations also show that the directionality of the highlighted domain boundaries in the absence of a field is determined by the

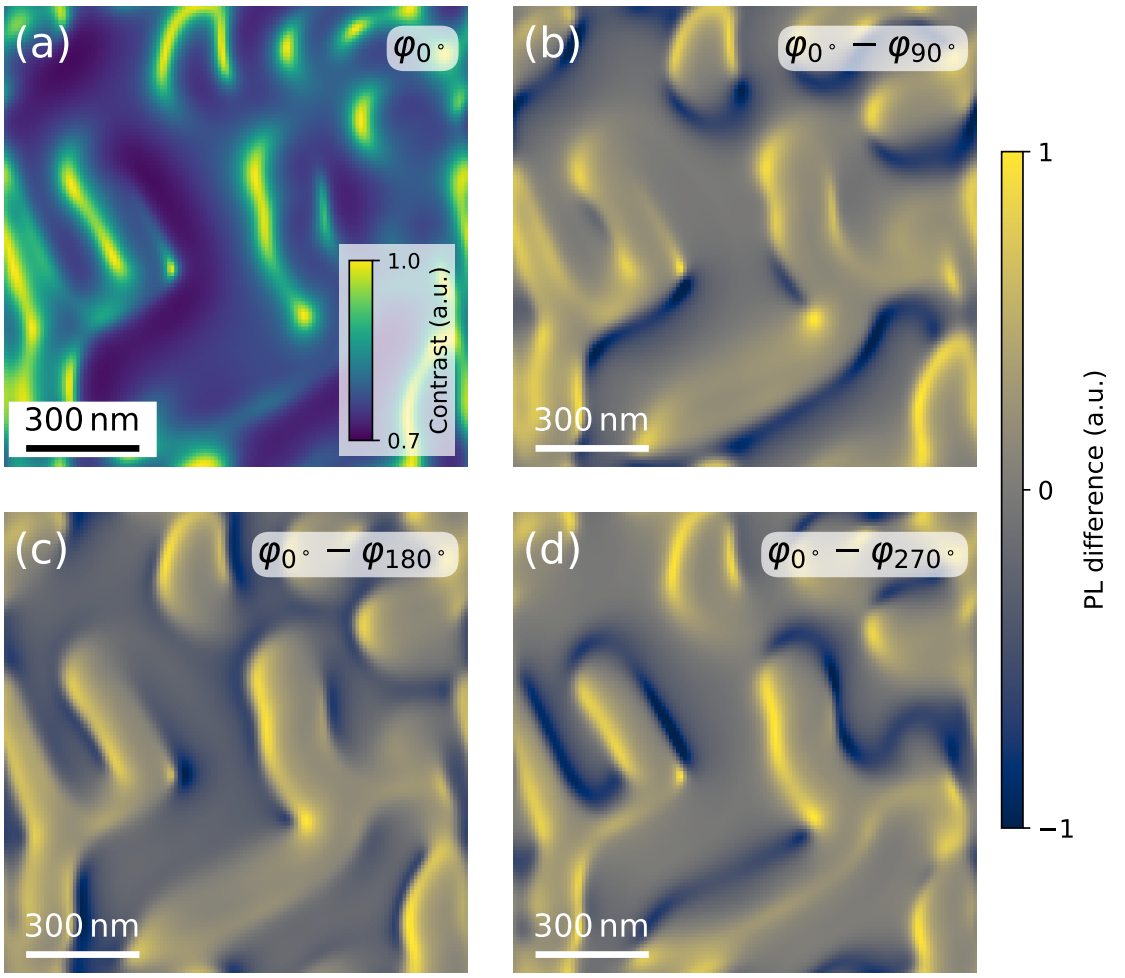

Figure 5.15: Simulation of quenching imaging as a function of an external magnetic field. We simulate the domain pattern starting from an MFM image. The domain boundaries and the magnetisation direction are the input of a micromagnetic simulator, which can return the stray field at variable distance from the surface. The parameters used in the simulation are $D = 2.87\,\mathrm{GHz}$, $E = 1\,\mathrm{MHz}$, $\vartheta_{NV} = 54.7°$, $\varphi_{NV} = 54.7°$, $d_{NV} = 70\,\mathrm{nm}$, $|B| = 10\,\mathrm{mT}$. We reproduce the experiment in Figure 5.14. We show the PL maps with the bias field along the NV equatorial axis in (a) and difference between this maps and the maps at 90°, 180°, 270° in panels (b-d), respectively.

direction of the NV axis with respect to the sample plane. The bright boundaries arise because of their preferential orientation, orthogonal to the NV axis equatorial angle.

5.6 On the magnetisation reconstruction

As mentioned throughout this work, one of the key aspects of NV magnetometry is the vectorial nature of the probe. A full ESR scan can build maps of the projection of the stray field along the NV axis. In principle, this information is sufficient to

obtain the other two components of the 3D magnetic field vector and to represent them in the sample reference frame. This is commonly obtained by imposing the magnetostatic condition ($\boldsymbol{\nabla} \times \mathbf{H} = 0$) and by assuming that the magnetisation $\mathbf{M}$ is planar and is uniform throughout the film thickness t ($\boldsymbol{\nabla} \times \mathbf{M} = 0$). Under these assumptions, the magnetic field is connected to the magnetisation by the relationship in the Fourier space $\mathbf{B}(\mathbf{k}, d_{NV}) = \mathbf{D}(\mathbf{k}, d_{NV})\mathbf{M}(\mathbf{k}, d_{NV})$, where $\mathbf{k} = (k_x, k_y)$ is the Fourier momentum in the sample (x, y) plane and:

$$\mathbf{D}(\mathbf{k}, d_{NV}) = \frac{\mu_0 M_s}{2}(e^{-d_{NV}|\mathbf{k}|} - e^{-d(d_{NV}+t)|\mathbf{k}|}) \begin{pmatrix} -\left(\frac{k_x}{|\mathbf{k}|}\right)^2 & -\frac{k_x k_y}{|\mathbf{k}|^2} & -i\frac{k_x}{|\mathbf{k}|} \\ -\frac{k_x k_y}{|\mathbf{k}|^2} & -\left(\frac{k_y}{|\mathbf{k}|}\right)^2 & -i\frac{k_y}{|\mathbf{k}|} \\ -i\frac{k_x}{|\mathbf{k}|} & -i\frac{k_y}{|\mathbf{k}|} & 1 \end{pmatrix}, \quad (5.8)$$

known as the dipolar tensor [160]. Since $\mathbf{D}(\mathbf{k}, d_{NV})$ has linearly dependent rows, the magnetic field can be reconstructed from a single component. Likewise, the magnetisation distribution can be reconstructed in a similar way. Another important consequence entailed by the form of the dipolar tensor is that the NV acts as a filter in the Fourier space and filters out components of $\mathbf{B}(\mathbf{k}, d_{NV})$ with $|\mathbf{k}| > 1/d_{NV}$.

In the case of a magnetic multilayer, the reconstruction of the magnetisation starting from an ODMR scan requires a thorough analysis. As mentioned above, the NV filters out part of the stray field components, leading to a first potential source of error in the magnetisation of the spin texture. Secondly, the NV is subject to the total stray field at a given point, given by the sum of the contributions of the single magnetised layers. If the magnetisation ceases to be uniform across the stack, the above assumptions are no longer valid and if used they could lead to an incorrect reconstruction. In this cases, NV magnetometry should be used in combination with other techniques, such as Lorentz force microscopy or XMCD.

5.7 Conclusions and outlook

In this chapter we have described the steps taken towards implementing a fully functional NV-AFM setup which can operate both at room and cryogenic temperatures. Using magnetic strips with out-of-plane magnetisation we characterised the NV-to-sample distances of commercial diamond tips containing implanted NV-centres, observing high variability of this value with few tips showing $d_{NV} > 300\,\text{nm}$. Using tips with $d_{NV} \lesssim 100\,\text{nm}$, we image the domains of magnetic multilayers using PL quenching imaging. We also notice that applying an external bias field allows us to map different portions of the magnetic domains boundaries.

NV-AFM with top optical readout offers plenty of potential applications ideal to study magnetism both at room temperature and at cryogenic temperature. The use of NV centres in diamond tips removes the need for the time-consuming nanodiamond grafting process, and at the same time it offers improved PL collection efficiency and spin coherence time, increasing the speed at which scans can be acquired. However, the difficulty in obtaining commercial tips with $d_{NV} < 100\,\text{nm}$, essential to image small magnetic domains, makes scanning NV magnetometry still partially reliant on chance.

The strong stray fields produced by the multilayers we studied in this chapter prevent us from taking full-ESR maps to enable quantitative magnetic field imaging. The PL quenching is expected to become even stronger when the domains are nucleated into skyrmions. Hence, full-ESR imaging requires both better microwave driving –so that the ODMR is still visible at weak (e.g. $\approx 15\%$) quenching– and the reduction of the multilayer repeats. Low-repeat multilayers cannot be imaged using MFM, so it is important to first ensure that the NV microscope performs correctly using multilayers with sufficient repeats that can be imaged by both MFM and full-ESR imaging.

Chapter 6

Conclusions and outlook

Much of the work described in this thesis has been devoted to the development of scanning magnetometry. In Chapter 3, I have described the precursor of scanning NV experiments, that is magnetometry based on NVs in nanodiamonds resting on the sample surface. The technique has been used to study the local magnetisation arising from PCMO/STO, at perovskite which becomes ferromagnetic at cryogenic temperatures, from 8 K to 130 K. The spatial variations of the stray fields detected by the NVs lead us to estimate a domain size of the order of μm. I also observe a strong dependence between the laser power and the NV Zeeman splitting when below the PCMO/STO Curie temperature, indicating that the optical power plays an important role in the magnetisation dynamics. Using the decoherence induced by the magnetisation fluctuation dynamics, we measure spatial variations of the magnetisation temperature ranging from 66 K to 96 K across a few μm. These measurements also show the limitations of drop-cast NVs as magnetometers to probe spin textures.

Chapter 4 describes the technical aspects of the implementation of a scanning NV magnetometer based on a commercial atomic force microscope with optical readout. Using an inverted confocal microscope, I devise a procedure to synchronize the topography maps taken by the AFM with the PL maps recorded by the confocal microscope. The procedure can be used to probe magnetic fields, as tested using magnetic nanoparticles. I also show preliminary results on the stray field characterisation of MFM tips, concluding that a simple magnetic dipole model is not sufficient to describe accurately what is measured by the NV.

In chapter 5 I present another scanning NV magnetometer, based on an electrical readout AFM which can operate from room temperature to below 3 K. The microscope can be operated using commercially available diamond tips which contain implanted NV centres. Preliminary magnetic images on hard disk drives show

inconsistent feature sizes between MFM and NV-AFM scans. Simulations of the NV response over such spin textures qualitatively show that the NV-to-sample distance is above 400 nm. We then experimentally characterise the NV to sample distance using strips with out-of-plane magnetisation. We observe NV-to-sample distances > 300 nm in four tips, while most of the tips characterised have $100\,\text{nm} < d_{NV} < 200\,\text{nm}$ and only one has $d_{NV} < 100$ nm. Such a distance is required to image meander domains in Ir/Fe/Co/Pt multilayers. We take quenching imaging maps on this sample and we observe a small discrepancy between the periodicity measured with MFM maps and the NV-AFM maps.

The results obtained with the two scanning NV setups are promising, indicating that only minor technical bottlenecks are to be solved. In particular, it is expected that once tips with small NV-to-sample distance are available, the cryo-compatible AFM will be ready to record high-resolution images, allowing for studies of the magnetic multilayers presented in Chapter 5. In the next paragraphs, I will describe some of the future research directions that can be undertaken.

As discussed in Chapter 5, the magnetic multilayers we studied can be nucleated into skyrmions. NV magnetometry in this case would enable a vectorial imaging of the skyrmion stray field and would allow to determine the magnetisation ordering. In this case, small NV-to-sample distances become crucial, since the skyrmion sizes are < 50 nm. At the same time, the magnetic fields created by the skyrmions can be extremely high and quenching imaging might be the only available imaging mode, as observed recently [161, 162]. For this reason, the skyrmion imaging will be performed on stacks with 3 repeats or less. This can done only after the one-to-one between MFM and NV-AFM images is established on stacks with more repeats. Another possible route is the imaging of antiferromagnetic skyrmions, which have been experimentally reported [163]. Consisting of skyrmions which are antiferromagnetically ordered along the thin film thickness, they are a promising alternative for even more efficient spintronic platforms, due to their predicted smaller size and greater mobility. Here NV centres have the potential to elucidate many features of skyrmion physics. If the stray fields generated by the skyrmions do not quench the ODMR, the NV can be used to obtain vectorial maps of the stray field and use it to determine the chirality of the skyrmions. Achieving the spatial mapping of the chirality is required to validate models of the interfacial DMI, thus explaining its link to the topological Hall effect. In the specific case of antiferromagnetic skyrmions, there is no direct evidence of that this coupling exists. NV centres can potentially be used to determine the validity of the models predicting antiferromagnetic skyrmions.

Following the first measurements on atomically thin graphene in 2004 [164], re-

search on two-dimensional materials has rapidly grown and has come to include a large class of materials. Among these, monolayers of CrI_3 have led to the first observation of 2D magnets [165]. Interestingly, the material switches from ferromagnetic to antiferromagnetic behaviour depending on the odd or even number of layers which make up the crystal [166], allowing for high control on the magnetic ordering. Recently, a 2D ferromagnet was imaged for the first time using scanning NV magnetometry [167]. The discovery of previously unobserved phenomena in carefully stacked monolayers, induced by the Moiré superlattice they form [168], has unlocked even more physics that could be explored. In particular, there has been a proposal for the realisation of skyrmion lattices in Van der Waals magnets using Moiré patterns [169], which have not been experimentally observed so far. Scanning NV magnetometry would allow a systematic study of the parameters that determine the ferromagnetic ground state, which can change from magnetic bubbles to skyrmion lattices, as well as the influence of the Moiré pattern on the stabilisation of such structures.

Another potentially interesting route lies in exploiting the potential of the NV to interact with its surrounding mesoscopic environment. By repeatedly polarising the NV spin and then by transferring its polarisation to the surrounding nuclear spins (like ^{13}C), nuclear spin hyperpolarisation can be achieved [170, 171]. If this scheme was feasible for diamond tips, it would be possible to realise a hyperpolarised mobile probe. This would be of particular interest if scanning NV magnetometry could be applied to biological samples, where spin-polarisation can be used to enhance the MRI contrast. It could be also applied to studies of polarisation transfer in solid state systems.

Appendix A

Details on the NV Hamiltonian and photodynamics

Analytical solution of the secular equation

The secular equation Eq. 2.9 can be solved using Cardano's method. The three eigenfrequencies are:

$$\nu_1 = \sqrt[3]{\rho - \frac{\lambda}{2}} - \sqrt[3]{\rho + \frac{\lambda}{2}} \tag{A.1}$$

$$\nu_2 = \xi \sqrt[3]{\rho - \frac{\lambda}{2}} - \xi^2 \sqrt[3]{\rho + \frac{\lambda}{2}} \tag{A.2}$$

$$\nu_3 = \xi^2 \sqrt[3]{\rho - \frac{\lambda}{2}} - \xi^4 \sqrt[3]{\rho + \frac{\lambda}{2}} \tag{A.3}$$

where:

$$\xi = -\frac{1 - i\sqrt{3}}{2} \tag{A.4}$$

The ρ coefficient is:

$$\rho = \sqrt{\frac{\lambda^2}{4} + \frac{\mu^3}{27}} \tag{A.5}$$

and:

$$\lambda = -\frac{D}{6}\left(\tilde{B}^2 + 4E^2\right) + \frac{2}{27}D^3 - \frac{\tilde{B}^2}{2}\left(D\cos(2\vartheta) + 2E\cos(2\varphi)\sin^2(\vartheta)\right) \tag{A.6}$$

$$\mu = -\left(\frac{D^2}{3} + \tilde{B} + E^2\right) \tag{A.7}$$

where D is the zero-field splitting, E is the off-axis strain splitting, ϑ and φ are the azimuthal and equatorial angle of the magnetic field (for an NV axis pointing along

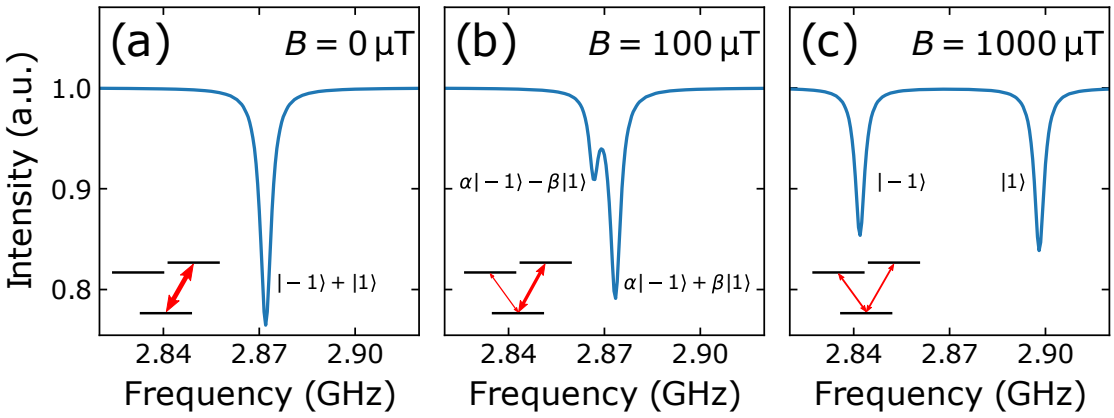

Figure A.1: Simulated response of the ODMR, for an NV with $D = 2.87\,\text{GHz}$ and $E = 2\,\text{MHz}$, with increasing on-axis bias field, with a linearly polarised MW excitation orthogonal to the NV axis. (a) In presence of strain, the transitions couple to linearly polarised MW excitation. (b) When a weak bias field, the reduction of the strain contribution causes the two transitions to couple to elliptically polarised MW. The linear excitation thus couples more strongly to one transition than the other, allowing us to see both transitions but with different contrast. (c) When the eigenstates are –almost– purely $|-1\rangle$ and $|+1\rangle$, the two transitions couple to σ^- and σ^+ polarised MW. Since the linearly polarised excitation can be written as a linear combination of circular polarisation, the ODMR shows two dips with equal contrast.

the $\hat{z}$ of the Cartesian coordinate frame), $\tilde{B} = \tilde{\gamma}|B|$, where $|B|$ is the norm of the magnetic field vector, $\tilde{\gamma} = \gamma/(2\pi)$, and γ is the electron gyromagnetic ratio.

Constraints on the secular equation solutions

As mentioned in Section 2.2.2, the coefficients of the secular equation (Eq. 2.9) are linked. The polynomial has the form $\lambda^3 + a\lambda + b = 0$, thus its roots ν_i satisfy the following system of equations:

$$\nu_1 + \nu_2 + \nu_3 = 0 \tag{A.8}$$

$$\nu_1\nu_2 + \nu_1\nu_3 + \nu_2\nu_3 = a \tag{A.9}$$

$$\nu_1\nu_2\nu_3 = b \tag{A.10}$$

which can be used to obtain Equation 2.11.

ODMR polarisation dependence

As stated in the main text, the MW excitation couples differently to the two ground state transitions, depending on the MW polarisation and on the eigenstates. I show an example of this in Figure A.1. I simulate the ground state Hamiltonian (with the addition of decoherence processes) and I add a linearly polarised MW excitation. By

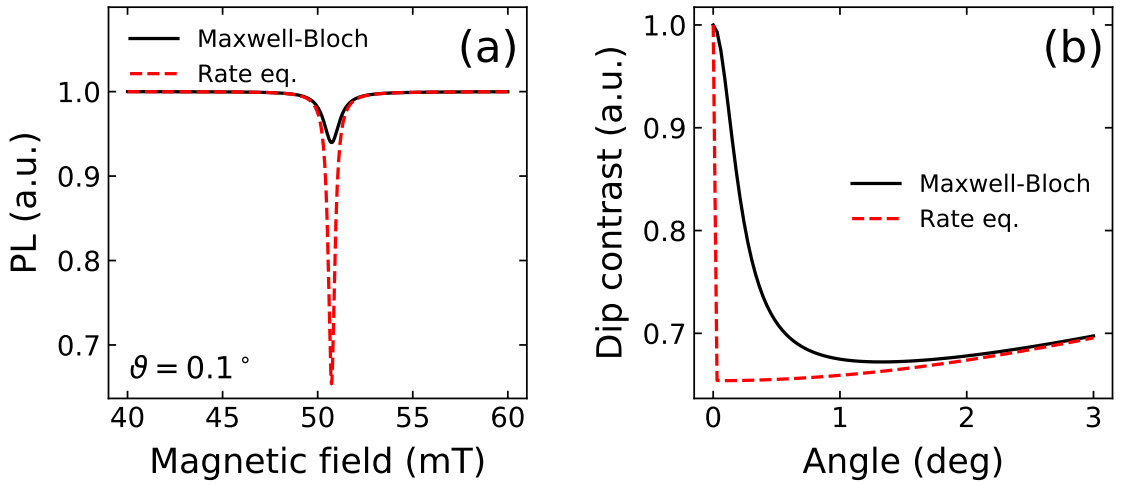

Figure A.2: Comparison of two models for magnetic field-dependent photodynamics of the NV centre, one based on Maxwell-Bloch euqation and the other based on rate equations (from [107]). (a) Fluorescence dip occurring at the magnetic field corresponding to the ESLAC, for a misalignment between NV axis and magnetic field $\vartheta = 0.1°$. The rate equation model does not fully capture the dynamics of the levels at the anti-crossing. The fluorescence dip at the ESLAC has constant contrast for small angles ($\vartheta \ll 1°$). (b) The dip contrast (in this case at the ESLAC) is discontinuous in the rate equation model. The correct dynamics are captured by the Maxwell-Bloch model. The two converge when the angle is large enough.

scanning the frequency of the excitation and solving for the steady-state population, the ODMR response is obtained. When only the strain interaction is present, the two transitions couple to microwave excitation with $\hat{H}$ and $\hat{V}$ polarisation. When an on-axis magnetic field splits the levels, the transitions couple to elliptically polarised MW, and when the eigenstates are purely $|-1\rangle$ and $|+1\rangle$ they couple to σ^- and σ^+.

Magnetic field-dependent photodynamics: comparison of two models

In Section 2.6, I discuss a model of the NV magnetic field-dependent photodynamics based on the Maxwell-Bloch equation for a 7-level system. An analogous model, described in detail in [107], was also tested. It makes use of a rate equation model neglecting the coherence of the quantum states. Since the dynamics are treated in the case of CW excitation, the assumption in general is valid and the two models fully agree. Neglecting the coherence of the states leads only to a minor discrepancy, for small angles ϑ between magnetic field and NV axis and at the vicinity of one of the two level anti-crossings. In this condition, the $|0\rangle$ and $|-\rangle$ levels would be degenerate. However, the small off-axis magnetic field induces a coupling between the two. Hence, the population beats between the two levels at a rate which is proportional to the energy splitting induced by the off-axis field. If the precession

rate is comparable to the excitation and decay rates of the 7-level system, a dip in the photoluminescence at the two anti-crossings is expected, caused by the precession of $|0\rangle$ into $|-\rangle$. The rate equation model captures this but the contrast is not dependent on ϑ (Fig. A.2(a)). This leads to a discontinuity in the contrast at the level anti-crossings: the PL is independent from the magnetic field amplitude when the $\vartheta = 0$ –as expected– but when $\vartheta \ll 0$, no matter how small the angle, the dip contrast is approximately constant. This is unexpected. The correct behaviour would lead to a smoothly decreasing dip contrast for decreasing ϑ, since the precession rate induced by the off-axis field gets weaker and weaker compared to the system dynamics (Fig. A.2(b)).

The two models match away from the level anti-crossing. Hence, for stray fields realistic for scanning NV magnetometry (i.e. $|B| < 20\,\mathrm{mT}$), simulations run with the two models yield the same results. The rate model is preferable because it is computationally much faster than the master equation model.

Hyperfine levels and bias fields

The nitrogen atom which is part the NV adds a perturbation to the electron Hamiltonian. The hyperfine interaction can be visible in the ODMR spectrum (Fig. A.3(a)). The number of visible dips and the frequency splitting is dependent on strain and magnetic field (Fig. A.3(b)). At zero field and in the presence of strain, only two transitions split by $\approx 1\,\mathrm{MHz}$ are visible. Only when the on-axis Zeeman interaction is stronger than the strain splitting, i.e. only when the Hamiltonian eigenstates are also eigenstates of the $S_z \otimes I_z$ operators, three transitions split by 2.2 MHz are visible for each electronic transition.

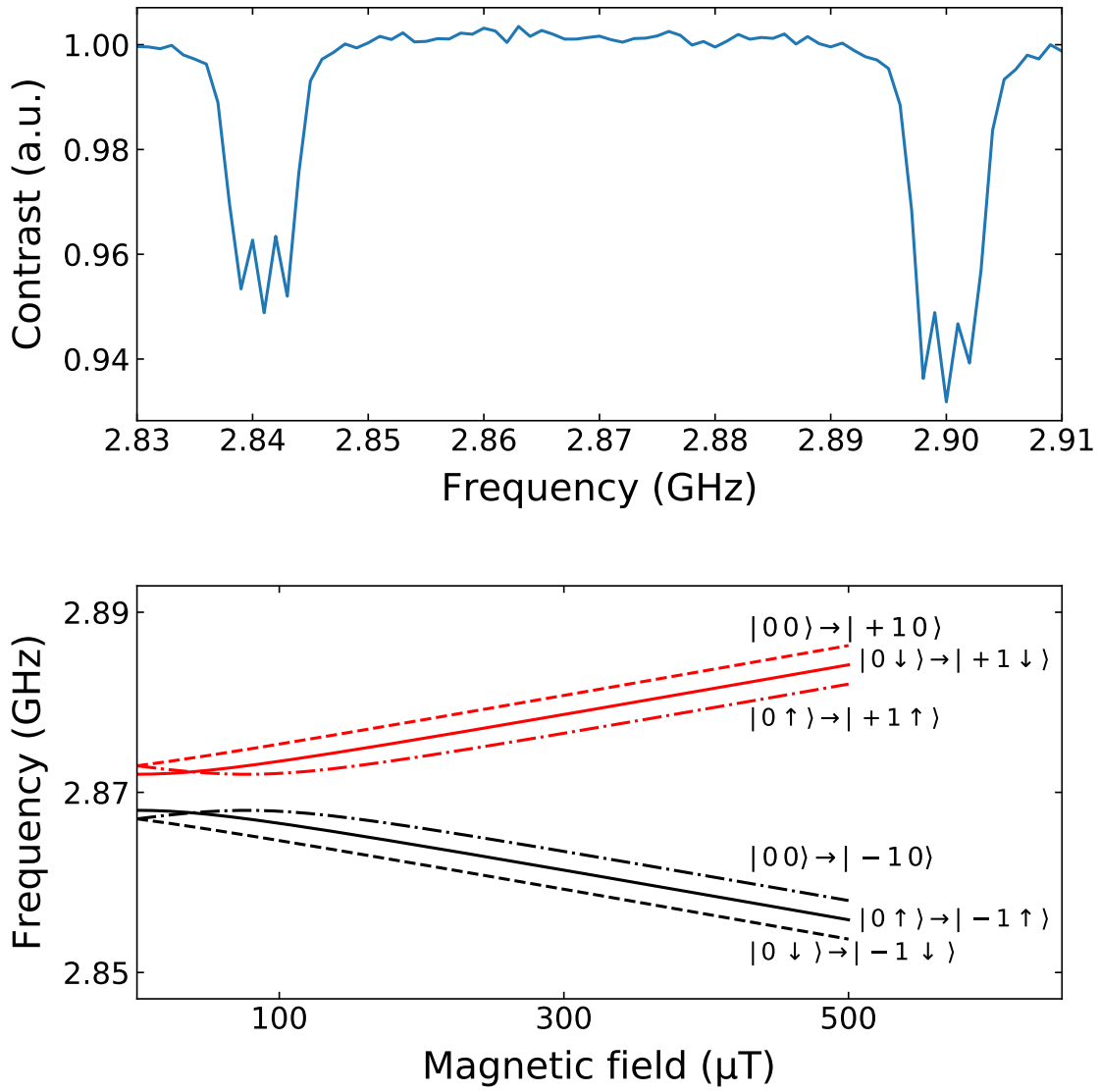

Figure A.3: Hyperfine splitting and ODMR. (a) ODMR with an external magnetic field of 1.1 mT applied along the axis. The three hyperfine transitions are visible in each ODMR dip. (b) Dependence of the $^3A_2$ resonance frequencies as a function of an on-axis external field, with the addition of the hyperfine Hamiltonian (here with ^{14}N, $D = 2.87\,\text{GHz}$ and $E = 2\,\text{MHz}$). At zero field, when the strain interaction is dominant, the eigenstates are a linear superposition of the $S_z \otimes I_z$ eigenvectors. This leads to only two observable transitions separated by $\approx 1\,\text{MHz}$ within each ODMR dip. When an on-axis magnetic field is sufficiently strong, the Hamiltonian eigenstates are also $S_z \otimes I_z$ eigenstates. Within each ODMR dip, three transitions split by 2.2 MHz are visible.

Appendix B

Additional data on PCMO

SQUID measurements

In the main text, I state that magnetic fields stronger than 10 mT significantly perturb the magnetisation of PCMO. I verify this by plotting the total sample out-of-plane magnetic moment as a function of temperature, for different out-of-plane bias fields. The data are taken as described in the main text: the sample is first cooled down to the cryostat base temperature and then polarised with a strong magnetic field. A bias field ranging from −30 mT to 1 T is applied to the sample and the magnetic moment is measured at different temperatures. The magnetisation of the sample is significantly perturbed above bias fields with magnitude larger than

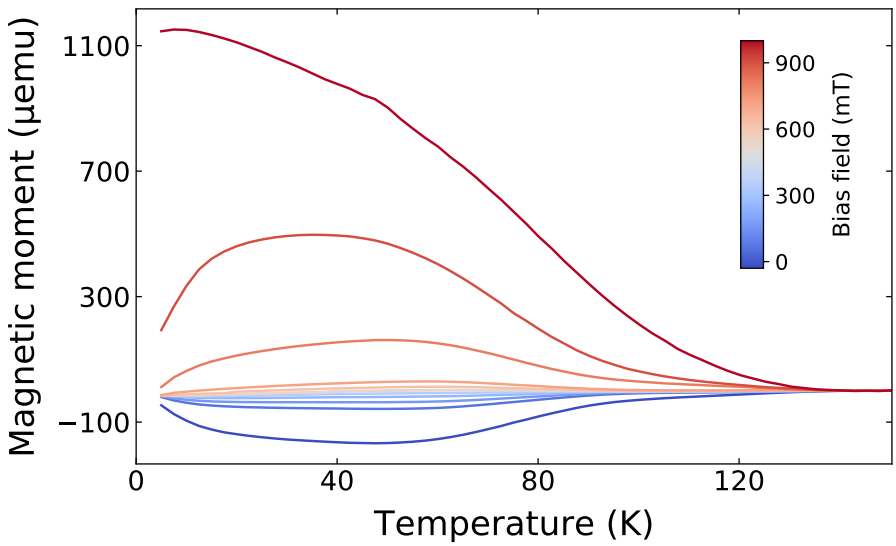

Figure B.1: Effect of a bias field on the PCMO magnetisation. The sample is zero-field cooled, then is polarised by a strong magnetic field and its magnetisation is recorded as function of temperature, for different bias fields. Magnetic fields comparable or greater than 30 mT significantly perturb the PCMO magnetisation.

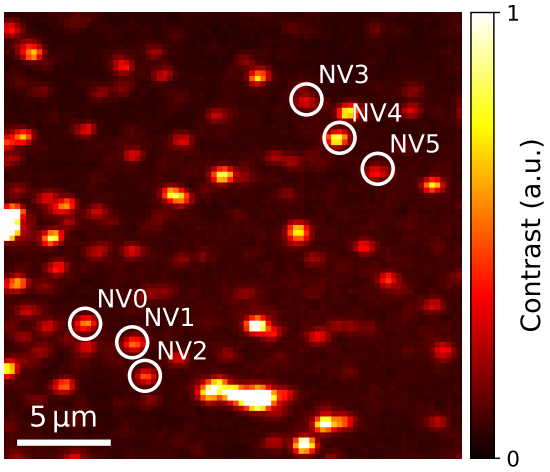

Figure B.2: PL map on PCMO/STO, with a PCMO film thickness of 60 nm. The map is taken at 150 K, well above the PCMO magnetic transition. Two groups of three nanodiamonds are selected. ODMR response of each one is tracked while cooling down the sample to base temperature.

10 mT (Fig. B.1). Hence, if a bias field is applied to the NV, it is important to maintain it below this value to avoid perturbing the stray fields generated from PCMO.

Additional ODMR traces for PCMO/STO

In this section I present the data collected on PCMO with a film thickness of 60 nm, as compared to the one described in Chapter 3, which is 150 nm-thick. After drop-casting the nanodiamonds, the sample is cooled down to around 150 K in order to prevent sample degradation. The low temperature prevents potential damage induced by the laser, which can occur if the sample is kept in vacuum but at room temperature. We select 6 NV centres from a 25 μm $\times$ 25 μm area (Fig. B.2) based on the properties of the NV, i.e. ODMR contrast, strain splitting and fluorescence rate. The NVs are divided in two groups separated by about 15 μm, while the emitters within the same group are less than 4 μm apart. I make sure that there is sample is not magnetic at such temperature by sweeping the setpoint from 150 K to 130 K and ensuring there is no change in the ODMR splitting.

The experimental sequence I follow is slightly different from the one presented in the main text. The sample is first cooled down to 120 K. The temperature is stepped down to the cryostat base temperature. At each step the ODMR is acquired for each of the 6 NV centres. No bias field is applied, in order to avoid perturbing sample magnetism. The data are presented in Figure B.3. No ODMR trace for NV4 is shown, since the ODMR signal vanishes when the PCMO becomes magnetic.

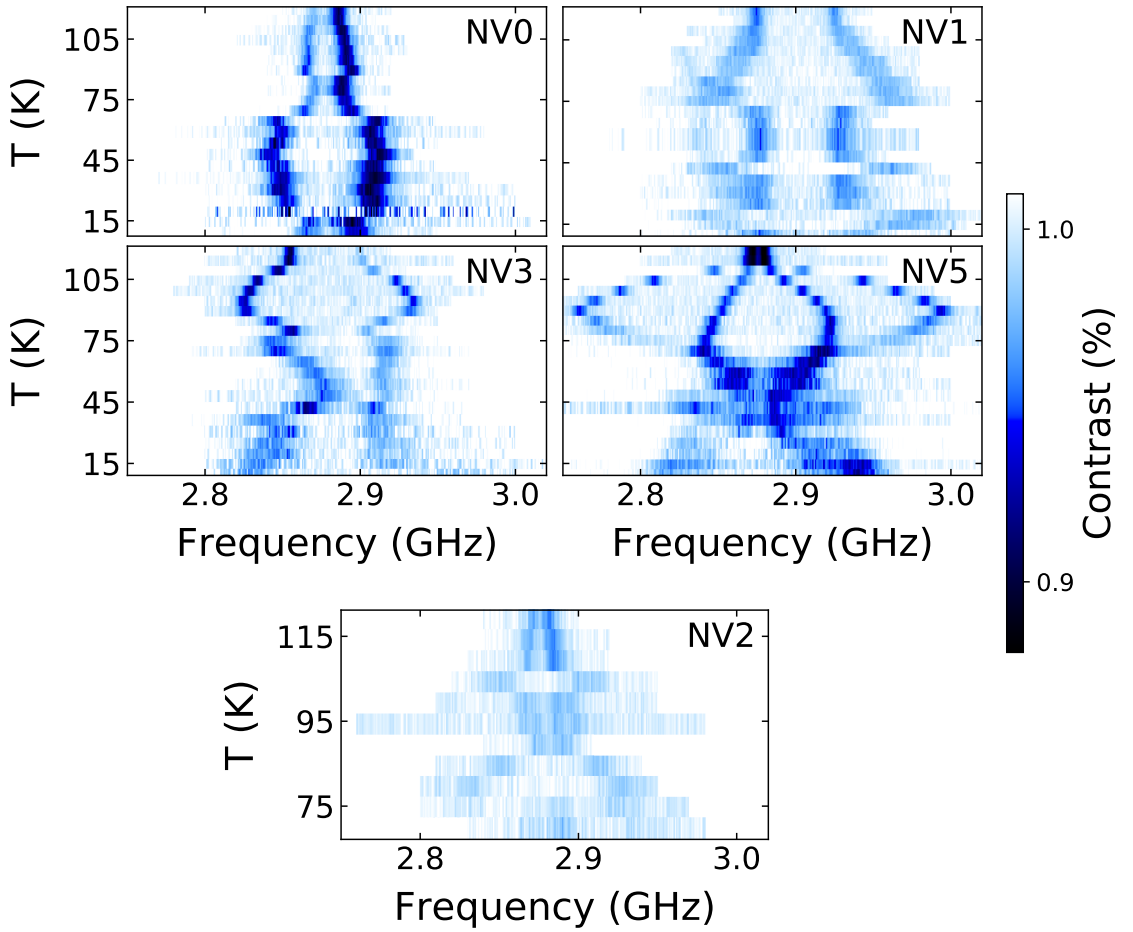

Figure B.3: NV ODMR traces as a function of temperature on a 60 nm-thick PCMO sample. The ODMR traces are measured while cooling down the sample from 120 K to 8 K, without any applied bias field. The signals from NV0-NV1 and from NV3-NV5 show similar evolution, which seems to confirm the results presented in the main text. The signal from NV2 is shown up to 70 K. Below that temperature, the ODMR is not detectable, probably because of the strong stray fields which quench the contrast.

The ODMR of NV2 is not visible below 70 K. The ODMR signal again seems to connected with the location of the emitter. The signals for the two groups (NV0-NV1 and NV3-NV4) have similar temperature evolutions. The two NV centres for the NV5 site detect a rotation of the stray field vector occurring between 110 K and 70 K. We also notice that the Curie temperature of the thin film is higher than the one presented in the main text.

Appendix C

Additional data on the diamond probes

In Subsection 5.4.2 of Chapter 5 the problem of large NV-to-sample distances d_{NV} is discussed. It can be argued that the large values are due to an incorrect setting of the AFM scan parameters, namely the free oscillation amplitude and the setpoint. We verify the influence of these parameters on d_{NV} by measuring it at three different free oscillation amplitude values and at three different setpoint values for each one. The results are presented in Table C.1. No significant reduction is observable from a free oscillation amplitude of 100 mV to 60 mV. This is not entirely surprising, since diamond tips we use in our AFM operate in shear-force mode. Changing the setpoint has a moderate effect on d_{NV}, with a maximum observed reduction of 20 nm when changing the value from 70% to 30% of the free oscillation amplitude.

Another potential explanation for the large NV-to-sample distance is the accumulation of debris on the tip, or protruding parts due to an incorrect fabrication. A diamond tip which has fallen off the quartz prong during a scan, coming from the batch of tips with large d_{NV}, is used to check for this problem. The diamond slab

		Setpoint (Amplitude %)		
		70	50	30
Free oscillation amplitude (mV)	100	400 ± 3 nm	385 ± 3 nm	387 ± 3 nm
	80	402 ± 2 nm	391 ± 3 nm	382 ± 3 nm
	60	392 ± 3 nm	384 ± 3 nm	387 ± 3 nm

Table C.1: NV to sample distance d_{NV} measured on a step. I measure the d_{NV} at three tuning fork free oscillation amplitudes and at three different setpoints for each amplitude value. The fitted values show that the oscillation amplitude does visibly affect in determining a small d_{NV}. This is not entirely unexpected, given that the AFM operates in shear force. The setpoint is more significant for d_{NV} but the maximum reduction is only ≈ 20 nm.

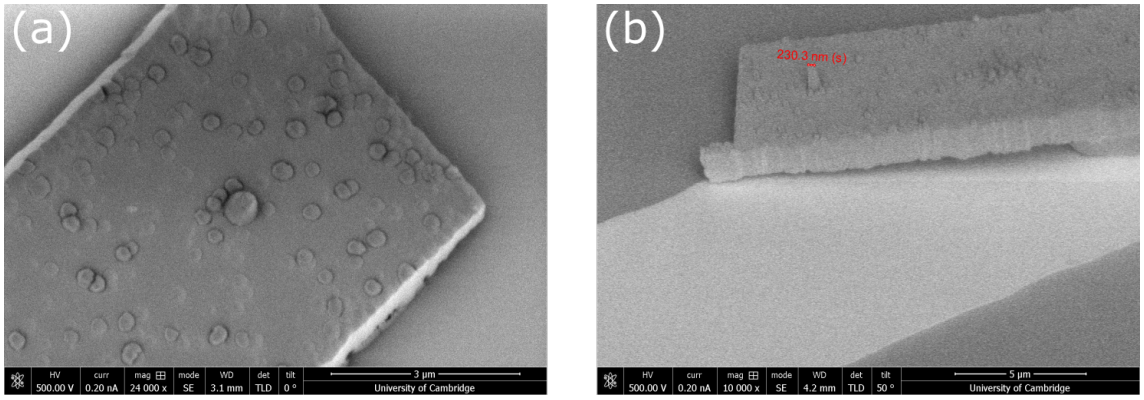

Figure C.1: SEM images of a diamond tip, detached from the quartz prong and resting on a surface both in (a) top view and (b) side view. The tip comes from the batch which shows $d_{NV} > 300\,\text{nm}$. There is no visible debris accumulation or protruding parts which can explain the observed large d_{NV}.

and the pillar are imaged with a scanning electron microscope. I choose not to coat the tip with gold to avoid introducing artifacts to the image. This introduces slight distortions in the images and limits the operating range of the SEM to low vacuum to increase the discharging rate of the sample. The images in Figure C.1 show that there is no visible debris or objects protruding more than $2\,\mu\text{m}$ (the pillar height) from the bottom of the diamond slab.

Bibliography

[1] G. Varvaro and F. Casoli, *Ultrahigh-density magnetic recording: storage materials and media designs* (Jenny Stanford Publishing, 2016) (cited on page 1).

[2] L. Berger, "Emission of spin waves by a magnetic multilayer traversed by a current", Physical Review B **54**, 9353–9358 (1996) (cited on page 1).

[3] J. C. Slonczewski, "Current-driven excitation of magnetic multilayers", Journal of Magnetism and Magnetic Materials **159** (1996) (cited on page 1).

[4] S. S. P. Parkin, M. Hayashi, and L. Thomas, "Magnetic Racetrack Memory", Science **320**, 190–194 (2008) (cited on page 1).

[5] T. H. Skyrme, "A unified field theory of mesons and baryons", Nuclear Physics **31**, 556–569 (1962) (cited on page 1).

[6] S. Mühlbauer, B. Binz, F. Jonietz, C. Pfleiderer, A. Rosch, A. Neubauer, R. Georgii, and P. Böni, "Skyrmion lattice in a chiral magnet", Science **323**, 915–919 (2009) (cited on page 1).

[7] X. Z. Yu, Y. Onose, N. Kanazawa, J. H. Park, J. H. Han, Y. Matsui, N. Nagaosa, and Y. Tokura, "Real-space observation of a two-dimensional skyrmion crystal", Nature **465**, 901–904 (2010) (cited on page 1).

[8] J. Iwasaki, M. Mochizuki, and N. Nagaosa, "Universal current-velocity relation of skyrmion motion in chiral magnets", Nature Communications **4**, 10.1038/ncomms2442 (2013) (cited on page 1).

[9] J. Iwasaki, M. Mochizuki, and N. Nagaosa, "Current-induced skyrmion dynamics in constricted geometries", Nature Nanotechnology **8**, 742–747 (2013) (cited on page 1).

[10] J. Zázvorka, F. Jakobs, D. Heinze, N. Keil, S. Kromin, S. Jaiswal, K. Litzius, G. Jakob, P. Virnau, D. Pinna, K. Everschor-Sitte, L. Rózsa, A. Donges, U. Nowak, and M. Kläui, "Thermal skyrmion diffusion used in a reshuffler device", Nature Nanotechnology **14**, 658–661 (2019) (cited on page 1).

[11] J. Grollier, D. Querlioz, and M. D. Stiles, "Spintronic Nanodevices for Bioinspired Computing", Proceedings of the IEEE **104**, 2024–2039 (2016) (cited on page 1).

[12] F. Ma, Y. Zhou, H. B. Braun, and W. S. Lew, "Skyrmion-Based Dynamic Magnonic Crystal", Nano Letters **15**, 4029–4036 (2015) (cited on page 1).

[13] T. Häberle, F. Haering, H. Pfeifer, L. Han, B. Kuerbanjiang, U. Wiedwald, U. Herr, and B. Koslowski, "Towards quantitative magnetic force microscopy: Theory and experiment", New Journal of Physics **14** (2012) (cited on page 2).

[14] D. Drung, C. Aßmann, J. Beyer, A. Kirste, M. Peters, F. Ruede, and T. Schurig, "Highly sensitive and easy-to-use SQUID sensors", in Ieee transactions on applied superconductivity, Vol. 17, 2 (2007), pages 699–704 (cited on page 2).

[15] J. R. Kirtley, M. B. Ketchen, K. G. Stawiasz, J. Z. Sun, W. J. Gallagher, S. H. Blanton, and S. J. Wind, "High-resolution scanning SQUID microscope", Applied Physics Letters **66**, 1138–1140 (1995) (cited on pages 2, 5).

[16] B. W. Gardner, J. C. Wynn, P. G. Björnsson, E. W. Straver, K. A. Moler, J. R. Kirtley, and M. B. Ketchen, "Scanning superconducting quantum interference device susceptometry", Review of Scientific Instruments **72**, 2361–2364 (2001) (cited on pages 2, 5).

[17] M. E. Huber, N. C. Koshnick, H. Bluhm, L. J. Archuleta, T. Azua, P. G. Björnsson, B. W. Gardner, S. T. Halloran, E. A. Lucero, and K. A. Moler, "Gradiometric micro-SQUID susceptometer for scanning measurements of mesoscopic samples", Review of Scientific Instruments **79** (2008) (cited on pages 2, 5).

[18] A. Finkler, Y. Segev, Y. Myasoedov, M. L. Rappaport, L. Ne'Eman, D. Vasyukov, E. Zeldov, M. E. Huber, J. Martin, and A. Yacoby, "Self-aligned nanoscale SQUID on a tip", Nano Letters **10**, 1046–1049 (2010) (cited on pages 2, 5).

[19] D. Vasyukov, Y. Anahory, L. Embon, D. Halbertal, J. Cuppens, L. Neeman, A. Finkler, Y. Segev, Y. Myasoedov, M. L. Rappaport, M. E. Huber, and E. Zeldov, "A scanning superconducting quantum interference device with single electron spin sensitivity", Nature Nanotechnology **8**, 639–644 (2013) (cited on pages 2, 5).

[20] D. Rugar, R. Budakian, H. J. Mamin, and B. W. Chui, "Single spin detection by magnetic resonance force microscopy", Nature **430**, 329–332 (2004) (cited on pages 3, 5).

[21] C. L. Degen, M. Poggio, H. J. Mamin, C. T. Rettner, and D. Rugar, "Nanoscale magnetic resonance imaging", Proceedings of the National Academy of Sciences of the United States of America **106**, 1313–1317 (2009) (cited on page 3).

[22] G. Boero, M. Demierre, P. A. Besse, and R. S. Popovic, "Micro-Hall devices: Performance, technologies and applications", Sensors and Actuators, A: Physical **106**, 314–320 (2003) (cited on pages 3, 5).

[23] M Bode, "Spin-polarized scanning tunnelling microscopy", Reports on Progress in Physics **66**, 523–582 (2003) (cited on page 3).

[24] I. V. Soldatov and R. Schäfer, "Advances in quantitative Kerr microscopy", Physical Review B **95**, 10.1103/PhysRevB.95.014426 (2017) (cited on page 3).

[25] S. McVitie, D. McGrouther, S. McFadzean, D. A. MacLaren, K. J. O'Shea, and M. J. Benitez, "Aberration corrected Lorentz scanning transmission electron microscopy", Ultramicroscopy **152**, 57–62 (2015) (cited on page 3).

[26] J. Vogel, M. Bonfim, N. Rougemaille, O. Boulle, I. M. Miron, S. Auffret, B. Rodmacq, G. Gaudin, J. C. Cezar, F. Sirotti, and S. Pizzini, "Direct observation of massless domain wall dynamics in nanostripes with perpendicular magnetic anisotropy", Physical Review Letters **108** (2012) (cited on page 3).

[27] B. M. Chernobrod and G. P. Berman, "Spin microscope based on optically detected magnetic resonance", Journal of Applied Physics **97** (2005) (cited on page 3).

[28] J. M. Taylor, P. Cappellaro, L. Childress, L. Jiang, D. Budker, P. R. Hemmer, A. Yacoby, R. Walsworth, and M. D. Lukin, "High-sensitivity diamond magnetometer with nanoscale resolution", Nature Physics **4**, 810–816 (2008) (cited on page 3).

[29] A. Gruber, A. Dräbenstedt, C. Tietz, L. Fleury, J. Wrachtrup, and C. Von Borczyskowski, "Scanning confocal optical microscopy and magnetic resonance on single defect centers", Science (1997) (cited on page 4).

[30] F. Jelezko, T. Gaebel, I. Popa, A. Gruber, and J. Wrachtrup, "Observation of Coherent Oscillations in a Single Electron Spin", Physical Review Letters **92**, 076401 (2004) (cited on pages 4, 24).

[31] L. Childress, M. V. Gurudev Dutt, J. M. Taylor, A. S. Zibrov, F. Jelezko, J. Wrachtrup, P. R. Hemmer, and M. D. Lukin, "Coherent dynamics of coupled electron and nuclear spin qubits in diamond", Science **314**, 281–285 (2006) (cited on page 4).

[32] M. V. Gurudev Dutt, L. Childress, L. Jiang, E. Togan, J. Maze, F. Jelezko, A. S. Zibrov, P. R. Hemmer, and M. D. Lukin, "Quantum register based on individual electronic and nuclear spin qubits in diamond", Science **316**, 1312–1316 (2007) (cited on page 4).

[33] C. Bradley, J. Randall, M. Abobeih, R. Berrevoets, M. Degen, M. Bakker, M. Markham, D. Twitchen, and T. Taminiau, "A Ten-Qubit Solid-State Spin Register with Quantum Memory up to One Minute", Physical Review X **9**, 031045 (2019) (cited on pages 4, 27).

[34] M. Chen, M. Hirose, and P. Cappellaro, "Measurement of transverse hyperfine interaction by forbidden transitions", Physical Review B **92**, 020101 (2015) (cited on pages 4, 20).

[35] B. J. Hausmann, T. M. Babinec, J. T. Choy, J. S. Hodges, S. Hong, I. Bulu, A. Yacoby, M. D. Lukin, and M. Lončar, "Single-color centers implanted in diamond nanostructures", New Journal of Physics **13** (2011) (cited on page 4).

[36] M. Lesik, P. Spinicelli, S. Pezzagna, P. Happel, V. Jacques, O. Salord, B. Rasser, A. Delobbe, P. Sudraud, A. Tallaire, J. Meijer, and J.-F. Roch, "Maskless and targeted creation of arrays of colour centres in diamond using focused ion beam technology", physica status solidi (a) **210**, 2055–2059 (2013) (cited on page 4).

[37] T. Staudacher, F. Ziem, L. Häussler, R. Stöhr, S. Steinert, F. Reinhard, J. Scharpf, A. Denisenko, and J. Wrachtrup, "Enhancing the spin properties of shallow implanted nitrogen vacancy centers in diamond by epitaxial overgrowth", Applied Physics Letters **101** (2012) (cited on page 4).

[38] S. A. Momenzadeh, R. J. Stöhr, F. F. de Oliveira, A. Brunner, A. Denisenko, S. Yang, F. Reinhard, and J. Wrachtrup, "Nanoengineered Diamond Waveguide as a Robust Bright Platform for Nanomagnetometry Using Shallow Nitrogen Vacancy Centers", Nano Letters **15**, 165–169 (2015) (cited on page 4).

[39] J. F. Barry, J. M. Schloss, E. Bauch, M. J. Turner, C. A. Hart, L. M. Pham, and R. L. Walsworth, "Sensitivity Optimization for NV-Diamond Magnetometry", ArXiv e-prints (2019) (cited on page 4).

[40] T. Wolf, P. Neumann, K. Nakamura, H. Sumiya, T. Ohshima, J. Isoya, and J. Wrachtrup, "Subpicotesla diamond magnetometry", Physical Review X **5**, 10.1103/PhysRevX.5.041001 (2015) (cited on page 4).

[41] J. P. Tetienne, N. Dontschuk, D. A. Broadway, A. Stacey, D. A. Simpson, and L. C. Hollenberg, "Quantum imaging of current flow in graphene", Science Advances **3**, 10.1126/sciadv.1602429 (2017) (cited on page 4).

[42] D. Le Sage, K. Arai, D. R. Glenn, S. J. Devience, L. M. Pham, L. Rahn-Lee, M. D. Lukin, A. Yacoby, A. Komeili, and R. L. Walsworth, "Optical magnetic imaging of living cells", Nature **496**, 486–489 (2013) (cited on pages 4, 42).

[43] J. F. Barry, M. J. Turner, J. M. Schloss, D. R. Glenn, Y. Song, M. D. Lukin, H. Park, and R. L. Walsworth, "Optical magnetic detection of single-neuron action potentials using quantum defects in diamond", Proceedings of the National Academy of Sciences of the United States of America **113**, 14133–14138 (2016) (cited on page 4).

[44] B. Grotz, J. Beck, P. Neumann, B. Naydenov, R. Reuter, F. Reinhard, F. Jelezko, J. Wrachtrup, D. Schweinfurth, B. Sarkar, and P. Hemmer, "Sensing external spins with nitrogen-vacancy diamond", New Journal of Physics **13**, 10.1088/1367-2630/13/5/055004 (2011) (cited on page 4).

[45] H. J. Mamin, M. H. Sherwood, and D. Rugar, "Detecting external electron spins using nitrogen-vacancy centers", Physical Review B - Condensed Matter and Materials Physics **86**, 10.1103/PhysRevB.86.195422 (2012) (cited on page 4).

[46] L. Gross, F. Mohn, N. Moll, P. Liljeroth, and G. Meyer, "The chemical structure of a molecule resolved by atomic force microscopy", Science **325**, 1110–1114 (2009) (cited on page 4).

[47] T. Staudacher, F. Shi, S. Pezzagna, J. Meijer, J. Du, C. A. Meriles, F. Reinhard, and J. Wrachtrup, "Nuclear magnetic resonance spectroscopy on a (5-nanometer)^3 sample volume", Science **339**, 561–563 (2013) (cited on pages 4–5).

[48] G. Balasubramanian, I. Y. Chan, R. Kolesov, M. Al-Hmoud, J. Tisler, C. Shin, C. Kim, A. Wojcik, P. R. Hemmer, A. Krueger, T. Hanke, A. Leitenstorfer, R. Bratschitsch, F. Jelezko, and J. Wrachtrup, "Nanoscale imaging magnetometry with diamond spins under ambient conditions", Nature **455**, 648–651 (2008) (cited on pages 4, 18, 63, 79).

[49] L. Rondin, J. P. Tetienne, P. Spinicelli, C. Dal Savio, K. Karrai, G. Dantelle, A. Thiaville, S. Rohart, J. F. Roch, and V. Jacques, "Nanoscale magnetic field mapping with a single spin scanning probe magnetometer", Applied Physics Letters **100**, 10.1063/1.3703128 (2012) (cited on pages 4, 88, 90–91).

[50] P. Maletinsky, S. Hong, M. S. Grinolds, B. Hausmann, M. D. Lukin, R. L. Walsworth, M. Loncar, and A. Yacoby, "A robust scanning diamond sensor for nanoscale imaging with single nitrogen-vacancy centres", Nature Nanotechnology **7**, 320–324 (2012) (cited on pages 4–5, 88, 104).

[51] M. Pelliccione, A. Jenkins, P. Ovartchaiyapong, C. Reetz, E. Emmanouilidou, N. Ni, and A. C. B. Jayich, "Scanned probe imaging of nanoscale magnetism at cryogenic temperatures with a single-spin quantum sensor", **11**, 700–705 (2016) (cited on page 5).

[52] Y. Dovzhenko, F. Casola, S. Schlotter, T. X. Zhou, F. Büttner, R. L. Walsworth, G. S. Beach, and A. Yacoby, "Magnetostatic twists in room-temperature skyrmions explored by nitrogen-vacancy center spin texture reconstruction", Nature Communications **9**, 10.1038/s41467-018-05158-9 (2018) (cited on page 5).

[53] M. S. Grinolds, S. Hong, P. Maletinsky, L. Luan, M. D. Lukin, R. L. Walsworth, and A. Yacoby, "Nanoscale magnetic imaging of a single electron spin under ambient conditions", Nature Physics **9**, 215–219 (2013) (cited on pages 5, 27, 42).

[54] C. Degen, "Nanoscale magnetometry: Microscopy with single spins", Nature Nanotechnology **3**, 643–644 (2008) (cited on page 5).

[55] H. J. Mamin, R. Budakian, B. W. Chui, and D. Rugar, "Detection and manipulation of statistical polarization in small spin ensembles", Physical Review Letters **91**, 10.1103/PhysRevLett.91.207604 (2003) (cited on page 5).

[56] H. J. Mamin, T. H. Oosterkamp, M. Poggio, C. L. Degen, C. T. Rettner, and D. Rugar, "Isotope-Selective Detection and Imaging of Organic Nanolayers", Nano Letters **9**, 3020–3024 (2009) (cited on page 5).

[57] H. J. Mamin, M. Kim, M. H. Sherwood, C. T. Rettner, K. Ohno, D. D. Awschalom, and D. Rugar, "Nanoscale Nuclear Magnetic Resonance with a Nitrogen-Vacancy Spin Sensor", Science **339**, 557–560 (2013) (cited on pages 5, 27).

[58] B. K. Ofori-Okai, S. Pezzagna, K. Chang, M. Loretz, R. Schirhagl, Y. Tao, B. A. Moores, K. Groot-Berning, J. Meijer, and C. L. Degen, "Spin properties of very shallow nitrogen vacancy defects in diamond", Physical Review B **86**, 10.1103/PhysRevB.86.081406 (2012) (cited on page 5).

[59] H. S. Knowles, D. M. Kara, and M. Atatüre, "Observing bulk diamond spin coherence in high-purity nanodiamonds", Nature Materials **13**, 21–25 (2013) (cited on pages 5, 37).

[60] J. R. Maze, P. L. Stanwix, J. S. Hodges, S. Hong, J. M. Taylor, P. Cappellaro, L. Jiang, M. V. Dutt, E. Togan, A. S. Zibrov, A. Yacoby, R. L. Walsworth, and M. D. Lukin, "Nanoscale magnetic sensing with an individual electronic spin in diamond", Nature **455**, 644–647 (2008) (cited on page 5).

[61] D. R. Glenn, D. B. Bucher, J. Lee, M. D. Lukin, H. Park, and R. L. Walsworth, "High-resolution magnetic resonance spectroscopy using a Solid-State spin sensor", Nature **555**, 351–354 (2018) (cited on page 5).

[62] J.-P. Tetienne, T. Hingant, J.-V. Kim, L. H. Diez, J.-P. Adam, K. Garcia, J.-F. Roch, S. Rohart, A. Thiaville, D. Ravelosona, and V. Jacques, "Nanoscale imaging and control of domain-wall hopping with a nitrogen-vacancy center microscope", Science **344**, 1366–1369 (2014) (cited on page 5).

[63] I. Gross, L. J. Martínez, J. P. Tetienne, T. Hingant, J. F. Roch, K. Garcia, R. Soucaille, J. P. Adam, J. V. Kim, S. Rohart, A. Thiaville, J. Torrejon, M. Hayashi, and V. Jacques, "Direct measurement of interfacial Dzyaloshinskii-Moriya interaction in X—CoFeB—MgO heterostructures with a scanning NV magnetometer (X=Ta,TaN, and W)", Physical Review B **94**, 1–8 (2016) (cited on page 5).

[64] I. Gross, W. Akhtar, V. Garcia, L. J. Martínez, S. Chouaieb, K. Garcia, C. Carrétéro, A. Barthélémy, P. Appel, P. Maletinsky, J.-V. Kim, J. Y. Chauleau, N. Jaouen, M. Viret, M. Bibes, S. Fusil, and V. Jacques, "Real-space imaging of non-collinear antiferromagnetic order with a single-spin magnetometer", Nature **549**, 252–256 (2017) (cited on page 5).

[65] L Thiel, D Rohner, M Ganzhorn, P Appel, E Neu, B Müller, R Kleiner, D Koelle, and P Maletinsky, "Quantitative nanoscale vortex imaging using a cryogenic quantum magnetometer", Nature Nanotechnology **11**, 677–681 (2016) (cited on page 5).

[66] P. Wang, S. Chen, M. Guo, S. Peng, M. Wang, M. Chen, W. Ma, R. Zhang, J. Su, X. Rong, F. Shi, T. Xu, and J. Du, "Nanoscale magnetic imaging of ferritins in a single cell", Science Advances **5**, 10.1126/sciadv.aau8038 (2019) (cited on page 6).

[67] J. P. Tetienne, A. Lombard, D. A. Simpson, C. Ritchie, J. Lu, P. Mulvaney, and L. C. Hollenberg, "Scanning Nanospin Ensemble Microscope for Nanoscale Magnetic and Thermal Imaging", Nano Letters **16**, 326–333 (2016) (cited on pages 6, 42).

[68] P. Appel, M. Ganzhorn, E. Neu, and P. Maletinsky, "Nanoscale microwave imaging with a single electron spin in diamond", New Journal of Physics **17**, 10.1088/1367-2630/17/11/112001 (2015) (cited on pages 6, 42).

[69] A. Ariyaratne, D. Bluvstein, B. A. Myers, and A. C. Jayich, "Nanoscale electrical conductivity imaging using a nitrogen-vacancy center in diamond", Nature Communications **9**, 10.1038/s41467-018-04798-1 (2018) (cited on pages 6, 42).

[70] M. A. Pinault, J. Barjon, T. Kociniewski, F. Jomard, and J. Chevallier, "The n-type doping of diamond: Present status and pending questions", Physica B: Condensed Matter **401-402**, 51–56 (2007) (cited on page 9).

[71] E. A. Ekimov, V. A. Sidorov, E. D. Bauer, N. N. Mel'nik, N. J. Curro, J. D. Thompson, and S. M. Stishov, "Superconductivity in diamond", Nature **428**, 542–545 (2004) (cited on page 9).

[72] F. Jelezko and J. Wrachtrup, "Single defect centres in diamond: A review", physica status solidi (a) **203**, 3207–3225 (2006) (cited on page 9).

[73] A. Gali, M. Fyta, and E. Kaxiras, "Ab initio supercell calculations on nitrogen-vacancy center in diamond: Electronic structure and hyperfine tensors", Physical Review B **77**, 155206 (2008) (cited on page 10).

[74] A. Gali, "Theory of the neutral nitrogen-vacancy center in diamond and its application to the realization of a qubit", Physical Review B - Condensed Matter and Materials Physics **79**, 10.1103/PhysRevB.79.235210 (2009) (cited on page 10).

[75] J. H. N. Loubser and J. A. van Wyk, "Electron spin resonance in the study of diamond", Reports on Progress in Physics **41**, 1201–1248 (1978) (cited on page 10).

[76] Y. Mita, "Change of absorption spectra in type-I b diamond with heavy neutron irradiation", Physical Review B **53**, 11360–11364 (1996) (cited on page 10).

[77] B. J. Shields, Q. P. Unterreithmeier, N. P. de Leon, H. Park, and M. D. Lukin, "Efficient Readout of a Single Spin State in Diamond via Spin-to-Charge Conversion", Physical Review Letters **114**, 136402 (2015) (cited on page 10).

[78] E. Bourgeois, A. Jarmola, P. Siyushev, M. Gulka, J. Hruby, F. Jelezko, D. Budker, and M. Nesladek, "Photoelectric detection of electron spin resonance of nitrogen-vacancy centres in diamond", Nature Communications **6**, 8577 (2015) (cited on page 10).

[79] L. Rondin, G. Dantelle, A. Slablab, F. Grosshans, F. Treussart, P. Bergonzo, S. Perruchas, T. Gacoin, M. Chaigneau, H. C. Chang, V. Jacques, and J. F. Roch, "Surface-induced charge state conversion of nitrogen-vacancy defects in nanodiamonds", Physical Review B - Condensed Matter and Materials Physics **82**, 1–5 (2010) (cited on page 10).

[80] K.-M. C. Fu, C. Santori, P. E. Barclay, and R. G. Beausoleil, "Conversion of neutral nitrogen-vacancy centers to negatively charged nitrogen-vacancy centers through selective oxidation", Applied Physics Letters **96**, 121907 (2010) (cited on page 10).

[81] M. V. Hauf, B. Grotz, B. Naydenov, M. Dankerl, S. Pezzagna, J. Meijer, F. Jelezko, J. Wrachtrup, M. Stutzmann, F. Reinhard, and J. A. Garrido, "Chemical control of the charge state of nitrogen-vacancy centers in diamond", Physical Review B - Condensed Matter and Materials Physics **83**, 1–4 (2011) (cited on page 10).

[82] N Aslam, G Waldherr, P Neumann, F Jelezko, and J Wrachtrup, "Photo-induced ionization dynamics of the nitrogen vacancy defect in diamond investigated by single-shot charge state detection", New Journal of Physics **15**, 013064 (2013) (cited on pages 10–11).

[83] P. Siyushev, H. Pinto, M. Vörös, A. Gali, F. Jelezko, and J. Wrachtrup, "Optically Controlled Switching of the Charge State of a Single Nitrogen-Vacancy Center in Diamond at Cryogenic Temperatures", Physical Review Letters **110**, 167402 (2013) (cited on page 10).

[84] M. W. Doherty, N. B. Manson, P. Delaney, and L. C. L. Hollenberg, "The negatively charged nitrogen-vacancy centre in diamond: The electronic solution", New Journal of Physics **13**, 10.1088/1367-2630/13/2/025019 (2011) (cited on pages 10–11).

[85] A. Gali, E. Janzén, P. Deák, G. Kresse, and E. Kaxiras, "Theory of Spin-Conserving Excitation of the N-V-Center in Diamond", Physical Review Letters **103**, 1–4 (2009) (cited on pages 10–11).

[86] N. Reddy, N. Manson, and E. Krausz, "Two-laser spectral hole burning in a colour centre in diamond", Journal of Luminescence **38**, 46–47 (1987) (cited on page 11).

[87] S. C. Rand, D. Redman, S Brown, and R. H. Sands, "Spin Dynamics and Electronic States of N-V Centers in Diamond by EPR and Four-Wave-Mixing Spectroscopy", Physical Review Letters **67**, 3420–3423 (1991) (cited on pages 11, 33).

[88] E van Oort, N. B. Manson, and M Glasbeek, "Optically detected spin coherence of the diamond N-V centre in its triplet ground state", Journal of Physics C: Solid State Physics **21**, 4385–4391 (1988) (cited on page 11).

[89] N. B. Manson, X.-F. He, and P. T. H. Fisk, "Raman heterodyne detected electron-nuclear-double-resonance measurements of the nitrogen-vacancy center in diamond", Optics Letters **15**, 1094 (1990) (cited on page 11).

[90] E. Togan, Y. Chu, A. S. Trifonov, L. Jiang, J. Maze, L. Childress, M. V. Dutt, A. S. Sørensen, P. R. Hemmer, A. S. Zibrov, and M. D. Lukin, "Quantum entanglement between an optical photon and a solid-state spin qubit", Nature **466**, 730–734 (2010) (cited on pages 11, 13).

[91] L. Robledo, H. Bernien, T. van der Sar, and R. Hanson, "Spin dynamics in the optical cycle of single nitrogen-vacancy centres in diamond", New Journal of Physics **13**, 025013 (2011) (cited on pages 12, 32–33).

[92] J. Harrison, M. Sellars, and N. Manson, "Measurement of the optically induced spin polarisation of N-V centres in diamond", Diamond and Related Materials **15**, 586–588 (2006) (cited on page 12).

[93] C. L. Degen, F. Reinhard, and P. Cappellaro, "Quantum sensing", Reviews of Modern Physics **89**, 1–39 (2016) (cited on pages 13, 28–29).

[94] R. N. Patel, T. Schröder, N. Wan, L. Li, S. L. Mouradian, E. H. Chen, and D. R. Englund, "Efficient photon coupling from a diamond nitrogen vacancy center by integration with silica fiber", Light: Science & Applications **5**, e16032–e16032 (2016) (cited on page 14).

[95] L Rondin, J. P. Tetienne, T Hingant, J. F. Roch, P Maletinsky, and V Jacques, "Magnetometry with nitrogen-vacancy defects in diamond", Rep Prog Phys **77**, 56503 (2014) (cited on page 15).

[96] G. Kucsko, P. C. Maurer, N. Y. Yao, M. Kubo, H. J. Noh, P. K. Lo, H. Park, and M. D. Lukin, "Nanometre-scale thermometry in a living cell", Nature **500**, 54–58 (2013) (cited on page 15).

[97] M. W. Doherty, F. Dolde, H. Fedder, F. Jelezko, J. Wrachtrup, N. B. Manson, and L. C. L. Hollenberg, "Theory of the ground-state spin of the NV-center in diamond", Physical Review B **85**, 205203 (2012) (cited on page 16).

[98] F. T. Charnock and T. A. Kennedy, "Combined optical and microwave approach for performing quantum spin operations on the nitrogen-vacancy center in diamond", Physical Review B **64**, 041201 (2001) (cited on page 20).

[99] B. Smeltzer, J. McIntyre, and L. Childress, "Robust control of individual nuclear spins in diamond", Physical Review A **80**, 050302 (2009) (cited on page 20).

[100] J. R. Rabeau, P. Reichart, G. Tamanyan, D. N. Jamieson, S. Prawer, F. Jelezko, T. Gaebel, I. Popa, M. Domhan, and J. Wrachtrup, "Implantation of labelled single nitrogen vacancy centers in diamond using ^{15}N", Applied Physics Letters **88**, 023113 (2006) (cited on page 20).

[101] V. Jacques, P. Neumann, J. Beck, M. Markham, D. Twitchen, J. Meijer, F. Kaiser, G. Balasubramanian, F. Jelezko, and J. Wrachtrup, "Dynamic polarization of single nuclear spins by optical pumping of nitrogen-vacancy color centers in diamond at room temperature", Physical Review Letters **102**, 7–10 (2009) (cited on page 20).

[102] A. Dréau, M. Lesik, L. Rondin, P. Spinicelli, O. Arcizet, J. F. Roch, and V. Jacques, "Avoiding power broadening in optically detected magnetic resonance of single NV defects for enhanced dc magnetic field sensitivity", Physical Review B - Condensed Matter and Materials Physics **84**, 1–8 (2011) (cited on pages 21, 25, 28–29).

[103] N. F. Ramsey, "A Molecular Beam Resonance Method with Separated Oscillating Fields", Physical Review **78**, 695–699 (1950) (cited on page 25).

[104] M. Markham, J. Dodson, G. Scarsbrook, D. Twitchen, G. Balasubramanian, F. Jelezko, and J. Wrachtrup, "CVD diamond for spintronics", Diamond and Related Materials **20**, 134–139 (2011) (cited on page 27).

[105] B. Naydenov, F. Dolde, L. T. Hall, C. Shin, H. Fedder, L. C. L. Hollenberg, F. Jelezko, and J. Wrachtrup, "Dynamical decoupling of a single-electron spin at room temperature", Physical Review B **83**, 081201 (2011) (cited on page 27).

[106] E. L. Hahn, "Spin Echoes", Physical Review **80**, 580–594 (1950) (cited on page 27).

[107] J. P. Tetienne, L. Rondin, P. Spinicelli, M. Chipaux, T. Debuisschert, J. F. Roch, and V. Jacques, "Magnetic-field-dependent photodynamics of single NV defects in diamond: An application to qualitative all-optical magnetic imaging", New Journal of Physics **14**, 10.1088/1367-2630/14/10/103033 (2012) (cited on pages 32–33, 117).

[108] P. Appel, E. Neu, M. Ganzhorn, A. Barfuss, M. Batzer, M. Gratz, A. Tschöpe, and P. Maletinsky, "Fabrication of all diamond scanning probes for nanoscale magnetometry", Review of Scientific Instruments, 10.1063/1.4952953 (2016) (cited on page 38).

[109] V. M. Acosta, E. Bauch, M. P. Ledbetter, A. Waxman, L. S. Bouchard, and D. Budker, "Temperature dependence of the nitrogen-vacancy magnetic resonance in diamond", Physical Review Letters **104**, 10.1103/PhysRevLett.104.070801 (2010) (cited on page 42).

[110] D. R. Glenn, R. R. Fu, P. Kehayias, D. Le Sage, E. A. Lima, B. P. Weiss, and R. L. Walsworth, "Micrometer-scale magnetic imaging of geological samples using a quantum diamond microscope", Geochemistry, Geophysics, Geosystems **18**, 3254–3267 (2017) (cited on page 42).

[111] A. Horsley, P. Appel, J. Wolters, J. Achard, A. Tallaire, P. Maletinsky, and P. Treutlein, "Microwave Device Characterization Using a Widefield Diamond Microscope", Physical Review Applied **10**, 10.1103/PhysRevApplied.10.044039 (2018) (cited on page 42).

[112] S. Steinert, F. Dolde, P. Neumann, A. Aird, B. Naydenov, G. Balasubramanian, F. Jelezko, and J. Wrachtrup, "High sensitivity magnetic imaging using an array of spins in diamond", Review of Scientific Instruments **81**, 10.1063/1.3385689 (2010) (cited on page 42).

[113] J. Goodenough, W. Gräper, F. Holtzberg, D. Huber, R. Lefever, J. Longo, T. McGuire, and S. Methfessel, *Magnetic and Other Properties Of Oxides and Related Compounds*, edited by K.-H. Hellwege and A. Hellwege, Vol. 2010 (Landolt-Börnstein, New Series III/4a, 2012) (cited on page 45).

[114] A.-M. Haghiri-Gosnet and J.-P. Renard, "CMR manganites: physics, thin films and devices", Journal of Physics D: Applied Physics **36**, R127–R150 (2003) (cited on page 46).

[115] C. H. Chen and S. W. Cheong, "Commensurate to incommensurate charge ordering and its real-space images in $La_{0.5}Ca_{0.5}MnO_3$", Physical Review Letters **76**, 4042–4045 (1996) (cited on page 46).

[116] W. E. Pickett and D. J. Singh, "Electronic structure and half-metallic transport in t system", Physical Review B - Condensed Matter and Materials Physics **53**, 1146–1160 (1996) (cited on page 46).

[117] J. B. Goodenough, "Theory of the role of covalence in the perovskite-type manganites [La,M(II)]MnO_3", Physical Review **100**, 564–573 (1955) (cited on page 47).

[118] J. B. Goodenough, "An interpretation of the magnetic properties of the perovskite-type mixed crystals $La_{1-x}Sr_xCoO_{3-\lambda}$", Journal of Physics and Chemistry of Solids **6**, 287–297 (1958) (cited on page 47).

[119] J. Kanamori, "Superexchange interaction and symmetry properties of electron orbitals", Journal of Physics and Chemistry of Solids **10**, 87–98 (1959) (cited on page 47).

[120] C. Zener, "Interaction between the d-shells in the transition metals. II. Ferromagnetic compounds of manganese with Perovskite structure", Physical Review **82**, 403–405 (1951) (cited on page 47).

[121] M. B. Salamon and M. Jaime, "The physics of manganites: Structure and transport", Reviews of Modern Physics **73**, 583–628 (2001) (cited on page 47).

[122] J. M. D. Coey, M. Viret, L. Ranno, and K. Ounadjela, "Electron Localization in Mixed-Valence Manganites", Physical Review Letters **75**, 3910–3913 (1995) (cited on page 47).

[123] H. Y. Hwang, S.-W. Cheong, P. G. Radaelli, M. Marezio, and B. Batlogg, "Lattice Effects on the Magnetoresistance in Doped $LaMnO_3$", Physical Review Letters **75**, 914–917 (1995) (cited on page 47).

[124] W. Prellier, P. Lecoeur, and B. Mercey, *Colossal-magnetoresistive manganite thin films*, 2001 (cited on page 47).

[125] A. M. Haghiri-Gosnet, J. Wolfman, B. Mercey, C. Simon, P. Lecoeur, M. Korzenski, M. Hervieu, R. Desfeux, and G. Baldinozzi, "Microstructure and magnetic properties of strained $La_{0.7}Sr_{0.3}MnO_3$ thin films", Journal of Applied Physics **88**, 4257–4264 (2000) (cited on pages 47–48).

[126] W Prellier, C. Simon, B Mercey, and B Raveau, "Thickness dependence of the stability of the charge-ordered state in $Pr_{0.5}Ca_{0.5}MnO_3$ thin films", Physical Review B **62**, 337–340 (2000) (cited on page 47).

[127] A. J. Millis, T. Darling, and A. Migliori, "Quantifying strain dependence in "colossal" magnetoresistance manganites", Journal of Applied Physics **83**, 1588–1591 (1998) (cited on page 48).

[128] T. Kanki, H. Tanaka, and T. Kawai, "Anomalous strain effect in $La_{0.8}Ba_{0.2}MnO_3$ epitaxial thin film: Role of the orbital degree of freedom in stabilizing ferromagnetism", Physical Review B **64**, 224418 (2001) (cited on page 48).

[129] T. K. Nath, R. A. Rao, D. Lavric, C. B. Eom, L. Wu, and F. Tsui, "Effect of three-dimensional strain states on magnetic anisotropy of $La_{0.8}Ca_{0.2}MnO_3$ epitaxial thin films", Applied Physics Letters **74**, 1615–1617 (1999) (cited on page 48).

[130] Y. Suzuki, H. Y. Hwang, S.-W. Cheong, and R. B. van Dover, "The role of strain in magnetic anisotropy of manganite thin films", Applied Physics Letters **71**, 140–142 (1997) (cited on page 48).

[131] F. Tsui, M. C. Smoak, T. K. Nath, and C. B. Eom, "Strain-dependent magnetic phase diagram of epitaxial $La_{0.67}Sr_{0.33}MnO_3$ thin films", Applied Physics Letters **76**, 2421–2423 (2000) (cited on page 48).

[132] K. A. Müller, W. Berlinger, and F. Waldner, "Characteristic structural phase transition in perovskite-type compounds", Physical Review Letters **21**, 814–817 (1968) (cited on page 48).

[133] Y Tokura, "Critical features of colossal magnetoresistive manganites", Reports on Progress in Physics **69**, 797–851 (2006) (cited on page 49).

[134] A. Di Bernardo, S. Komori, G. Livanas, G. Divitini, P. Gentile, M. Cuoco, and J. W. A. Robinson, "Nodal superconducting exchange coupling", Nature Materials, 10.1038/s41563-019-0476-3 (2019) (cited on page 48).

[135] J. Linder and J. W. A. Robinson, "Superconducting Spintronics", Nature Physics **11**, 10.1038/nphys3242 (2015) (cited on page 48).

[136] J. Chakhalian, J. W. Freeland, G. Srajer, J. Strempfer, G. Khaliullin, J. C. Cezar, T. Charlton, R. Dalgliesh, C. Bernhard, G. Cristiani, H. U. Habermeier, and B. Keimer, "Magnetism at the interface between ferromagnetic and superconducting oxides", Nature Physics **2**, 244–248 (2006) (cited on page 48).

[137] T. Elovaara, H. Huhtinen, S. Majumdar, and P. Paturi, "Irreversible metamagnetic transition and magnetic memory in small-bandwidth manganite $Pr_{1-x}Ca_xMnO_3$ (x=0.0-0.5)", Journal of Physics Condensed Matter **24**, 216002 (2012) (cited on pages 49, 52).

[138] A. Venimadhav, M. S. Hegde, R. Rawat, and I. Das, "Magnetotransport properties in thin films of charge-ordered materials", Journal of Applied Physics **89**, 8057–8060 (2001) (cited on page 51).

[139] T. Tsuyama, S. Chakraverty, S. Macke, N. Pontius, C. Schüßler-Langeheine, H. Y. Hwang, Y. Tokura, and H. Wadati, "Photoinduced Demagnetization and Insulator-to-Metal Transition in Ferromagnetic Insulating $BaFeO_3$ Thin Films", Physical Review Letters **116**, 256402 (2016) (cited on page 59).

[140] T. Elovaara, J. Tikkanen, S. Granroth, S. Majumdar, R. Félix, H. Huhtinen, and P. Paturi, "Mechanisms of photoinduced magnetization in $Pr_{0.6}Ca_{0.4}MnO_3$ studied above and below charge-ordering transition temperature", Journal of Physics: Condensed Matter **29**, 425802 (2017) (cited on page 59).

[141] A. Dussaux, P. Schoenherr, K. Koumpouras, J. Chico, K. Chang, L. Lorenzelli, N. Kanazawa, Y. Tokura, M. Garst, A. Bergman, C. L. Degen, and D. Meier, "Local dynamics of topological magnetic defects in the itinerant helimagnet FeGe", Nature Communications **7**, 12430 (2016) (cited on page 61).

[142] D. Lee, K. W. Lee, J. V. Cady, P. Ovartchaiyapong, and A. C. Jayich, "Topical review: Spins and mechanics in diamond", Journal of Optics **19**, 033001 (2017) (cited on page 65).

[143] W. L. Barnes, "Fluorescence near interfaces: The role of photonic mode density", Journal of Modern Optics **45**, 661–699 (1998) (cited on page 78).

[144] T. Yamaoka, K. Watanabe, Y. Shirakawabe, K. Chinone, E. Saitoh, M. Tanaka, and H. Miyajima, "Applications of high-resolution MFM system with low-moment probe in a vacuum", IEEE Transactions on Magnetics **41**, 3733–3735 (2005) (cited on page 79).

[145] T. Weis, I. Krug, D. Engel, A. Ehresmann, V. Höink, J. Schmalhorst, and G. Reiss, "Characterization of magnetic force microscopy probe tip remagnetization for measurements in external in-plane magnetic fields", Journal of Applied Physics **104**, 10.1063/1.3040025 (2008) (cited on page 79).

[146] R. P. Ferner, S. McVitie, A. Gallagher, and W. A. Nicholson, "Characterisation of MFM tip fields by electron tomography", IEEE Transactions on Magnetics **33**, 4062–4064 (1997) (cited on page 79).

[147] J. Scott, S. McVitie, and R. P. Ferrier, "Characterisation of FeBSiC coated MFM tips using Lorentz electron tomography and MFM", IEEE Transactions on Magnetics **35**, 3986–3988 (1999) (cited on page 79).

[148] S. Kolkowitz, A. C. Bleszynski Jayich, Q. P. Unterreithmeier, S. D. Bennett, P. Rabl, J. G. Harris, and M. D. Lukin, "Coherent sensing of a mechanical resonator with a single-spin qubit", Science **335**, 1603–1606 (2012) (cited on page 79).

[149] N. Diep Lai, D. Zheng, F. Treussart, and J.-F. Roch, "Optical determination and magnetic manipulation of a single nitrogen-vacancy color center in diamond nanocrystal", Advances in Natural Sciences: Nanoscience and Nanotechnology **1**, 015014 (2010) (cited on page 82).

[150] P. R. Dolan, X. Li, J. Storteboom, and M. Gu, "Complete determination of the orientation of NV centers with radially polarized beams", Optics Express **22**, 4379 (2014) (cited on page 82).

[151] T. Hingant, J. P. Tetienne, L. J. Martínez, K. Garcia, D. Ravelosona, J. F. Roch, and V. Jacques, "Measuring the magnetic moment density in patterned ultrathin ferromagnets with submicrometer resolution", Physical Review Applied **4**, 1–7 (2015) (cited on page 96).

[152] J. Cao, Y. Chen, T. Jin, W. Gan, Y. Wang, Y. Zheng, H. Lv, S. Cardoso, D. Wei, and W. S. Lew, "Spin orbit torques induced magnetization reversal through asymmetric domain wall propagation in Ta/CoFeB/MgO structures", Scientific Reports **8**, 10.1038/s41598-018-19927-5 (2018) (cited on page 100).

[153] N. Nagaosa and Y. Tokura, *Topological properties and dynamics of magnetic skyrmions*, 2013 (cited on page 102).

[154] R. Wiesendanger, *Nanoscale magnetic skyrmions in metallic films and multilayers: A new twist for spintronics*, 2016 (cited on page 102).

[155] A. Soumyanarayanan, M. Raju, A. L. Oyarce, A. K. Tan, M. Y. Im, A. P. Petrovic, P. Ho, K. H. Khoo, M. Tran, C. K. Gan, F. Ernult, and C. Panagopoulos, "Tunable room-temperature magnetic skyrmions in Ir/Fe/Co/Pt multilayers", Nature Materials **16**, 898–904 (2017) (cited on page 102).

[156] C. Moreau-Luchaire, C. Moutafis, N. Reyren, J. Sampaio, C. A. Vaz, N. Van Horne, K. Bouzehouane, K. Garcia, C. Deranlot, P. Warnicke, P. Wohlhüter, J. M. George, M. Weigand, J. Raabe, V. Cros, and A. Fert, "Additive interfacial chiral interaction in multilayers for stabilization of small individual skyrmions at room temperature", Nature Nanotechnology **11**, 444–448 (2016) (cited on page 102).

[157] S. Heinze, K. Von Bergmann, M. Menzel, J. Brede, A. Kubetzka, R. Wiesendanger, G. Bihlmayer, and S. Blügel, "Spontaneous atomic-scale magnetic skyrmion lattice in two dimensions", Nature Physics **7**, 713–718 (2011) (cited on page 102).

[158] H. Yang, A. Thiaville, S. Rohart, A. Fert, and M. Chshiev, "Anatomy of Dzyaloshinskii-Moriya Interaction at Co/Pt Interfaces", Physical Review Letters **115**, 10.1103/PhysRevLett.115.267210 (2015) (cited on page 102).

[159] B. C. Buchler, T. Kalkbrenner, C. Hettich, and V. Sandoghdar, "Measuring the quantum efficiency of the optical emission of single radiating dipoles using a scanning mirror", Physical Review Letters **95**, 10.1103/PhysRevLett.95.063003 (2005) (cited on page 104).

[160] T. Van Der Sar, F. Casola, R. Walsworth, and A. Yacoby, "Nanometre-scale probing of spin waves using single-electron spins", Nature Communications **6**, 1–8 (2015) (cited on page 109).

[161] I. Gross, W. Akhtar, A. Hrabec, J. Sampaio, L. J. Martínez, S. Chouaieb, B. J. Shields, P. Maletinsky, A. Thiaville, S. Rohart, and V. Jacques, "Skyrmion morphology in ultrathin magnetic films", Physical Review Materials **2**, 10.1103/PhysRevMaterials.2.024406 (2018) (cited on page 112).

[162] W. Akhtar, A. Hrabec, S. Chouaieb, A. Haykal, I. Gross, M. Belmeguenai, M. S. Gabor, B. Shields, P. Maletinsky, A. Thiaville, S. Rohart, and V. Jacques, "Current-Induced Nucleation and Dynamics of Skyrmions in a Co-based Heusler Alloy", Physical Review Applied **11**, 10.1103/PhysRevApplied.11.034066 (2019) (cited on page 112).

[163] W. Legrand, D. Maccariello, F. Ajejas, S. Collin, A. Vecchiola, K. Bouzehouane, N. Reyren, V. Cros, and A. Fert, "Room-temperature stabilization of antiferromagnetic skyrmions in synthetic antiferromagnets", Nature Materials, 10.1038/s41563-019-0468-3 (2019) (cited on page 112).

[164] K. S. Novoselov, A. K. Geim, S. V. Morozov, D. Jiang, Y. Zhang, S. V. Dubonos, I. V. Grigorieva, and A. A. Firsov, "Electric field in atomically thin carbon films", Science **306**, 666–669 (2004) (cited on page 112).

[165] B. Huang, G. Clark, E. Navarro-Moratalla, D. R. Klein, R. Cheng, K. L. Seyler, D. Zhong, E. Schmidgall, M. A. McGuire, D. H. Cobden, W. Yao, D. Xiao, P. Jarillo-Herrero, and X. Xu, "Layer-dependent ferromagnetism in a van der Waals crystal down to the monolayer limit", Nature **546**, 270–273 (2017) (cited on page 113).

[166] T. Song, X. Cai, M. W. Y. Tu, X. Zhang, B. Huang, N. P. Wilson, K. L. Seyler, L. Zhu, T. Taniguchi, K. Watanabe, M. A. McGuire, D. H. Cobden, D. Xiao, W. Yao, and X. Xu, "Giant tunneling magnetoresistance in spin-filter van der Waals heterostructures", Science **360**, 1214–1218 (2018) (cited on page 113).

[167] L. Thiel, Z. Wang, M. A. Tschudin, D. Rohner, I. Gutiérrez-Lezama, N. Ubrig, M. Gibertini, E. Giannini, A. F. Morpurgo, and P. Maletinsky, "Probing magnetism in 2D materials at the nanoscale with single-spin microscopy", Science **364**, 973–976 (2019) (cited on page 113).

[168] Y. Cao, V. Fatemi, S. Fang, K. Watanabe, T. Taniguchi, E. Kaxiras, and P. Jarillo-Herrero, "Unconventional superconductivity in magic-angle graphene superlattices", Nature **556**, 43–50 (2018) (cited on page 113).

[169] Q. Tong, F. Liu, J. Xiao, and W. Yao, "Skyrmions in the Moiré of van der Waals 2D Magnets", Nano Letters **18**, 7194–7199 (2018) (cited on page 113).

[170] J. Scheuer, I. Schwartz, Q. Chen, D. Schulze-Sünninghausen, P. Carl, P. Höfer, A. Retzker, H. Sumiya, J. Isoya, B. Luy, M. B. Plenio, B. Naydenov, and F. Jelezko, "Optically induced dynamic nuclear spin polarisation in diamond", New Journal of Physics **18**, 10.1088/1367-2630/18/1/013040 (2016) (cited on page 113).

[171] I. Schwartz, J. Scheuer, B. Tratzmiller, S. Müller, Q. Chen, I. Dhand, Z. Y. Wang, C. Müller, B. Naydenov, F. Jelezko, and M. B. Plenio, "Robust optical polarization of nuclear spin baths using Hamiltonian engineering of nitrogen-

vacancy center quantum dynamics", Science Advances **4**, 10.1126/sciadv.aat8978 (2018) (cited on page 113).